

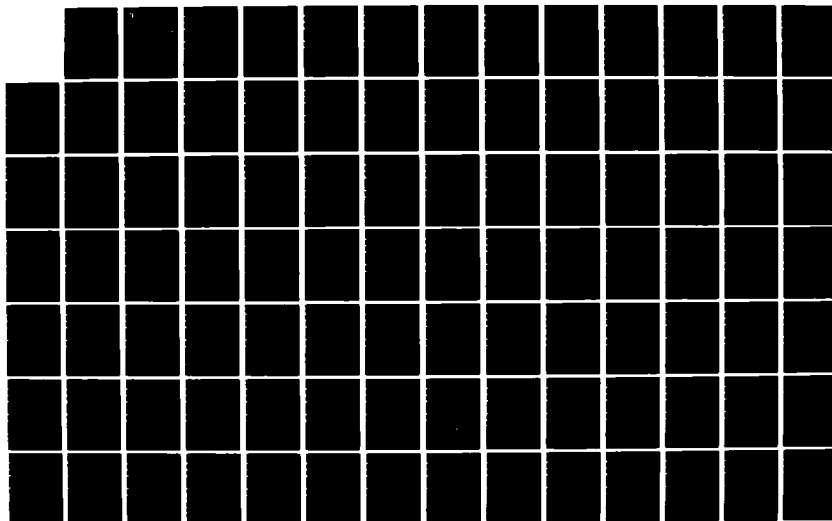
AD-A163 983

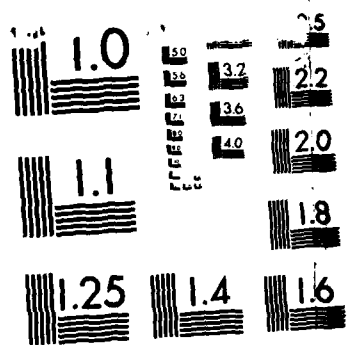
RADIATION AUGMENTED PROPULSION FEASIBILITY(U) ROCKWELL  
INTERNATIONAL CANOGA PARK CA ROCKETDYNE DIV  
S C HURLOCK ET AL DEC 85 RI/RD85-257 AFRPL-TR-85-068  
F04611-84-C-0047 F/G 10/1

14

UNCLASSIFIED

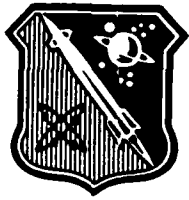
NL





MICROCOPY RESOLUTION TEST CHART  
NATIONAL BUREAU OF STANDARDS-1963-A

(12)

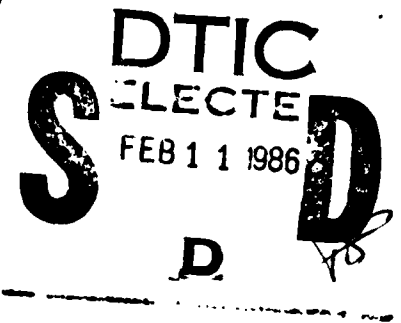


AFRPL TR-85-068

AD:

Final Report  
for the period  
17 Sept 1984 to  
28 Sept 1985

## Radiation Augmented Propulsion Feasibility



December 1985

Authors:  
S. C. Hurlock  
V. Quan  
J. Blauer  
J. R. Hall  
R. I. Wagner  
R. D. Wilson

Rockwell International  
Rocketdyne Division  
6633 Canoga Ave  
Canoga Park, CA 91304

### Approved for Public Release

Distribution is unlimited. The AFRPL Technical Services Office has reviewed this report, and it is releasable to the National Technical Information Service, where it will be available to the general public, including foreign nationals.

AD-A163 983

DTIC FILE COPY

*prepared for the:*

**Air Force  
Rocket Propulsion  
Laboratory**

Air Force Space Technology Center  
Space Division, Air Force Systems Command  
Edwards Air Force Base,  
California 93523-5000


## NOTICE


When U.S. Government drawings, specifications, or other data are used for any purpose other than a definitely related Government procurement operation, the Government thereby incurs no responsibility nor any obligation whatsoever, and the fact that the Government may have formulated, furnished, or in any way supplied the said drawings, specifications, or other data is not to be regarded by implication or otherwise, or in any manner licensing the holder or any other person or corporation, or conveying any rights or permission to manufacture, use or sell any patented invention that may in any way be related hereto.

## FOREWORD

This final technical report for contract number F04611-84-C-0047, was prepared by Rockwell International, Rocketdyne Division. The period of report was 17 Sep 1984 to 28 September 1985.

This technical report has been reviewed and is approved for publication and distribution in accordance with the distribution statement on the cover and on the DD Form 1473.

  
STEPHEN L. RODGERS  
Project Manager

  
JOHN T. NAKAMURA  
Chief, Chemistry and Materials  
Branch

FOR THE DIRECTOR

  
CLARK W. HAWK  
Chief, Liquid Rocket Division

UNCLASSIFIED

SECURITY CLASSIFICATION OF THIS PAGE

## REPORT DOCUMENTATION PAGE

1a. REPORT SECURITY CLASSIFICATION UNCLASSIFIED			1b. RESTRICTIVE MARKINGS	
2a. SECURITY CLASSIFICATION AUTHORITY			3. DISTRIBUTION/AVAILABILITY OF REPORT Approved for Public Release: Distribution is unlimited	
2b. DECLASSIFICATION/DOWNGRADING SCHEDULE				
4. PERFORMING ORGANIZATION REPORT NUMBER(S) RI/RD85-257			5. Monitoring Organization Report Number(s) AFRPL-TR-85-068	
6a. NAME OF PERFORMING ORGANIZATION Rockwell International Rocketdyne Division		6b. OFFICE SYMBOL (If applicable)		7a. NAME OF MONITORING ORGANIZATION Air Force Rocket Propulsion Laboratory
6c. ADDRESS (City, State and ZIP Code) 6633 Canoga Ave. Canoga Park CA 91304			7b. ADDRESS (City, State and ZIP Code) AFRPL/LKLR - Stop 24 Edwards Air Force Base, CA 93523-5000	
8a. NAME OF FUNDING/SPONSORING ORGANIZATION		8b. OFFICE SYMBOL (If applicable)		9. PROCUREMENT INSTRUMENT IDENTIFICATION NUMBER F04611-84-C-0047
8c. ADDRESS (City, State and ZIP Code)			10. SOURCE OF FUNDING NOS.	
			PROGRAM ELEMENT NO. 62302F	PROJECT NO. 5730
			TASK NO. 00	WORK UNIT NO. EW
11. TITLE (Include Security Classification) Radiation Augmented Propulsion Feasibility Study (U)				
12. PERSONAL AUTHOR(S) Hurlock, S. C.; Quan, V.; Blauer, J.; Hall, J. R.; Wagner, R. I.; Wilson, R. D.				
13a. TYPE OF REPORT FINAL		13b. TIME COVERED FROM 84/9/17 TO 85/9/28		14. DATE OF REPORT (Yr., Mo., Day) 85 12
15. PAGE COUNT 112				
16. SUPPLEMENTARY NOTATION				
17. COSATI CODES			18. SUBJECT TERMS (Continue on reverse if necessary and identify by block number)	
FIELD	GROUP	SUB. GR.		
c7	c2		Solar Propulsion, Chlorine, Iodine Monochloride, Hydrogen Chloride, Xenon Flashlamps, Ultraviolet Absorption, Kinetics, Photolysis	
19. ABSTRACT (Continue on reverse if necessary and identify by block number)				
Experiments and analysis were conducted to characterize the absorption of ultraviolet and visible radiation and subsequent energy release in chlorine gas, iodine monochloride vapor, and mixtures of hydrogen gas and chlorine gas. Xenon flashlamps were used to provide the radiation. Measurements included lamp electrical and optical characteristics, light energy absorbed, pressure rise in the closed reactor and reactants remaining after the reaction. Analysis included detailed kinetic modelling of the single shot experiments.				
20. DISTRIBUTION/AVAILABILITY OF ABSTRACT UNCLASSIFIED/UNLIMITED <input checked="" type="checkbox"/> SAME AS RPT <input type="checkbox"/> DTIC USERS <input type="checkbox"/>			21. ABSTRACT SECURITY CLASSIFICATION UNCLASSIFIED	
22a. NAME OF RESPONSIBLE INDIVIDUAL STEPHEN L. RODGERS			22b. TELEPHONE NUMBER (Include Area Code) (805) 277-5416	22c. OFFICE SYMBOL AFRPL/LKLR

## SUMMARY

Gas phase absorption of solar radiation has been suggested as an energy source to power space propulsion systems. The absorbing gas could be an expendable propellant or could be used in a closed cycle, exchanging heat with an expendable propellant. This study was conducted in order to develop basic data and understanding useful for the evaluation of such a system with the absorbing gas being a halogen or an interhalogen.

Three specific chemical systems were selected for study. These are  $\text{Cl}_2$ ,  $\text{ICl}$ , and  $\text{Cl}_2 + \text{H}_2$ . In this latter system, the chemical energy released by the photoinitiated formation of  $\text{HCl}$  from the elements is augmented by the radiation energy absorbed by  $\text{Cl}_2$ .

Experiments were conducted in which photolysis reactors were filled with the gases over a range of pressures and flashlamps were fired, thereby exposing the gases to a short pulse ( $5 \mu\text{s} - 10 \mu\text{s}$ ) of intense radiation intended to spectrally simulate the exoatmospheric solar radiation. Optical monitors provided time dependent data on the lamp output and on the in-band absorption. A fast pressure transducer provided time dependent data on the pressure rise within the closed reactors, thereby yielding information on the temperature rise and energy absorption.

Two reactor and flashlamp configurations were used. The first was a cylindrical reactor with a 100 J linear flashlamp mounted on its axis. This setup provided data useful in demonstrating energy deposition and release and in validating a radiation-kinetics-thermodynamics model. Observed pressure rise was limited because of the need to include  $\text{SF}_6$  gas in the reactor to alleviate an arcing problem and because of the relatively low ultraviolet output from the lamp. The second configuration employed a 9 kJ linear flashlamp and a small reactor adjacent to it which received a portion of the lamp radiation. This lamp was richer in ultraviolet output and the reactor did not need diluent or insulating gas, thus leading to higher observed pressure rises.

Pressure rise data in  $\text{Cl}_2$  and  $\text{ICl}$  corresponded to temperature increases of over 500K. When  $\text{Cl}_2 + \text{H}_2$  were exposed to the flashlamp radiation,

temperature rises of up to 2600K were observed. In the  $\text{Cl}_2 + \text{H}_2$  system, radiation augmentation was estimated to be up to 10-15 of the chemical energy.

An extensive kinetic rate package was assembled for the reactions studied and this data, together with spectroscopic data on the flashlamp and on the absorbing gases was used as input to a Rocketdyne numerical analysis model. Correlation of data obtained with  $\text{Cl}_2 + \text{SF}_6$  in the internal flashlamp configuration was quite good. Reasonable correlation of data obtained with  $\text{Cl}_2 + \text{H}_2 + \text{SF}_6$  was achieved after significant modifications of the rate set to include chain termination by  $\text{SF}_6$  and  $\text{O}_2$ . With the  $\text{SF}_6$  and some  $\text{O}_2$  impurity, the formation of HCl from the elements only proceeded part way to completion, about 50% at most, and this termination was successfully modelled numerically.

Analysis of the data obtained with the external flashlamp arrangement was quite satisfactory using basic spectroscopic and thermochemical principles.

Thus, data were collected and analytical methods were developed which have applicability to the evaluation of solar powered space propulsion systems deriving all or part of their energy through gas phase absorption of solar radiation.

## FOREWORD

The work reported here was conducted for the Air Force Rocket Propulsion Laboratory (AFRPL) by the Rocketdyne Division of Rockwell International. Rocketdyne received the contract for the work as a result of a proposal submitted in response to an AFRPL Program Research and Development announcement (PRDA AFRPL84-02: Configuration Energy Source). Rocketdyne's project team included the following individuals:

Dr. Stephen Hurlock -	Principal Investigator
Dr. Victor Quan -	Analysis and Modeling
Dr. Jay Blauer -	Chemical Kinetics
Mr. James Hall -	Pulsed Power and High Voltage Engineering
Dr. Ross Wagner -	Chemistry
Mr. Richard Wilson -	Chemistry

In addition, Messrs. Les Rogers and Tom Marks ably assembled and installed the experimental apparatus and assisted in the testing.

The program benefitted from consultation by Dr. Robert Hanrahan of Solar Reactor Space and Defense Technologies, Inc. (SRT) of Miami, Florida. SRT also provided their 100 Joule flashlamp photolysis equipment of use in the test program.

The encouragement and support provided by Dr. Stephen Rodgers, the AFRPL Program Manager, was especially helpful in the conduct and completion of the program.



Accession For	
NTIS	CRA&I <input checked="" type="checkbox"/>
DTIC	TAB <input type="checkbox"/>
Unannounced	<input type="checkbox"/>
Justification	
By	
Distribution	
Availability Codes	
Dist	Avail and/or Special
A-1	



## TABLE OF CONTENTS

REPORT DOCUMENTATION PAGE . . . . .	i
SUMMARY . . . . .	iii
FOREWORD . . . . .	v
TABLE OF CONTENTS . . . . .	vi
LIST OF FIGURES . . . . .	viii
LIST OF TABLES . . . . .	x
INTRODUCTION . . . . .	1
BACKGROUND . . . . .	3
Solar Radiation . . . . .	3
Halogens as Solar Radiation Absorbers . . . . .	3
Recovery of Deposited Energy . . . . .	8
OBJECTIVES AND SCOPE . . . . .	10
APPROACH . . . . .	12
EXPERIMENTAL DESCRIPTION . . . . .	14
GAS HANDLING SYSTEM . . . . .	14
PHOTOLYSIS CELL . . . . .	22
Internal Lamp Configuration . . . . .	22
External Lamp Configuration . . . . .	24
CELL AND LAMP DIAGNOSTICS AND DATA SYSTEM . . . . .	24
Voltage and Current Measurements . . . . .	24
Optical Measurements . . . . .	26
Pressure Measurements . . . . .	26
Data Acquisition System . . . . .	34
FLASHLAMP DRIVER AND FLASHLAMP . . . . .	34
Small Flashlamp System . . . . .	34
Large Flashlamp System . . . . .	35
OBSERVATIONAL RESULTS . . . . .	38
FLASHLAMP CHARACTERIZATION . . . . .	38
Electrical Energy Deposition in the Small Flashlamp System . . . . .	38
Optical Characteristics of the Small Flashlamp System . . . . .	44
Electrical Energy Deposition in the Large Flashlamp System . . . . .	48
Optical Characteristics of the Large Flashlamp System . . . . .	48

# TABLE OF CONTENTS

(continued)

FLASHLAMP ENERGY ABSORPTION BY $\text{Cl}_2$ . . . . .	55
Ultraviolet Absorption, Small Flashlamp System . . . . .	55
Ultraviolet Absorption, Large Flashlamp System . . . . .	58
Pressure Rise in Small Flashlamp System . . . . .	58
Pressure Rise in Large Flashlamp System . . . . .	61
FLASHLAMP ENERGY ABSORPTION BY $\text{ICl}$ . . . . .	74
ANALYSIS AND INTERPRETATION . . . . .	77
NUMERICAL ANALYSIS . . . . .	77
Computer Program Description . . . . .	77
Kinetic Data Set . . . . .	79
Spectroscopic and Radiometric Data Set . . . . .	79
Sample Calculations . . . . .	83
Correlation of Results . . . . .	83
ANALYSIS OF RESULTS FOR LARGE FLASHLAMP SYSTEM . . . . .	88
Energy Deposition and Release in $\text{Cl}_2$ . . . . .	91
Energy Deposition and Release in $\text{Cl}_2 + \text{H}_2$ . . . . .	93
CONCLUSIONS . . . . .	96
RECOMMENDATIONS . . . . .	98
LIST OF REFERENCES . . . . .	99

## LIST OF FIGURES

1.	Solar propulsion concept . . . . .	2
2.	Solar spectral irradiance at the mean distance of the earth from the sun. . . . .	4
3.	Extinction coefficients for halogens at 298 K . . . . .	5
4.	Interhalogen continuum absorption bands . . . . .	6
5.	Energy release in $\text{Cl}_2$ and $\text{Cl}_2 + \text{H}_2$ . . . . .	11
6.	Comparison of solar spectrum and xenon flashlamp spectrum . . .	13
7.	Functional block diagram of experimental setup . . . . .	15
8.	Building 315 Layout . . . . .	16
9.	Gas handling system schematic . . . . .	17
10.	Photolysis reactor with internal flashlamp. . . . .	23
11.	Photolysis cell for use with external flashlamp . . . . .	25
12.	Optical channels as configured on photolysis reactor with internal flashlamp . . . . .	27
13.	Photodiode detector circuit . . . . .	28
14.	Transmission of 334 nm bandpass filter . . . . .	29
15.	Transmission of 550 nm long wave pass filter . . . . .	30
16.	Transmission of 500 nm bandpass filter . . . . .	31
17.	Transmission of 650 nm band pass filter . . . . .	32
18.	Detector spectral response . . . . .	33
19.	Overall arrangement for 100 J flashlamp experiments . . . . .	36
20.	Overall arrangement for 9KJ flashlamp experiments . . . . .	37
21.	Electrical characteristics of 10kV lamp discharge . . . . .	39
22.	Lamp voltage waveforms for 5, 7, and 10 kV discharges . . . . .	41
23.	Lamp current waveforms for 5,7,and 10 kV discharges . . . . .	42
24.	Lamp electrical characteristics . . . . .	43
25.	Reproducibility of waveforms for different gas fills with $\text{SF}_6$ .	45
26.	Electrical and optical characteristics of 10kV discharge with no absorber . . . . .	46
27.	Electrical and optical integrals for 10kV discharge with no absorber . . . . .	47
28.	Reproducibility of optical flux signals with no absorber . . . .	49
29.	Lamp optical characteristics . . . . .	50

LIST OF FIGURES  
(CONTINUED)

30. Optical and electrical characteristics of the large flashlamp . .	51
31. Summary of flashlamp intensity beyond 550nm . . . . .	53
32. Summary of flashlamp intensity near 334nm compared with intensity beyond 550nm . . . . .	54
33. $\Phi_{330}(t)$ for various $\text{Cl}_2$ partial pressures . . . . .	56
34. Absorption by $\text{Cl}_2$ at 334nm . . . . .	57
35. Transmitted intensity vs. $\text{Cl}_2$ pressure for the large flashlamp and 10 cm reactor . . . . .	59
36. Pressure trace with a 10kV discharge in $\text{H}_2 + \text{Cl}_2$ . . . . .	60
37. Pressure behavior with a 10kV discharge in $\text{H}_2 + \text{Cl}_2$ . . . . .	62
38. Pressure rise in $\text{Cl}_2$ corrected for shifting baseline . . . . .	65
39. Fourier transform of pressure trace shown earlier in Fig. 38 . . .	66
40. Expanded display of the pressure trace shown in Fig. 38 . . . . .	68
41. Observed pressure and temperature rise in $\text{Cl}_2$ . . . . .	69
42. Pressure trace with $\text{H}_2$ and $\text{Cl}_2$ in the reactor . . . . .	70
43. Observed pressure rise in $\text{Cl}_2 + \text{H}_2$ based on highest peak . . . . .	71
44. Observed pressure rise in $\text{Cl}_2 + \text{H}_2$ based on average of first two peaks . . . . .	72
45. Observed temperature rise in $\text{Cl}_2 + \text{H}_2$ based on time between first two peaks . . . . .	73
46. Observed $\text{ICl}$ absorption near 500 nm . . . . .	75
47. Observed pressure rise in $\text{ICl}$ . . . . .	76
48. Sample computed results, pressure vs. time . . . . .	84
49. Sample computed results, $\text{Cl}_2$ concentration vs. time . . . . .	85
50. Pressure rise in $\text{Cl}_2 + \text{SF}_6$ . . . . .	86
51. Sensitivity of computational results to model parameters . . . . .	89
52. $\text{SF}_6 + \text{H}_2 + \text{Cl}_2$ results . . . . .	90
53. Analysis for temperature rise in $\text{Cl}_2$ . . . . .	92
54. Analytical and experimental temperature rise in $\text{Cl}_2 + \text{H}_2$ . . . . .	94

## LIST OF TABLES

1. Summary of Halogen Absorption Data	
Relevant to Solar Absorption . . . . .	7
2. Basic Parameters Summary for Halogen Absorbers . . . . .	9
3. Gas Handling System Component List . . . . .	18
4. Flashlamp Spectral Comparison . . . . .	52
5. Pressure Rise with $\text{SF}_6 + \text{Cl}_2$ . . . . .	63
6. Pressure Rise and $\text{Cl}_2$ Reacted with $\text{SF}_6 + \text{Cl}_2 + \text{H}_2$ . . . . .	64
7. Acoustic Frequencies (calculated . . . . .	75
8. Model Operation . . . . .	78
9. Recombination Reactions . . . . .	80
10. Einstein Coefficients for Spontaneous Emission . . . . .	81
11. Molecular Reactions . . . . .	82

## INTRODUCTION

Space propulsion systems currently in use or planned typically operate by expelling high velocity exhaust to provide thrust. The kinetic energy of the exhaust derives from potential energy which is stored in the payload as pressurization or as chemical energy in energetic propellants. It is appealing to consider advanced space propulsion systems in which all or part of the kinetic energy of the exhaust is provided through the absorption of solar radiation by the propellants.

Advanced space propulsion systems based on these concepts must be evaluated in terms of their performance relative to conventional systems. Evaluations of this type have identified long-duration, low-thrust missions such as station keeping and attitude control as potentially attractive applications for advanced propulsion systems deriving energy from radiation absorption. One approach to converting radiation to kinetic energy, which is the approach addressed by this study, is to use propellants which undergo a chemical change upon irradiation. The radiant energy is thus deposited into the propellant as the heat of formation of the new species. This energy is subsequently recovered and converted to thrust. In some systems the absorbed radiation may be the total energy available while in other systems it may augment chemically stored energy.

Figure 1 shows a very simplified schematic diagram for a propulsion system based on these ideas. The system shown includes a fluid flow loop with components for absorbing solar radiation, for transferring the energy to an expendable propellant, for reconditioning the working fluid, and for pumping it around the loop. The sketch implies a closed loop for the fluid which interacts with the solar radiation and a separate flow system for the expendable propellant, although variations on this scheme could also be considered. Furthermore, the source of energy for the working fluid conditioner and pump is not identified but a number of concepts could be considered, including tapping some of the energy out of the energy transfer device. It should be emphasized that the system shown here differs generically from the solar dynamic cycles, such as are being considered for Space Station power (Ref. 1) or from solar heated thruster concepts (Ref. 2) in that all or part of the energy added to the working fluid is directly absorbed via an overlap between

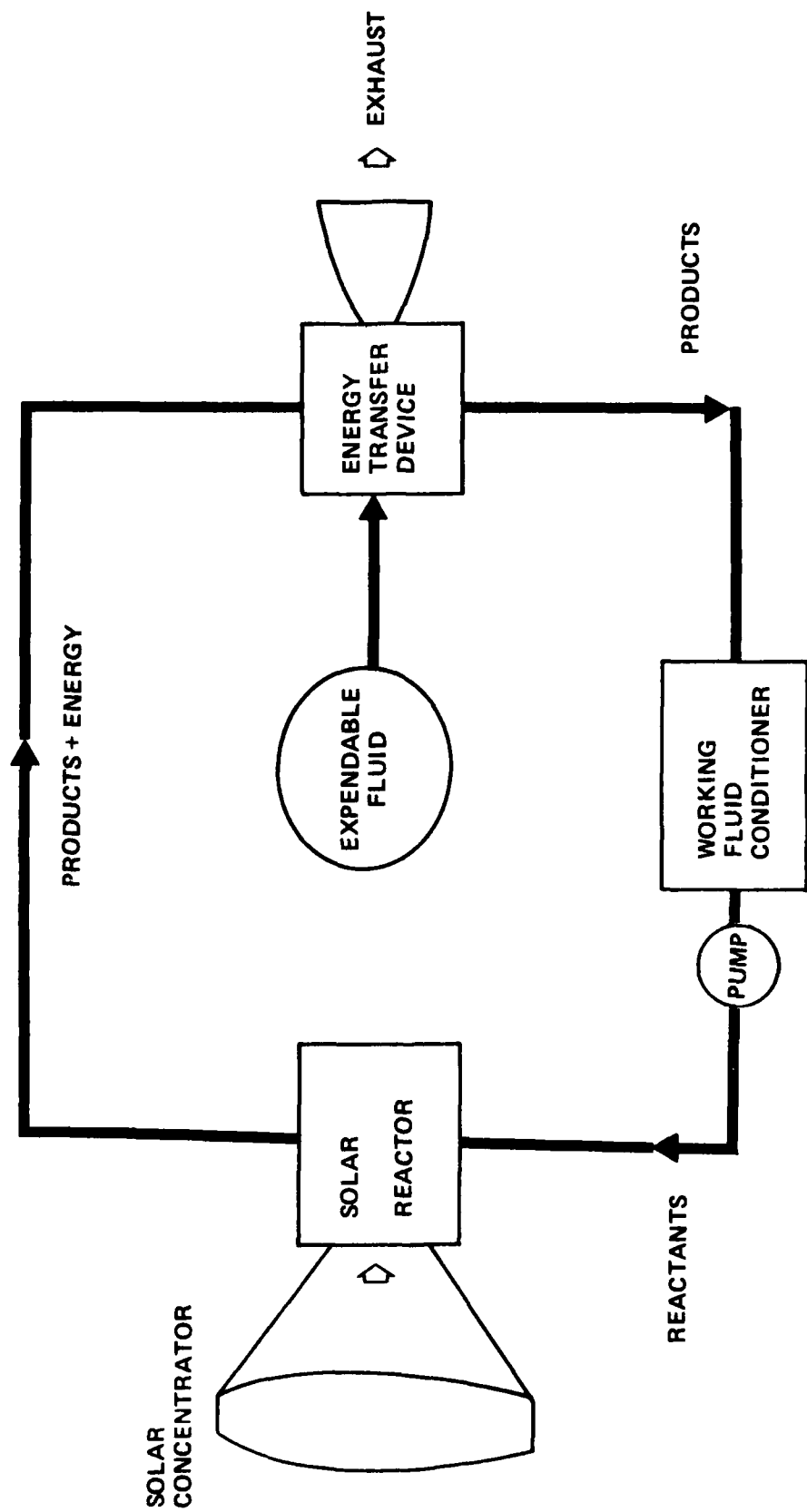


Figure 1. Solar propulsion concept.

the solar spectrum and the absorption spectrum of one or more components of the working fluid. The work reported here was conducted in order to assist in the evaluation of solar powered propulsion systems of the general type shown.

## BACKGROUND

### Solar Radiation

The spectrum of the solar radiation outside the earth's atmosphere closely resembles a 5900K blackbody spectrum (Ref.3 pp 3-34 to 3-29). The actual solar spectral irradiance outside the atmosphere is well represented by a standard curve proposed the Thekacara (Ref.4) and shown in Fig. 2. The coordinates for this curve are tabulated in Ref. 3 and 4 at 0.005 and 0.010  $\mu\text{m}$  intervals and these have been used for all solar spectrum calculations discussed here. The spectral irradiance integrated over wavelength yields the total exoatmospheric solar irradiance of  $1353 \text{ W/m}^2$ .

### Halogens as Solar Radiation Absorbers

When gas phase or volatile compounds are surveyed for photochemical activity induced by solar radiation, the halogens and their compounds show up clearly as candidates. The diatomic halogens  $\text{Cl}_2$ ,  $\text{Br}_2$ , and  $\text{I}_2$  have relatively broad absorptions peaking at about 330, 410, and 490 nm, respectively (Ref. 5). These are shown in Figure 3. The quantum yield for production of atoms from these molecules is essentially one from 250 to 500 nm, falling to about 0.5 for  $\text{I}_2$  from 500 to 600 nm (Ref. 6 pp 184-192). This leads to the potential for these molecules, taken in combination, to convert approximately 30% of the solar radiant energy into the heat of formation of ground state or excited atoms. When diatomic interhalogens (Figure 4) are considered, the absorption range is extended to beyond 600 nm (Ref. 7) and the solar absorption efficiency to above 35%. There are other more complex halogen-containing molecules, perfluoroalkyl iodides for example, whose photochemistry is well known from flash pumped laser research (Ref. 8). Molecules in this category were not considered as candidate absorbers because of potential difficulties associated with byproduct formation.

Table 1 lists some information on the halogens and interhalogens relevant to



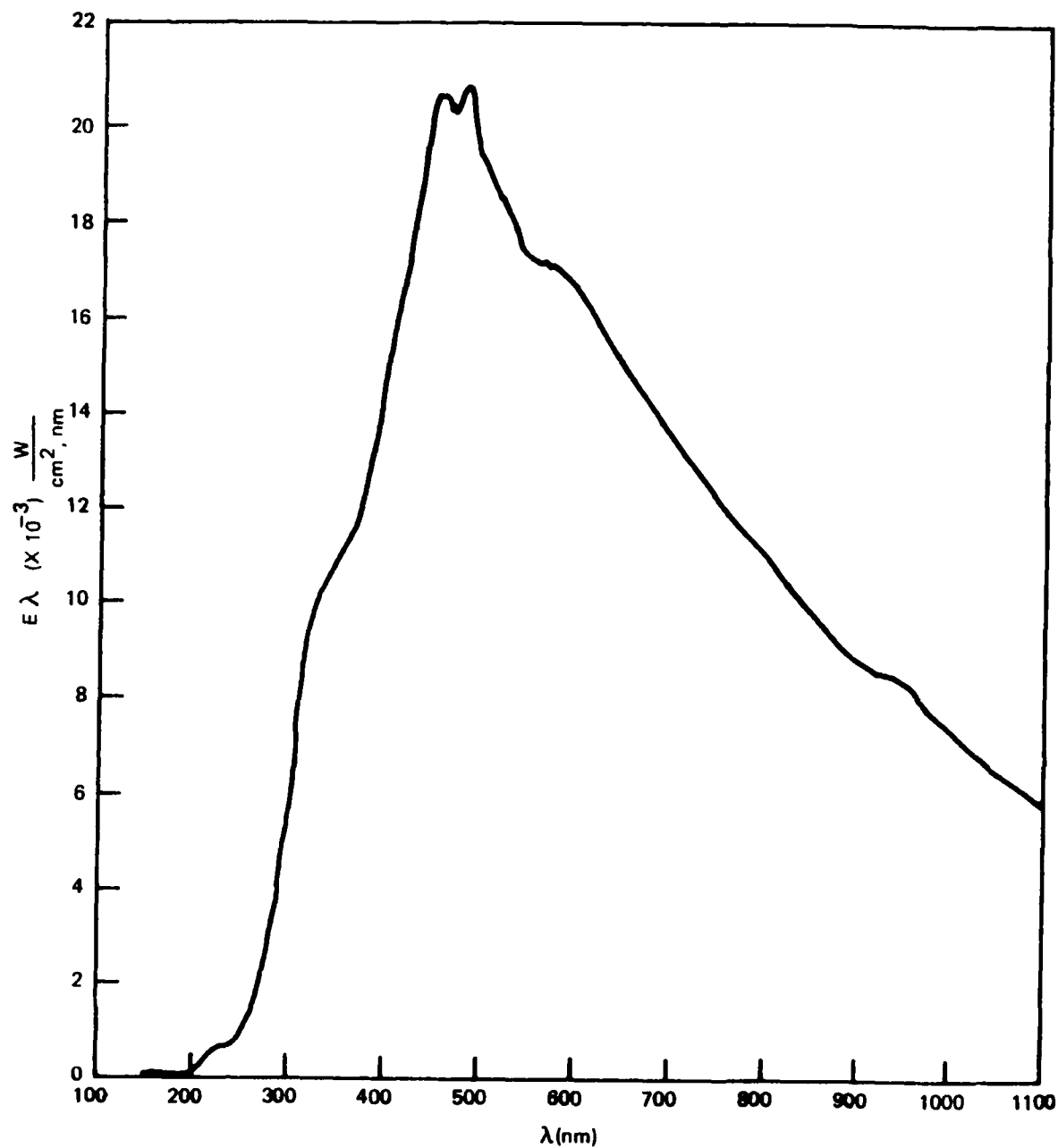


Figure 2. Solar spectral irradiance at the mean distance  
(149.68  $\times 10^6$  km) of the earth from the sun  
[total exatmospheric irradiance = 1.353 kW/m $^2$   
(Ref. 3)].

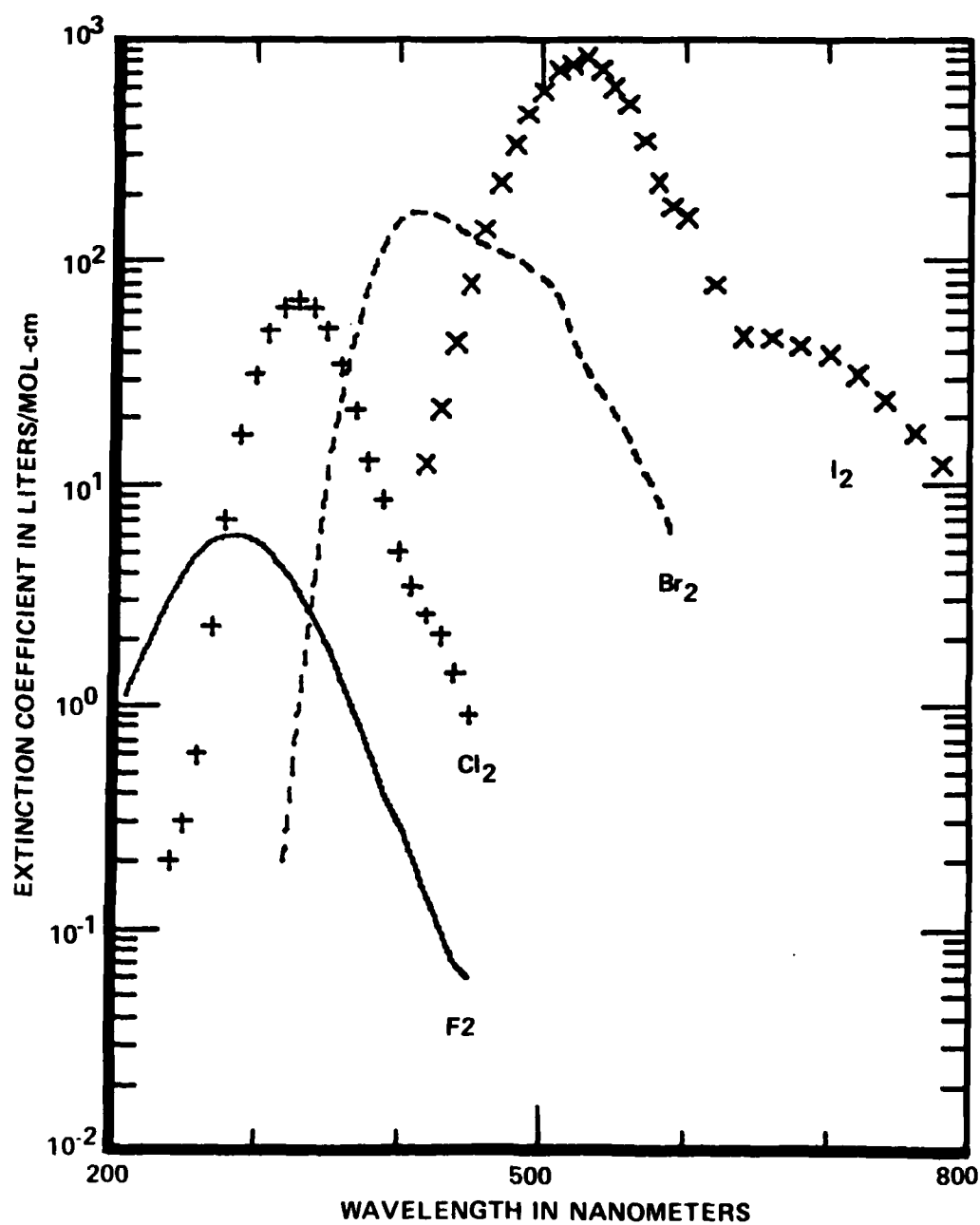


Figure 3. Extinction coefficient for halogens at 298°K (Ref. 5).

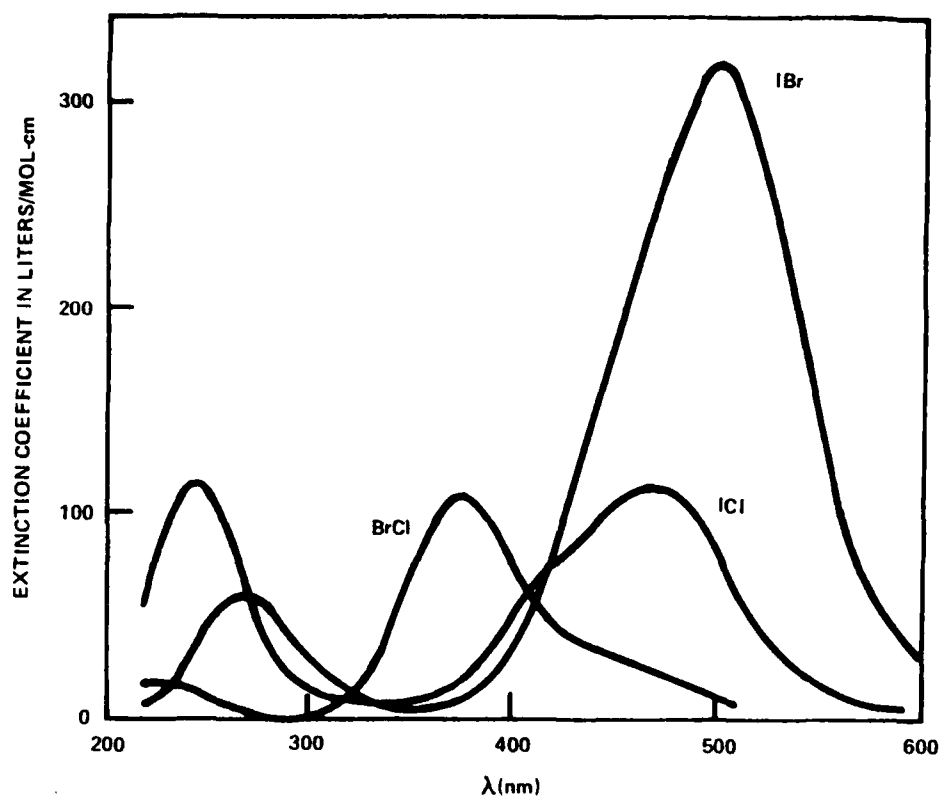


Figure 4. Interhalogen continuum  
absorption bands (Ref. 7).

TABLE 1. SUMMARY OF HALOGEN ABSORPTION DATA  
RELEVANT TO SOLAR ABSORPTION

REACTION	$\lambda_{\text{MAX}}$ (NM)	$\Delta E \lambda_{\text{MAX}}$ (KCAL/MOL)	$\lambda_{\text{RANGE}}$ (NM)	POTENTIAL SOLAR ABSORPTION EFFICIENCY (% OF 1353 W/M <sup>2</sup> )
$\text{Cl}_2 \rightarrow 2\text{Cl}(^2p_{3/2})$	330	86.640	250-450	14
$\text{Br}_2 \rightarrow \text{Br}(^2p_{3/2}) + \text{Br}(^2p_{3/2}, 1/2)$	466.2	61.328	300-510 (600)*	26
$\text{I}_2 \rightarrow \text{I}(^2p_{1/2}) + \text{I}(^2p_{3/2})$	499.5	57.239	400-500 (650)*	21
$\text{IBr} \rightarrow \text{I}(^2p_{3/2}) + \text{Br}(^2p_{1/2}, 3/2)$	500	57.182	220-600	32
$\text{ICI} \rightarrow \text{I}(^2p_{3/2}) + \text{Cl}(^2p_{3/2}, 1/2)$	470	60.832	220-570	29
$\text{BrCl} \rightarrow \text{Br}(^2p_{3/2}) + \text{Cl}(^2p_{3/2}, 1/2)$	370	77.273	220-510	22
* $\text{Br}_2$ AND $\text{I}_2$ PHOTODISSOCIATION FOR 510 TO 600 NM AND FOR 500 TO 650 NM, RESPECTIVELY, PROCEEDS AT A QUANTUM YIELD OF ABOUT 0.5				

their consideration as potential solar absorbers. This includes the photodissociation reaction, the wavelength range absorbed, the wavelength of the peak absorption, and the percentage overlap of the absorption spectrum with the solar radiation spectrum. In addition, the energy absorbed per mole of reaction at the peak absorption wavelength is given. This quantity is a measure of the energy absorbing capacity of the halogen, on a molar basis. Further data, relevant to solar energy deposition consideration, is given in Table 2.

#### Recovery of Deposited Energy

There are a number of ways of recovering the energy deposited in halogens by the photolysis. Two recovery paths were explicitly considered in this study. Irradiation produces halogen atoms according to the reactions of Table 1 and also excited molecules when the photolysis yield is less than 1. The atoms are typically hot. For example, the peak of the  $\text{Cl}_2$  absorption at 330 nm provides 86.64 kcal per g mol of  $\text{Cl}_2$  dissociated: this is 28.79 kcal more than the bond energy. The first recovery path considered involves systems containing only halogens. After thermalization of the hot atoms, recombination is induced through three-body or wall-catalyzed recombination reactions. In the case of pure halogens, the parent molecules will be formed. In the case of interhalogens, products will be pure halogens and diatomic interhalogens. Formation of more complex interhalogens has been assumed negligible in this study. The diatomic products will then thermalize. Thus the total photodeposited energy will be recovered as a temperature and pressures rise in the gas. Radiation losses in this type of system have been assumed negligible, but can be treated using a thermal radiation feature of the numerical model.

The second recovery path involves the addition of a fuel, with hydrogen added to chlorine being the example considered here. The final temperature and pressure of the product gas in this case is a result of thermalization of photo-deposited energy plus the chemical energy provided by the formation of HCl from the elements.

The well-known exothermic reaction between elemental hydrogen and chlorine yields 44.15 kcal/g mol of  $\text{Cl}_2$  upon weak photoinitiation. This energy is augmented by up to 86.64 cal/g mol of  $\text{Cl}_2$ , for complete photodissociation to

TABLE 2. BASIC PARAMETER SUMMARY FOR HALOGEN ABSORBERS

	MAX. ENERGY ABSORBED PER M <sup>2</sup> OF COLLECTOR	MAXIMUM ENERGY CAPACITY PER MOLE OF ABSORBER	MAX. EXTINCTION COEFFICIENT $\epsilon$ MOL <sup>-1</sup> CM <sup>-1</sup>	99% ABSORPTION LENGTH AT 1 ATM
Cl <sub>2</sub>	190 J/S	$3.62 \times 10^5$ J	67	0.66 cm
Br <sub>2</sub>	350 J/S	$2.56 \times 10^5$ J	165	0.27 cm
I <sub>2</sub>	285 J/S	$2.39 \times 10^5$ J	810	0.055 cm
IBr	430 J/S	$2.39 \times 10^5$ J	318	0.14 cm
ICl	390 J/S	$2.54 \times 10^5$ J	115	0.39 cm
BrCl	300 J/S	$3.23 \times 10^5$ J	107	0.42 cm

hot ground-state atoms. Thus, this approach yields up to 130.78 kcal/g mol of  $\text{Cl}_2$  dissociated in comparison with the 86.64 kcal/g mol of  $\text{Cl}_2$  which would be available with no hydrogen present or the 44.15 kcal/g mol which is available with weak photoinitiation. This leads to higher temperature product gases at the cost of added complexity and lower loop efficiency for subsequent dissociation of the  $\text{HCl}$  back to  $\text{H}_2$  and  $\text{Cl}_2$ . The situation is shown graphically in Figure 5. The volumetric energy release is plotted vs the wavenumber (and wavelength) for the three situations just discussed. At room temperature, the bond energy for  $\text{Cl}_2$  corresponds to  $20000\text{ cm}^{-1}$  (500nm). Below this energy, the photoinitiated  $\text{H}_2 + \text{Cl}_2$  reaction does not occur. When the chain reaction is weakly initiated, a negligible amount of radiation energy is deposited and the resulting energy release is independent of the wavenumber, as shown in the lower curve. The energy deposited in  $\text{Cl}_2$  depends on the wavenumber as shown by the middle curve, which is for completely dissociated  $\text{Cl}_2$ . When completely dissociated  $\text{Cl}_2$  is reacted with  $\text{H}_2$ , the resulting energy release is as shown by the top curve, which is the sum of the other two. The curve for energy release from an interhalogen would be similar to the  $\text{Cl}_2$  curve shown.

#### OBJECTIVES AND SCOPE

The objective of the work reported here was to develop data and analysis for use in evaluating the feasibility of space propulsion systems, such as the one shown earlier in Figure 1, in which solar energy is absorbed via photochemical reactions and ultimately converted to kinetic energy of the exhaust. In particular, data and analysis were desired so that the solar energy deposition and subsequent thermalization could be characterized. Development and evaluation of detailed schemes for implementing the generic concept shown in Figure 1 were not included.

The class of absorbers included in the present study included only halogens. Three categories of working fluids were considered: (1) pure halogens, (2) mixed halogens and (3) halogens plus fuels. Of course, in an actual system, inert diluents might be added to any of these. Three particular halogen-containing systems were identified for study: (1) chlorine gas, (2) iodine monochloride vapor, and (3) chlorine gas plus hydrogen gas. In the first two systems, the energy released originates only from the solar energy

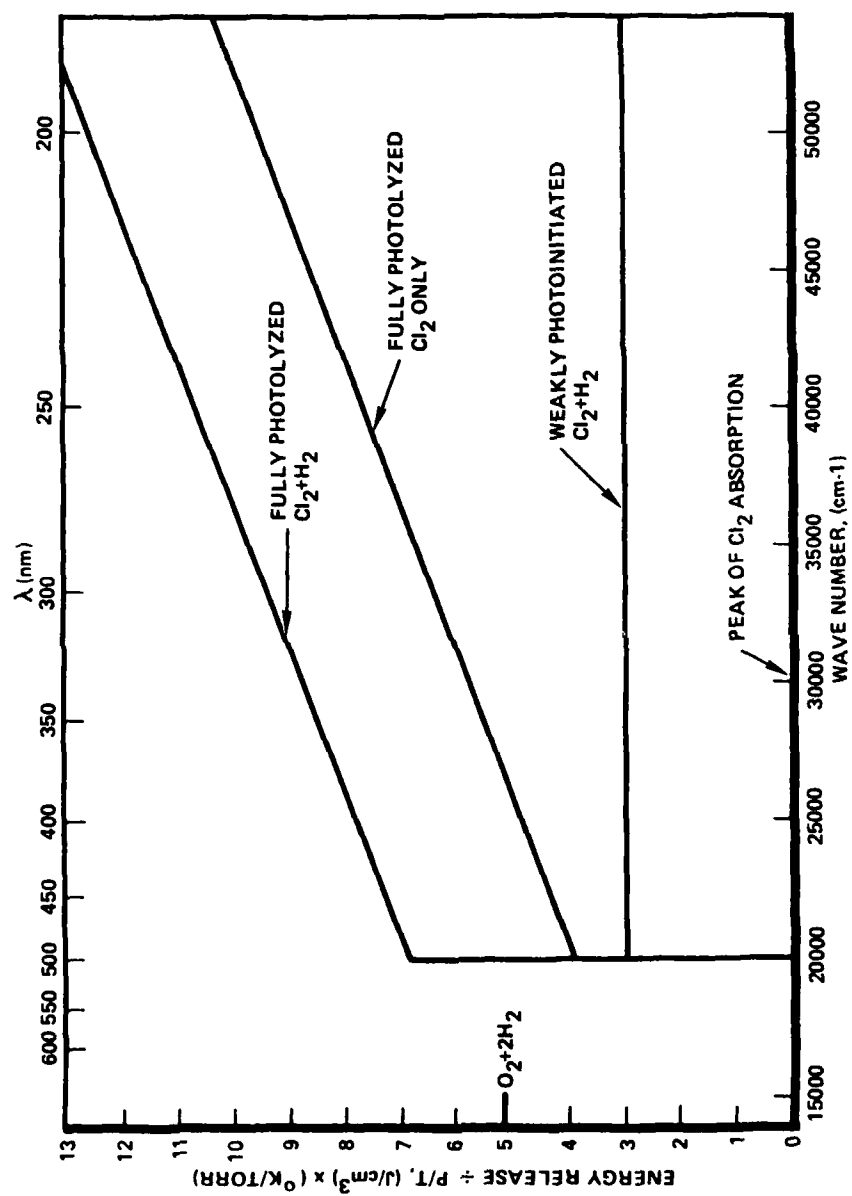


Figure 5. Energy release in  $\text{Cl}_2$  and  $\text{Cl}_2 + \text{H}_2$ .



absorbed. In the third system, the energy released originates from the solar energy absorbed plus the energy associated with the heat of formation of HCl. This latter chemical system had been discussed previously in the context of its utility for solar conversion (Refs. 9-13), but we were unable to find previous reference to the first two chemical systems.

#### APPROACH

The technical approach which was developed for meeting the objectives included experiments and analysis. Single shot flash photolysis experiments were selected because of their relative simplicity and the ability to address the full volume of a reactor which is large enough to make wall effects relatively unimportant. Also important was the consideration that xenon flashlamps, which were selected, provide a good simulation of the solar spectrum, especially when the lamps are operated at high power. Figure 6 shows that the comparison for a lamp fired at 5kJ, 0.75msec is quite good.

A variety of methods was used in the interpretation and analysis of experimental results. However, the most detailed understanding of the chemistry and physics of the energy deposition and subsequent reactions was provided by a Rocketdyne model designated as Radiation Kinetics Mixing Model (RKM). The model was used in the time domain to simulate the flash photolysis experiment. The quality of the correlation between the data and computations was quite good in most cases and validated the detailed understanding of the basic phenomena. The model can be operated in the space domain to predict results from a flowing solar reactor but this was not done in this study.

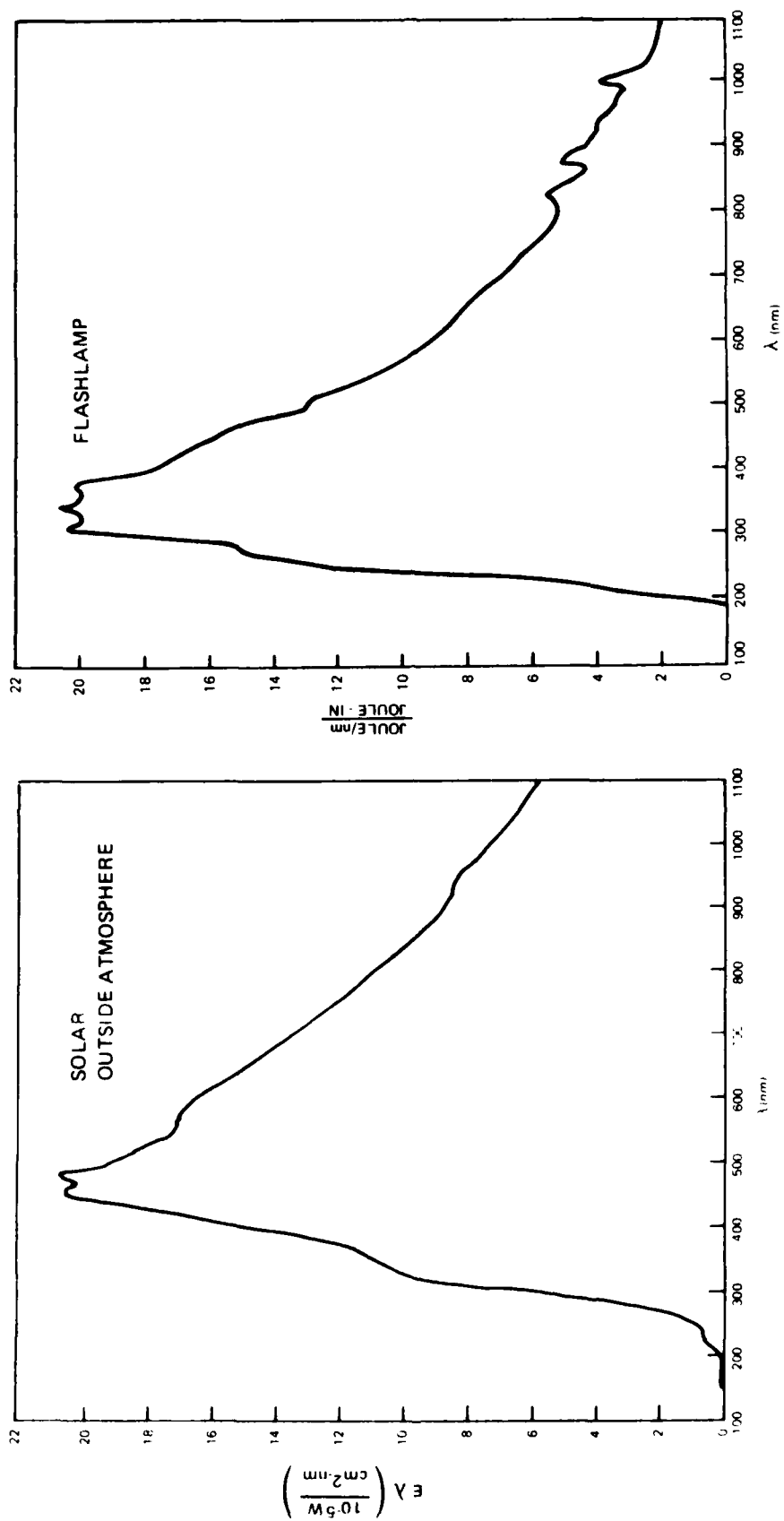


Figure 6. Comparison of solar spectrum and xenon flashlamp spectrum.

## EXPERIMENTAL DESCRIPTION

The experiments which were conducted involved filling a cylindrical cell with various mixtures of He, SF<sub>6</sub>, ICl, Cl<sub>2</sub> and H<sub>2</sub> and then exposing the contents to the light pulse from a xenon flashlamp. The principal independent variables were geometry, composition of the gas fill, and flashlamp intensity. The principal dependent variables (observables) were all recorded as functions of time. They were lamp discharge voltage, lamp discharge current, transmitted photon flux in two wavelength bands, and pressure rise in the cell. The experimental arrangement is shown schematically in Figure 7.

The experiments were conducted at the Rocketdyne Santa Susana Field Laboratories (SSFL) in the Chemical Physics Laboratory (Building 315). Three outdoor test cells and a control station inside the blockhouse were used, as shown in Figure 8. Cell 3 contained all of the gas cylinders. The rest of the gas handling system, the flashlamp, and the photolysis cell were in cell 2. The cold traps and vacuum pump were in cell 1. All of the remote control equipment and the data acquisition were in the blockhouse.

The apparatus which was used to accomplish each of the functions illustrated in Figure 7 typically evolved during the program in response to perceived deficiencies or ideas for improvement. In the following paragraphs, the apparatus is described according to the functions shown in the boxes of Figure 7. Only configurations which produced useful data, presented later, are described.

### GAS HANDLING SYSTEM

The gas handling system was a vacuum line with monel, stainless steel, glass, and Teflon components. The system is shown in detail in the flow schematic of Figure 9. Components are identified in Table 3. Operation of the system was quite straightforward. After evacuation of the system, the run tanks (I1 and I2 in Figure 9) were filled to the appropriate pressures of Cl<sub>2</sub>, 10% Cl<sub>2</sub> in He, H<sub>2</sub>, 10% H<sub>2</sub> in He, He, or SF<sub>6</sub>. H<sub>2</sub> and Cl<sub>2</sub> were never mixed in this operation. This filling was accomplished with one operator at the cylinders in cell 3 (Ref. Figures 8, 9) and one operator at the Switch Panel in the blockhouse (Ref. Figure 8). The operators were in headset communi-

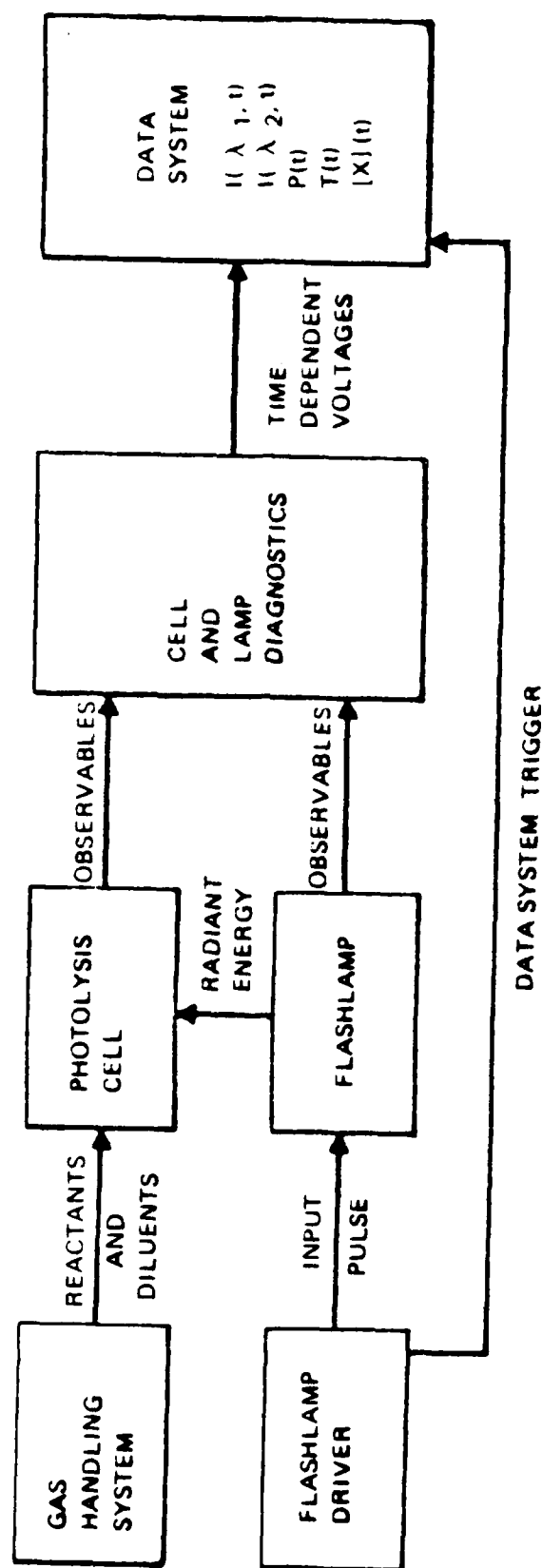


Figure 7. Functional block diagram of experimental setup.

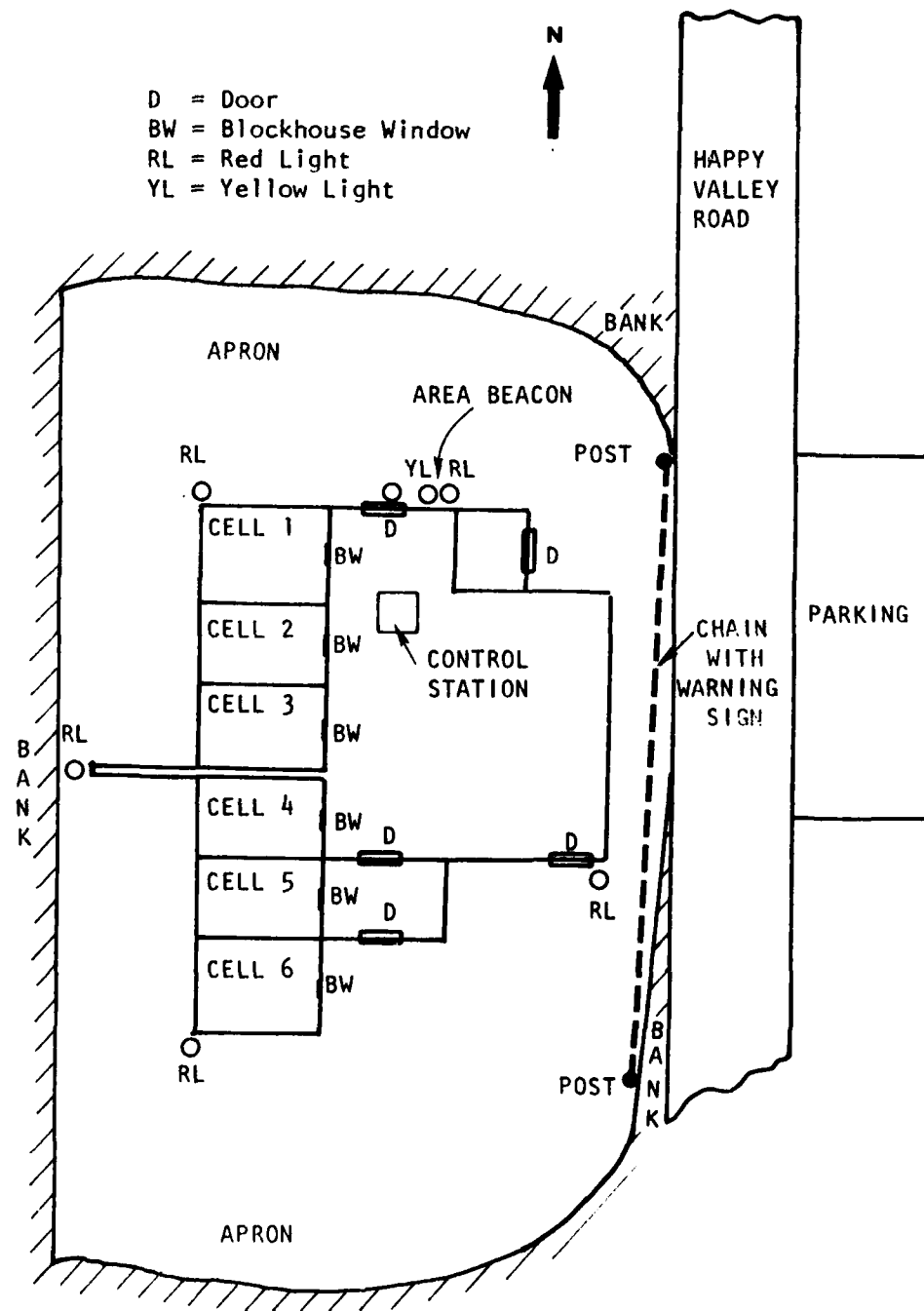


Figure 8. Building 315 layout.



TABLE 3.  
GAS HANDLING SYSTEM COMPONENT LIST

Call Out (Ref. Fig. 9)	Name	Description/Type
<b>GAS BOTTLES</b>		
B1	Chlorine in helium bottle	B-size, 10% Cl <sub>2</sub> in He, maximum pressure = 718 psi
B1.A	Chlorine bottle	Size 3, 15 lb liquid Cl <sub>2</sub> , vapor pressure 85.3 psig @ 70 F
B2	Helium bottle	K-size, maximum pressure = 2400 psi
B3	Hydrogen in helium bottle	B-size, 10% H <sub>2</sub> in He, maximum pressure = 700 psi
B3.A	Hydrogen bottle	Size 1A, Gaseous H <sub>2</sub> , 800 psi
B4	Sulfur hexafluoride Bottle	Size 1A, liquid SF <sub>6</sub> , vapor pressure 320 PSIG @ 70 F
<b>REGULATORS</b>		
R1	Chlorine in Helium regulator	2-stage Matheson H15C Monel
R1.A	Chlorine regulator	2-stage Matheson H15C Monel
R2	Helium regulator	2-stage Matheson 3104
R3	Hydrogen in Helium regulator	2-stage Matheson 3104
R3.A	Hydrogen regulator	2-stage Matheson 3104
R4	Sulfur hexafluoride regulator	2-stage Matheson 9-950
<b>VALVES</b>		
V1	Chlorine in Helium bottle valve	Hand operated
V1.A	Chlorine bottle valve	Hand operated

# VALVES (continued)

V2	Helium bottle valve	Hand operated
V3	Hydrogen in Helium bottle valve	Hand operated
V3.A	Hydrogen bottle valve	Hand operated
V4	Chlorine in Helium shut off valve	Hand operated, Monel
V4.A	Chlorine shut off valve	Hand operated, Monel
V5	Helium shut off valve	Hand operated, stainless
V6	Hydrogen in Helium shut off valve	Hand operated, stainless
V6.A	Hydrogen shut off valve	Hand operated, stainless
C1	Chlorine in Helium check valve	All stainless
C1.A	Chlorine Check Valve	All stainless
C-2	Helium Check valve	All stainless
C-3	Hydrogen in Helium check valve	All stainless
C-3.A	Hydrogen Check Valve	All stainless
C4	Surflur hexafluoride check valve	All Stainless
V7	Chlorine purge	Hand operated, stainless
V8	Hydrogen purge	Hand operated, stainless
V9	Chlorine fill valve (normally closed)	Air operated, stainless/Teflon
V10	Hydrogen fill valve (normally closed)	Air operated, stainless/Teflon
V11	Chlorine run valve (normally closed)	Air operated, stainless/Teflon
V12	Hydrogen run valve (normally closed)	Air operated, stainless/Teflon
V13	Chlorine Throttle valve	Hand operated, stainless (9 turns)
V14	Hydrogen throttle valve	Hand operated, stainless (9 turns)



## VALVES (continued)

V15	Bomb valve (normally closed)	Air operated, stainless/Teflon
V16	Vacuum valve (normally closed)	Air operated, stainless/Teflon
V17	Pump valve	Hand operated, stainless
V18	Bleed valve	Hand operated, stainless
V19	Chlorine regulator purge valve	Hand operated, monel
V20	Chlorine regulator vent valve	Hand operated, monel
V21	Chlorine isolation valve	Hand operated, monel
V22	IC1 Fill valve (normally closed)	Air operated, stainless/Teflon
V23	Transducer inlet valve	Hand operated, stainless
V24	Transducer bypass valve	Hand operated, stainless
V25	IC1 Shut-off valve	Hand operated, glass/Teflon
V26	Reference vacuum valve	Hand operated, stainless
V27	Pump bleed valve	Hand operated, stainless
V28	Sulfur hexafluoride bottle valve	Hand operated
V29	Sulfur hexafluoride shut off valve	Hand operated

## INSTRUMENTS

P1	Chlorine fill pressure	Heise 0-30 psig, read through blockhouse window
P2	Hydrogen fill pressure	Heise 0-60 psig, read through blockhouse window
P3	Bomb load pressure	Heise 0-50 psia, read through blockhouse window

# INSTRUMENTS (continued)

P4	Reference pump vacuum gauge	Hastings thermocouple gauge, read out unit at pump
P5	System vacuum gauge	Hastings thermocouple gauge, readout unit in blockhouse
P6	ICI fill pressure	Validyne reluctance manometer Model DP15-43, readout unit viewed through blockhouse window
TC1	Mixer temperature	C.A. thermocouple, readout in blockhouse
TC2	Photolysis reactor temperature	C.A. Thermocouple readout in blockhouse
XD1	Transducer, measure cell pressure increase after flashlamp discharge	Model S-102A15 Quartz Transducer PCB Piezotronics

cation with the blockhouse operator able to view gauges indicating pressures P1, P2, P3, and P5.

The gases in the run tanks were then admitted to the photolysis cell by remote operation of valves V-11, V-12, V-15, and V-16. Control of the flow to the cell was accomplished by presetting the throttling valves V13 and V14. Background pressures of less than 50 m torr were achieved in all parts of the systems except the  $\text{Cl}_2$  run tank  $T_1$ , which could be pumped to only about 300 m torr. The pressure gauges P1, P2, and P3 were Bourdon-tube type gauges manufactured by Heise. They had either 0.1 or 0.2 lb/in<sup>2</sup> scale divisions. The gauge used to read P3, the photolysis cell, was of the absolute pressure type and had 0.2 lb/in<sup>2</sup> divisions but could easily read to 0.1 lb/in<sup>2</sup>. The zero was set daily and an error of < 1.5% (actual - reading) was typically observed at the local atmospheric pressure of about 13.7 lb/in<sup>2</sup>.

There was no attempt made to correct the pressure readings in presenting or interpreting the data. Based on this, it was possible to add gas to the cell with uncertainties on the initial and final pressure readings of < 5 torr and an absolute error on the initial and final pressure of about 1.5%.

#### PHOTOLYSIS CELL

Two different photolysis cells were used during the program, in connection with the two flashlamp systems which were used. In the first, the flashlamp was internal to the cell while the second was placed adjacent to the flashlamp. Both cells were cylindrical in shape and of stainless steel construction.

##### Internal Lamp Configuration

The final configuration of this cell is shown in Figure 10. The body of the cell and the endcap on the ground end were of stainless steel construction. The endcap on the high voltage end was made of Teflon and was grooved on its inner surface to alleviate a discharge problem noted along a smooth Teflon surface. Viton O-rings were used on sealing surfaces. The lamp electrodes were pressed into stainless steel clips which were threaded onto stainless steel rods for electrical connection. One port was provided for evacuation

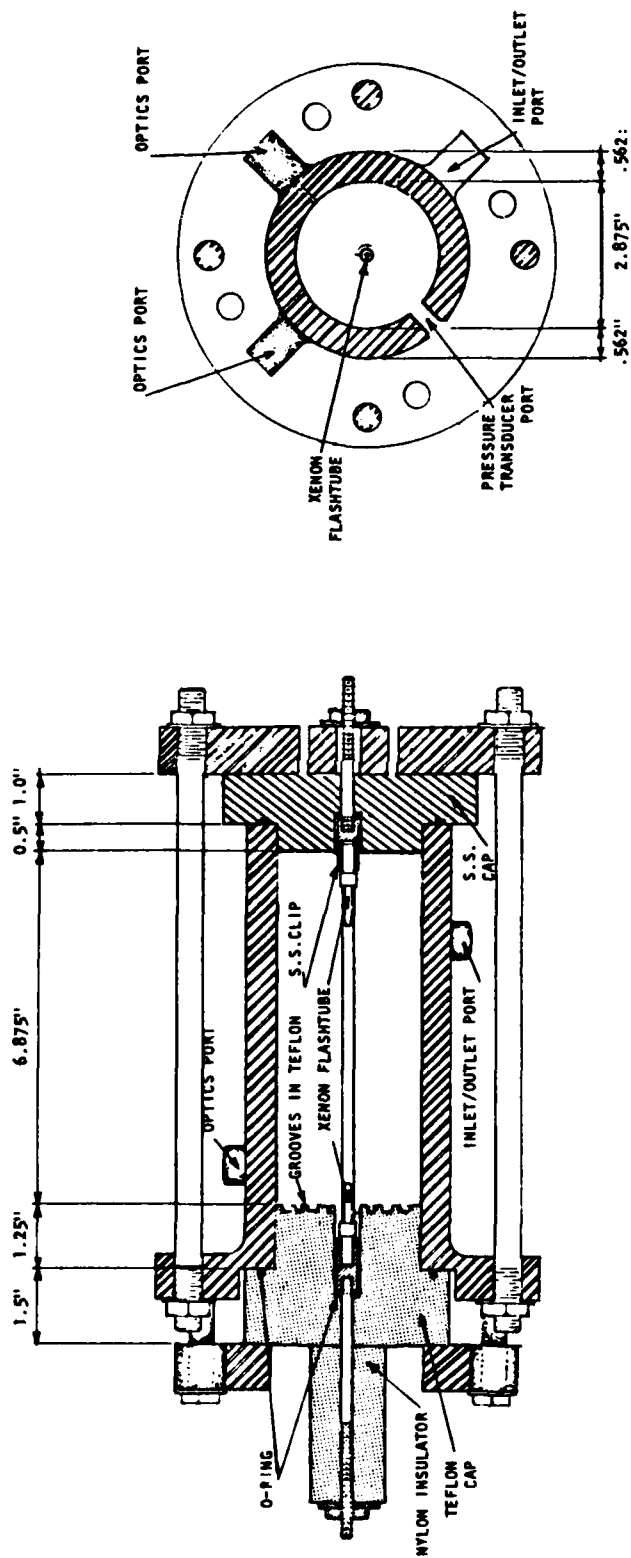


Figure 10. Photolysis reactor with internal flashlamp.

and fill as shown. Two other ports were used for optical access and a fourth port was used for the pressure transducer. The total volume of the cylindrical portion of this cell was  $731 \text{ cm}^3$ . Other volume factors included the flashlamp at about  $5.5 \text{ cm}^3$ , and the ports and fill system volume between the cell and last valve seat, estimated at  $20\text{--}25 \text{ cm}^3$ . The dimensions of the lamp capillary were 12.7 cm long, 0.3 cm I.D., 0.7 cm, O.D. Thus, the cylindrical area over which light was admitted to the cell volume at the flashlamp outer surface was  $4.9 \text{ cm}^2$ .

#### External Lamp Configuration

The final configuration of this cell is shown in Figure 11. The cell was constructed of heavy wall stainless steel with Suprasil windows cemented on the ends with silicone rubber cement (Red RTV). There were two holes through the cell sidewall as shown; one for an insulated pressure transducer, and one for connection to the gas handling system. The volume of this cell was  $64.1 \text{ cm}^3$ . The volume of the delivery line from the cell to the seat of the last valve was estimated to be less than  $3 \text{ cm}^3$ . The area of the window was  $6.4 \text{ cm}^2$ .

#### CELL AND LAMP DIAGNOSTICS AND DATA SYSTEM

In order to characterize the deposition of flashlamp energy into the gas in the photolysis cell and the subsequent thermalization of that energy, certain time dependent measurements were made. These are discussed in the following paragraphs.

#### Voltage and Current Measurements

The voltage waveform across the small flashlamp was measured by measuring the voltage across a 2000:1 high voltage probe which was connected in parallel with the lamp. The probe was a LANL design rated to 100kV. Although the 2000:1 ratio was verified using lower DC voltages, it was not checked up to 10kV on this program. Therefore, it is possible that discrepancies noted between observed voltage peaks and capacitor charging voltages at 10 kV could be attributed to this probe. These discrepancies are discussed later under small flashlamp system electrical characterization.

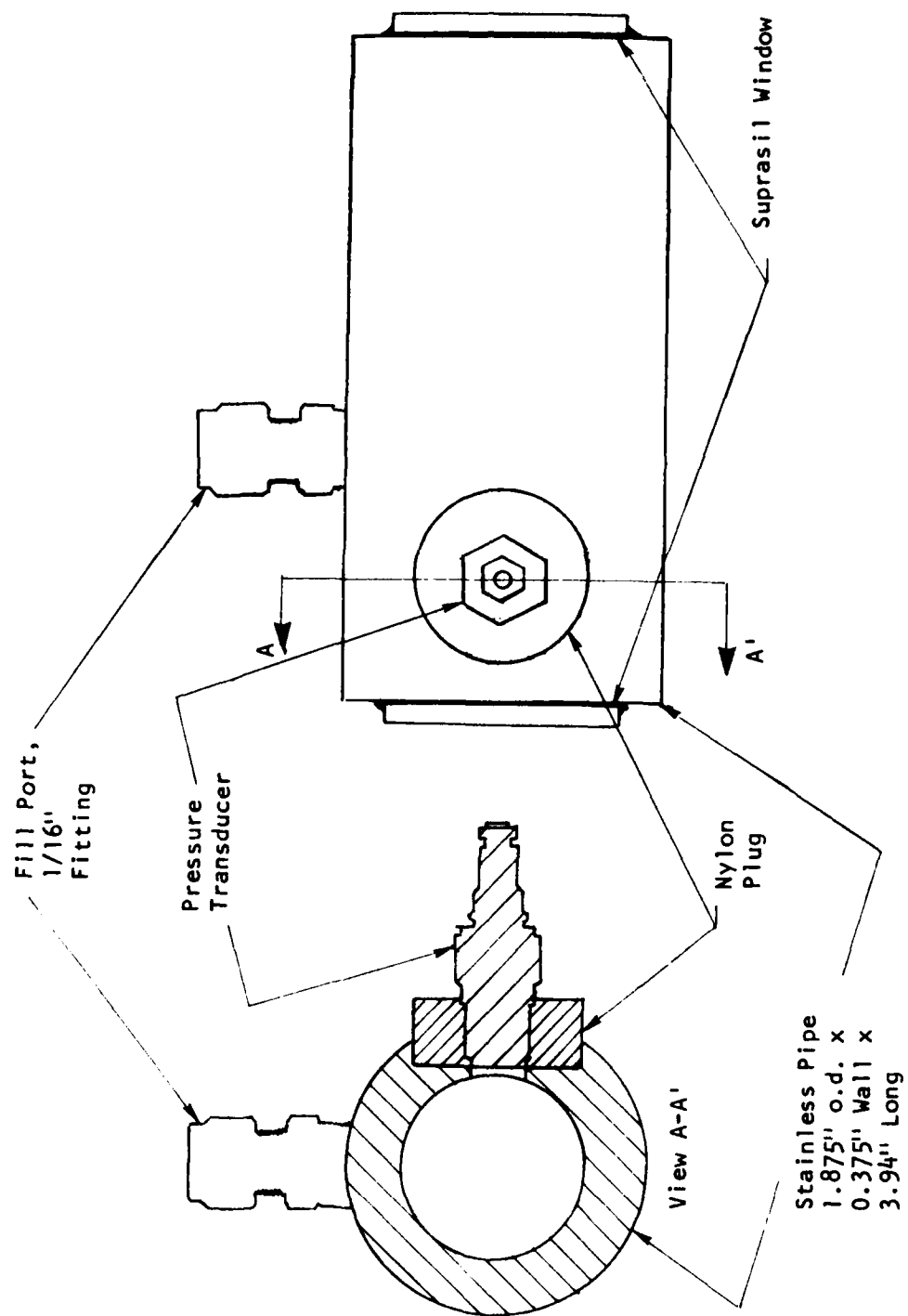


Figure 11. Photolysis cell for use with external flashlamp.

Current through the lamp was measured by observing the waveform output from a 100 A/V current transformer manufactured by Pearson Instruments. The transformer was mounted around the lamp high voltage electrode on the outside of the photolysis reactor. A 10X attenuator was used on the signal prior to input to the data system.

The voltage waveform across the large flashlamp was measured by recording the output from a 895:1 voltage probe provided by the vendor. Current measurements were not recorded with this system.

#### Optical Measurements

Two optical channels provided time-dependent waveforms of the flashlamp pulse in two wavelength bands. Each channel consisted of a quartz fiber bundle with one end collecting flashlamp radiation after passage through the reactor volume. The fibers transmitted the light into the control station and onto silicon photodiode detectors. Interference filters at the detector end were selected to pass light near the maximum of the halogen absorption ( $\lambda = 334$  nm for  $\text{Cl}_2$  and  $\lambda = 500$  nm for  $\text{ICl}$ ) for one channel and to pass light beyond the absorption ( $\lambda > 550$  nm for  $\text{Cl}_2$  and  $\lambda = 650$  nm for  $\text{ICl}$ ) for the other. Neutral density filters (N.D. = 3.0), were installed on the long wave pass channel to avoid detector saturation when the  $\lambda > 550$  nm filter was used. The systems are shown schematically in Figures 12 and 13. Optical filter characteristics are shown in Figures 14 - 17. Spectral response of the detectors, designated as UV enhanced, is shown in Figure 18. The detectors were used with either the 3 K  $\Omega$  or 10 K  $\Omega$  feedback resistor. It was verified using pulsed LED inputs that the detector rise and fall time were well under 1  $\mu\text{s}$ .

#### Pressure Measurements

Dynamic pressure rise in the photolysis cell following flashlamp discharge was monitored using a Model S-102A15 quartz transducer manufactured by PCB Piezotronics. The unit had a natural frequency of 425 kHz, a rise time of 1  $\mu\text{s}$ , an average response of 23.1 mV/psi and a linearity of < 1% of full scale (100psi full scale). The linearity, based on the calibration data provided, was much better than that. Calibration was provided at 2 psi intervals to 10 psi and at 20 psi intervals to 100 psi.

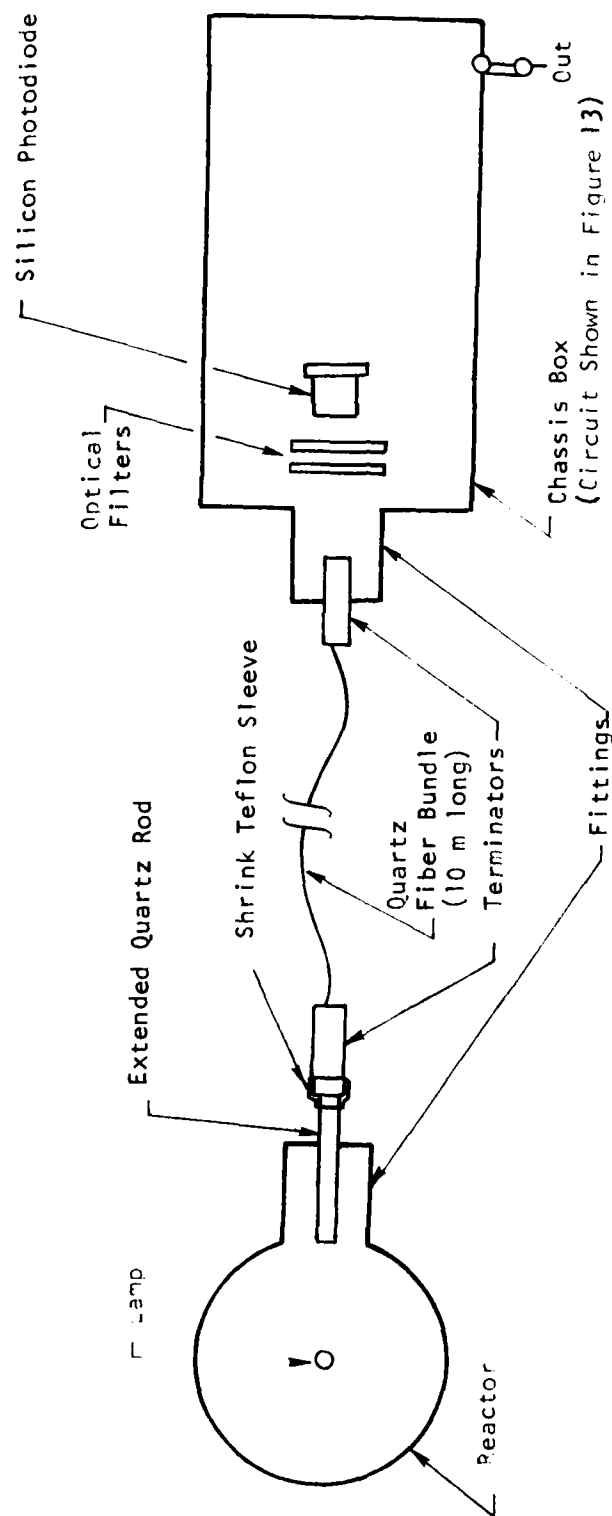


Figure 12. Optical channels as configured on photolysis reactor with internal flashlamp.



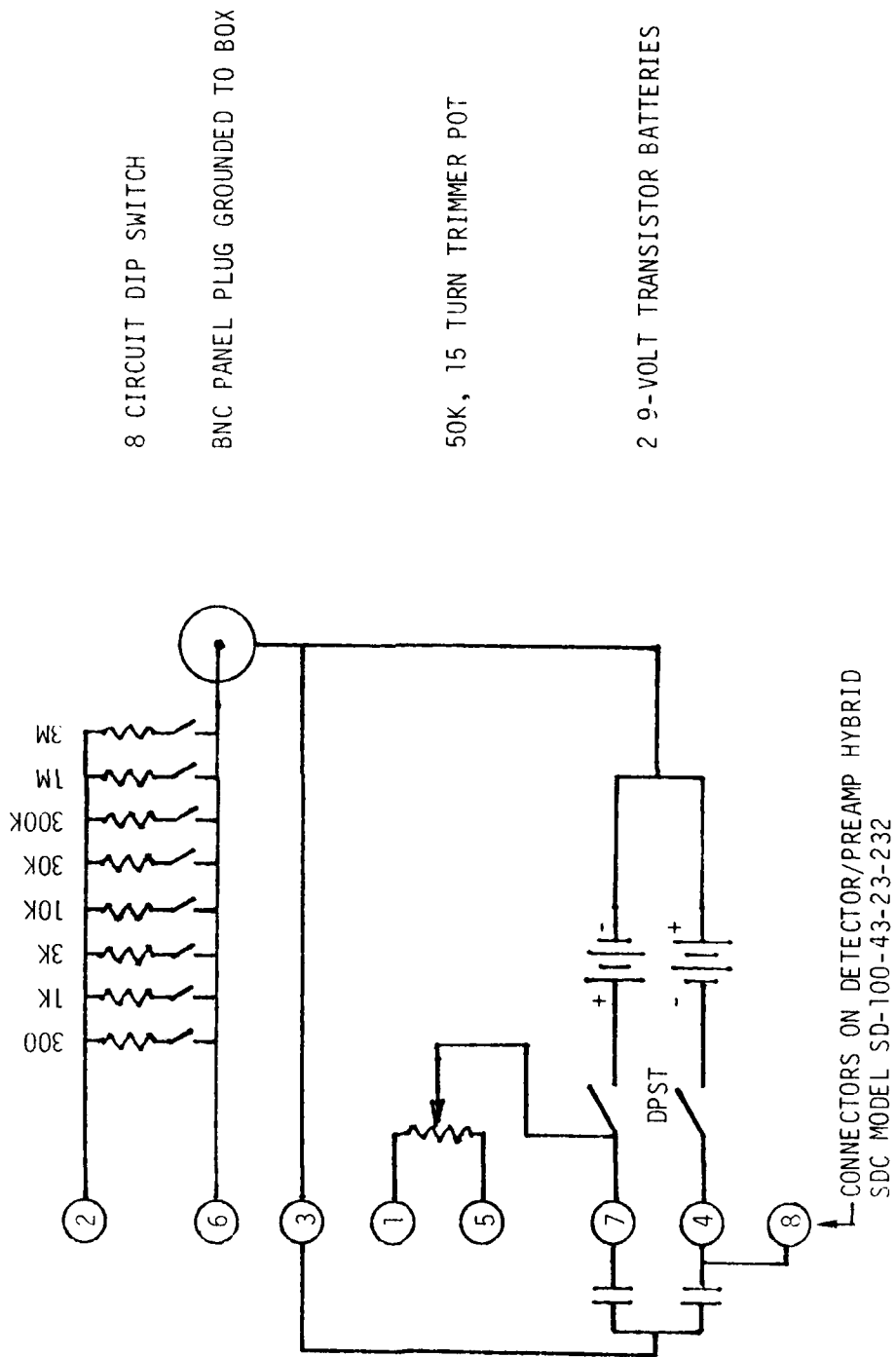


Figure 13. Photodiode detector circuit.

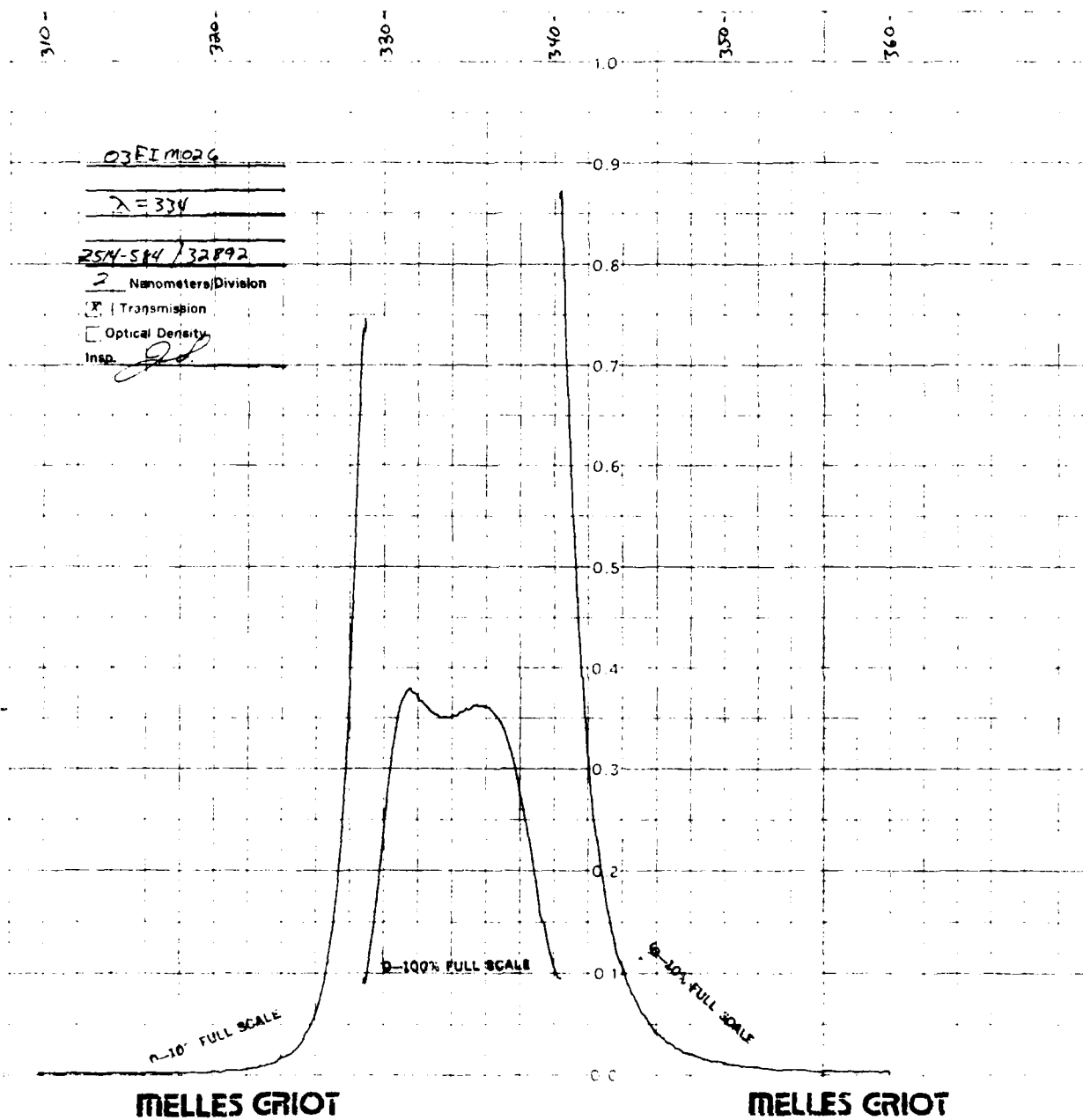


Figure 14. Transmission of 334 nm bandpass filter  
(Cl<sub>2</sub> absorption maximum).

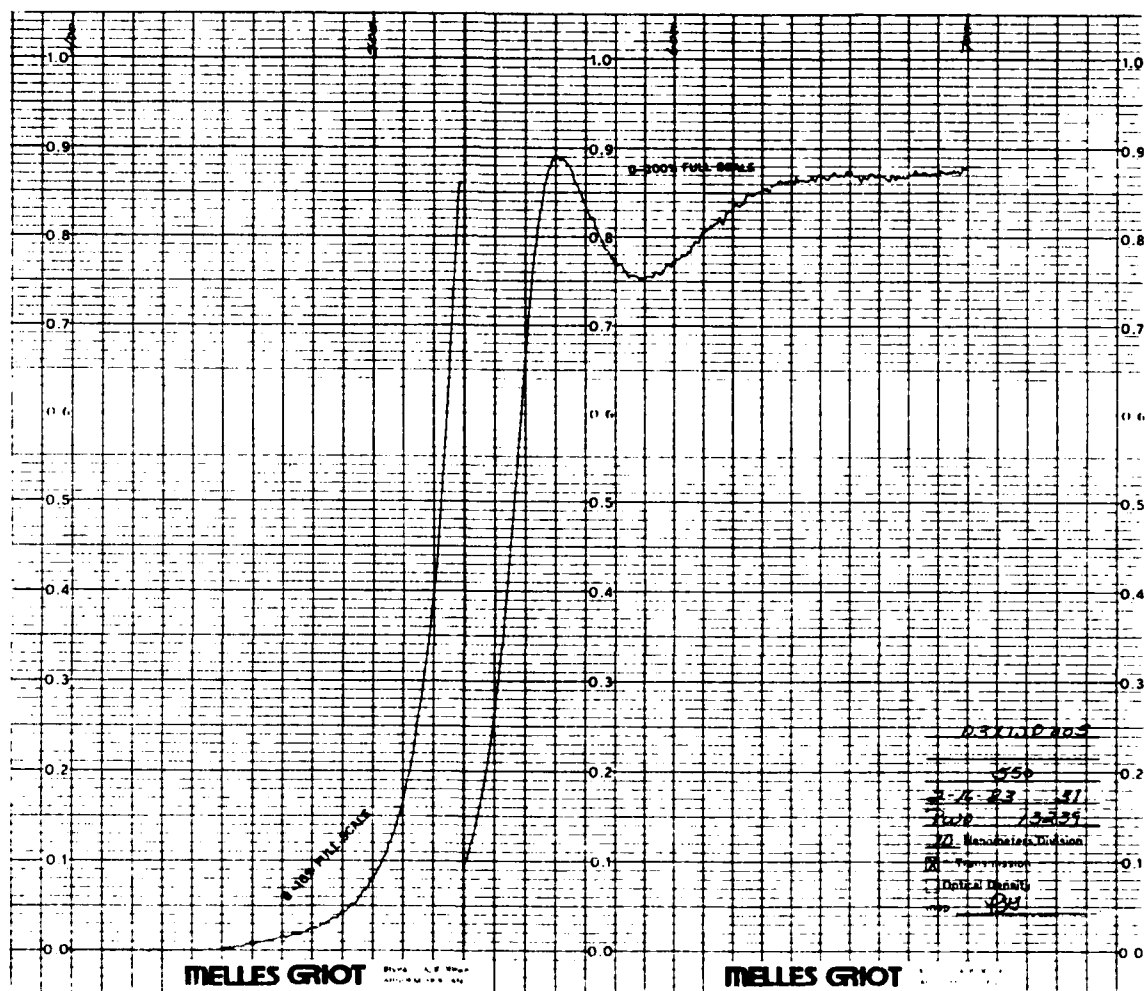


Figure 15. Transmission of 550 nm long wave pass filter (negligible Cl<sub>2</sub> absorption).

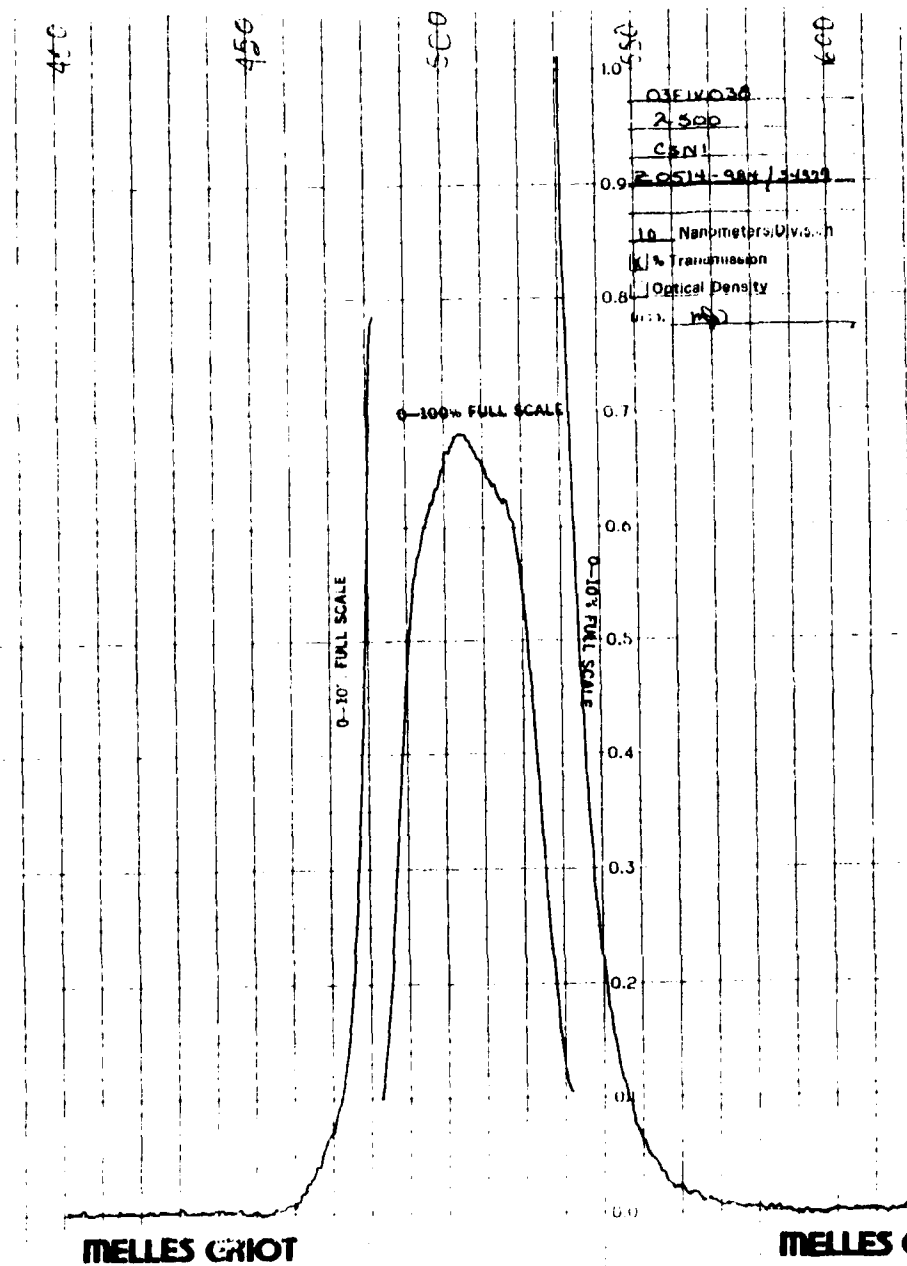


Figure 16. Transmission of 500nm bandpass filter (high ICl absorption).

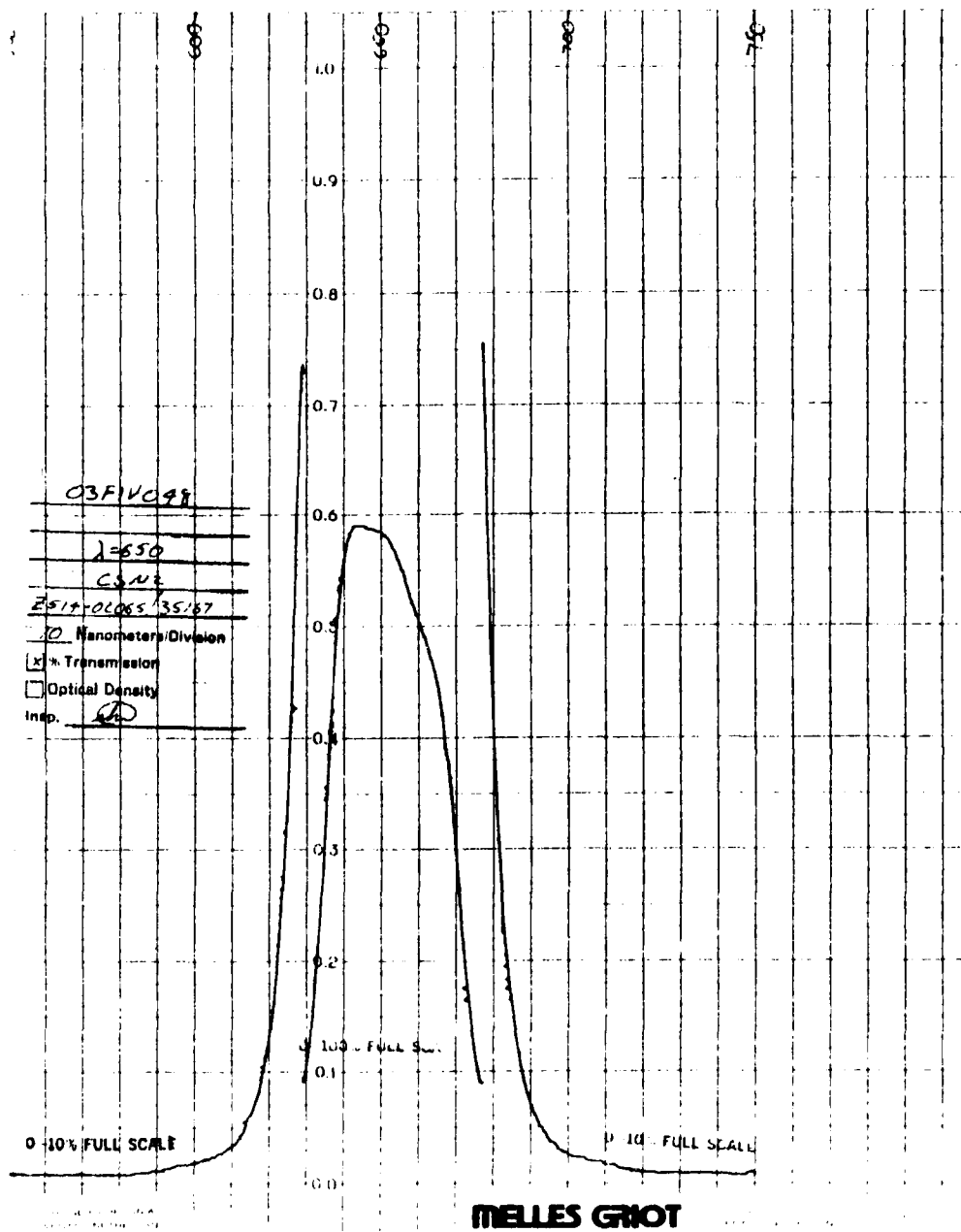


Figure 17. Transmission of 650nm bandpass filter  
(negligible ICl absorption high  $I_2$  absorption)

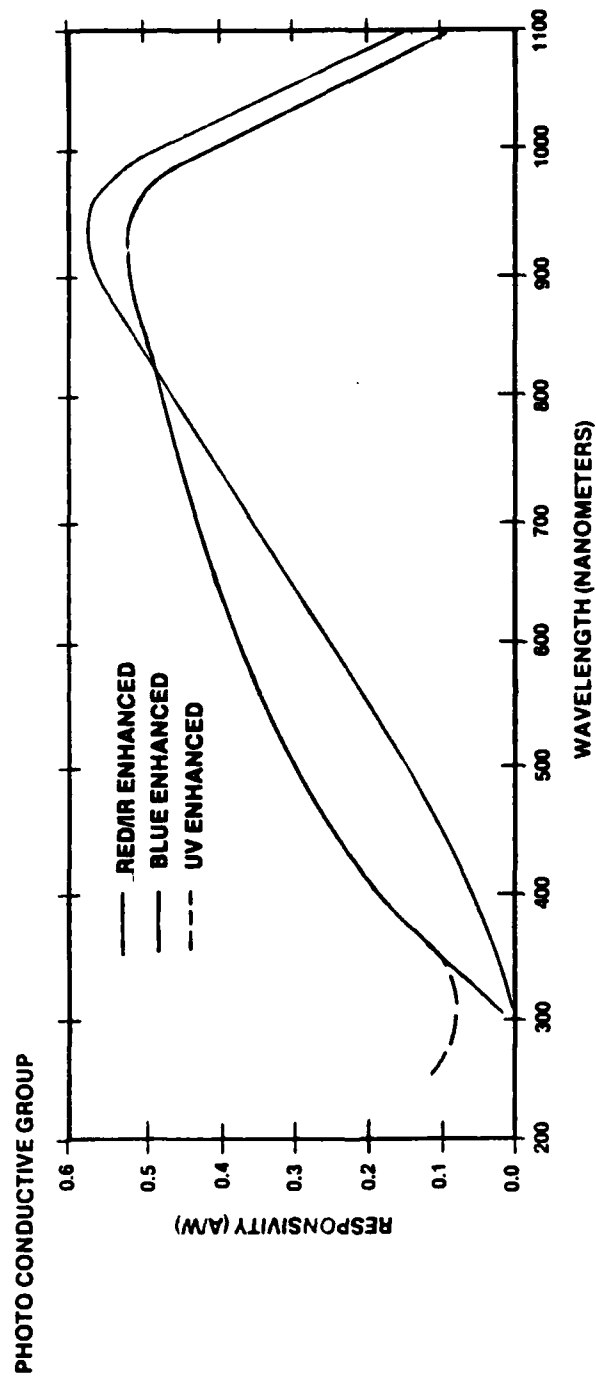


Figure 18. Detector spectral response.

Difficulties were encountered with electrical and thermal interferences. The electrical problems were alleviated by mounting the transducer in a nylon bushing instead of in the steel reactor, as shown earlier in Figure 11. The thermal problem was alleviated by covering the stainless steel transducer diaphragm with Teflon tape, thereby providing thermal insulation which held off the thermal shock until after the critical pressure rise data was collected.

#### Data Acquisition System

Time dependent signals were recorded using a Model 4094 four channel digital recording oscilloscope manufactured by Nicolet. Data rates up to 0.5 $\mu$ s per point on all four channels were available. A Model XF-44 dual-drive floppy diskette recorder was available for recording the data from each test.

#### FLASHLAMP DRIVER AND FLASHLAMP

Two different xenon flashlamp systems were used in this program. The first was based on a small flashlamp mounted inside a cylindrical cell, as shown earlier in Figure 10. The second system was based on a larger flashlamp which was placed adjacent to the cell shown in Figure 11.

#### Small Flashlamp System ( $\leq 100$ J Discharge)

The driver for this system was a Model 457 A Micropulser manufactured by the Xenon Corporation. This unit was equipped with capacitors of 0.5  $\mu$ F and 2  $\mu$ F which could be charged up to 10kV, thus providing up to 100J of discharge energy.

The flashlamps were also manufactured by Xenon and carried the designation S-1084. The capillary section of the lamp was 12.6 cm long x 7mm O.D. (3mm I.D.). The flashlamps were filled with xenon to a pressure of 300 torr. The system was modified as follows to accommodate operational and performance requirements of the experiments.

1. Remote operation of the high voltage on-off function was added to satisfy some procedural requirements.

2. A remote trigger switch circuit with a synchronizing pulse output was added to reduce time delay jitter, eliminate switch bounce effects, and reduce electrical interference carried by the synch pulse.
3. A capacitor of 200 nF was installed across the flashlamp to provide a higher voltage peak at the beginning of the discharge to improve lamp ignition. A 500  $\Omega$  bleed resistor was installed across this capacitor.
4. The braided cable on the ground return from the lamp was replaced with 2" wide copper sheet in an attempt to narrow the discharge waveform.

A trigger wire was installed for all of the lamp firings made with the 100 J flashlamp system. Several hundred lamp firings were recorded with this system, more than half of them at 100 J. Reproducibility of the electrical and optical characteristics was quite good, with no lamp failures encountered. The overall experimental arrangement for the experiments conducted with this system is shown in Figure 19.

#### Large Flashlamp System

The large flashlamp system was manufactured to Rocketdyne specifications by the Pulsar Products Division of Physics International Corporation. The flashlamps were designated as Model L-4258 and were manufactured by ILC Technology Inc. These lamps were filled with 30 torr of xenon, had an O.D. of 24mm, an I.D. of 19mm, and an electrode spacing of 100 cm. The overall experimental arrangement for the experiments conducted with this system is shown in Figure 20.





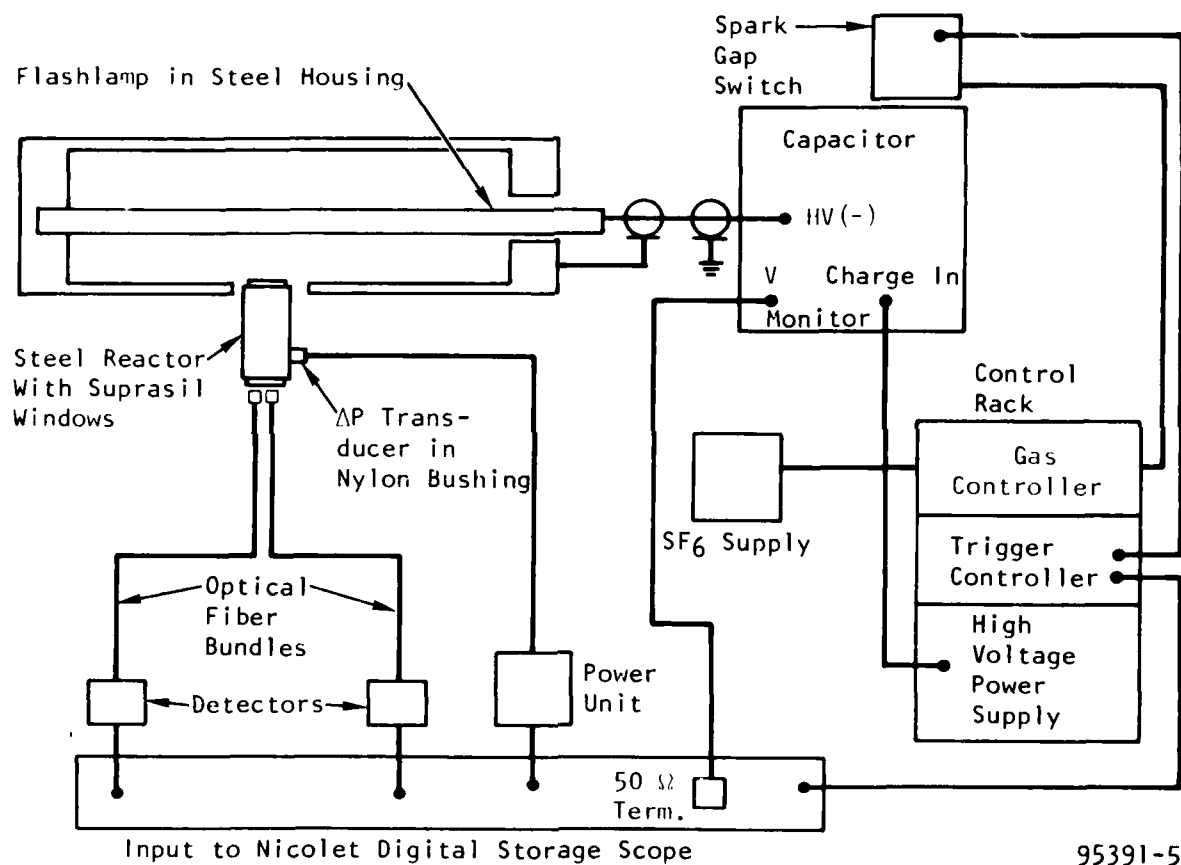


Figure 20. Overall arrangement for 9kJ flashlamp experiments,

## OBSERVATIONAL RESULTS

This section of the report is a presentation and discussion of the experimental results which were obtained during the program. The discussion includes estimates and comments on the quality of the raw data and methods used to reduce the data to physical observables. The discussion begins with a characterization of the operation and performance of the flashlamps. Then energy deposition and release results are presented.

### FLASHLAMP CHARACTERIZATION

#### Electrical Energy Deposition in the Small Flashlamp System

All of the small flashlamp system testing discussed in this report was done with a 2  $\mu\text{F}$  capacitor installed in the Xenon Corporation Model 457A Micropulser. Front panel meter voltage settings of 5000, 7000, or 10000 V were used, giving nominal discharge energies ( $1/2 CV^2$ ) of 25J, 49J, and 100J. Early in the testing, difficulties were encountered in obtaining reliable lamp firings due to shorting or arcing inside of the photolysis reactor. A number of steps were taken to alleviate this problem, including the addition of  $\text{SF}_6$  to the gas fill. It was discovered that at least 100 torr of  $\text{SF}_6$  was needed to suppress the unwanted arcing. Therefore, all tests reported with this system included 100 torr or more of  $\text{SF}_6$  in the photolysis reactor. The role of this gas as a heat sink and kinetics participant was not particularly desirable and moderated observed pressure rises through both kinetic and thermal effects, as discussed later. However, its role as an arc suppressor was very beneficial.

Figure 21 shows the recorded current and voltage waveforms for a 10000V lamp discharge with a 16 psia fill of  $\text{SF}_6$  in the cell. Also shown is the integral of  $V(t) \cdot I(t) dt$  performed by the Nicolet.<sup>(a)</sup> The spike on the front of the

#### (a) NOTE FOR INTERPRETATION OF GRAPH SYMBOLS

The Nicolet Digital Oscilloscope and the associated Hewlett-Packard x-y Digital Plotter were used regularly in recording, manipulating, and displaying the experimental data. The graphs produced by this data system are used

Date: 12/12/84

Run: 17/2

Fill: ~ 16 psia SF<sub>6</sub>

Voltage Setting: 10 kV

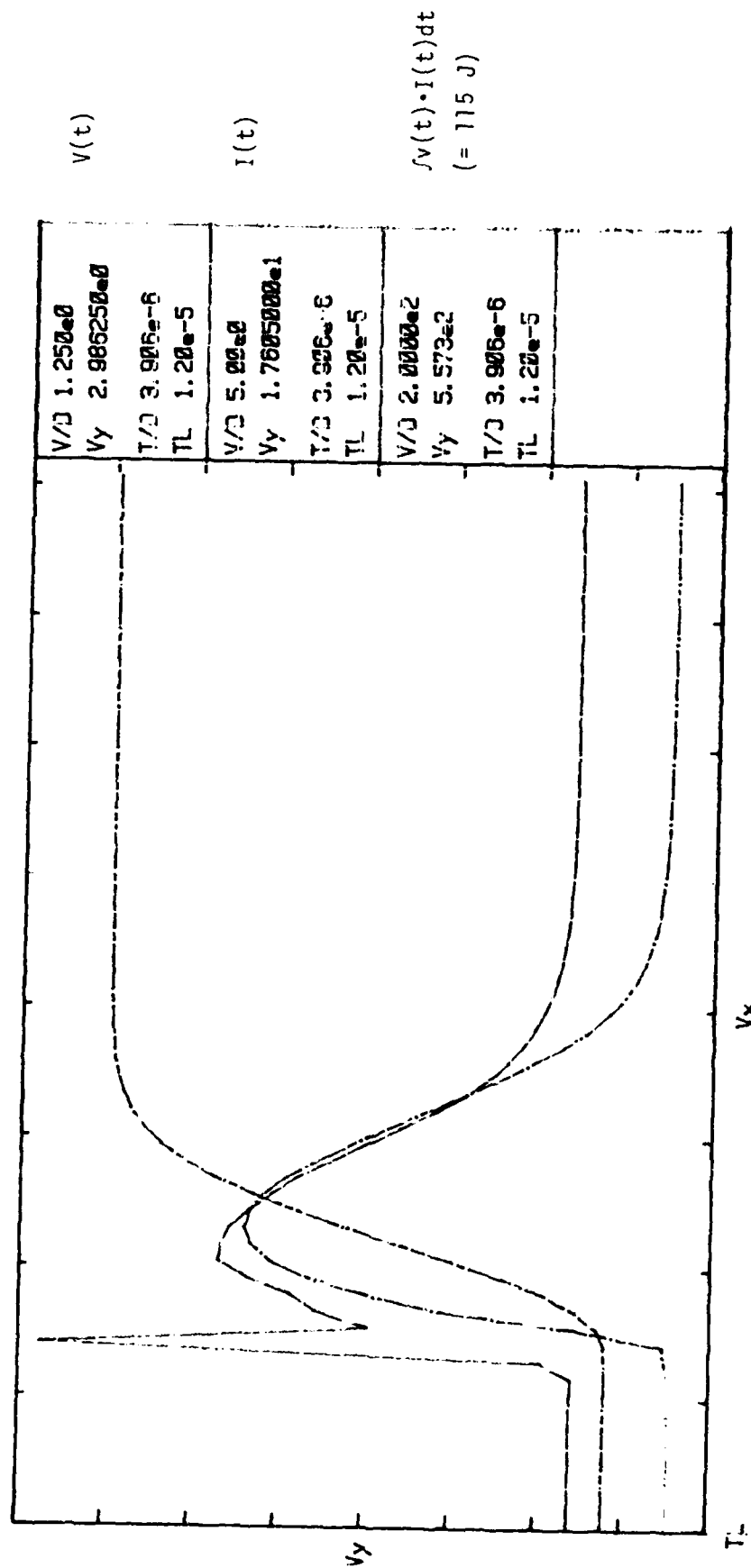


Figure 21. Electrical characteristics of 10 kV lamp discharge.

voltage waveform is caused by the peaking capacitor discussed earlier. This spike contributes very little energy but helps to initiate lamp firing.

The waveforms for 5 kV and 7 kV runs are similar but distinctive, as may be seen from the examples in Figures 22 and 23. The principal effects on the V and I waveforms of increasing the voltage and energy of the discharge are to narrow the waveforms and to move the peaks to earlier times, with the larger effect being seen between 5 kV and 7 kV.

Several aspects of the electrical energy deposition performance are plotted in Figure 24, which is a composite of data from 35 runs made on December 12, 1984. The parameters plotted are the peak values of lamp current and voltage, the value of the leading voltage spike, and the time integral of the voltage-current product, which is the energy deposited. Also plotted for comparison are the set voltage from the Micropulser panel meter and the stored energy,  $1/2 CV^2$ , based on this value. Data for each parameter are plotted as a maximum, minimum, and average from the runs for each voltage setting, with 11 runs at 5 kV, 8 runs at 7 kV, and 16 runs at 10 kV being included.

(a) (footnote cont'd.)...frequently in this report. This note is intended to facilitate reading these graphs. Four plots can be made per graph and the four boxes on the right of the graph provide relevant information. The right hand edge of each box shows the type of line used to plot the parameter, with scaling information given by the lettering inside each box as follows:

- V/D is the volts/division on the vertical axis (normally a calibration factor is then required to convert to engineering units)
- $V_y$  is the voltage value assigned to the central tick on the vertical axis
- 1/D is the time in seconds per division along the horizontal axis
- 1L is the absolute time value assigned to the left hand end of the time axis
- $V_x$  has no meaning in a plot of a waveform vs time.

Date: 12/12/84  
 Run: As Noted  
 Fill: 16 psia SF<sub>6</sub>  
 Voltage Setting: As Noted

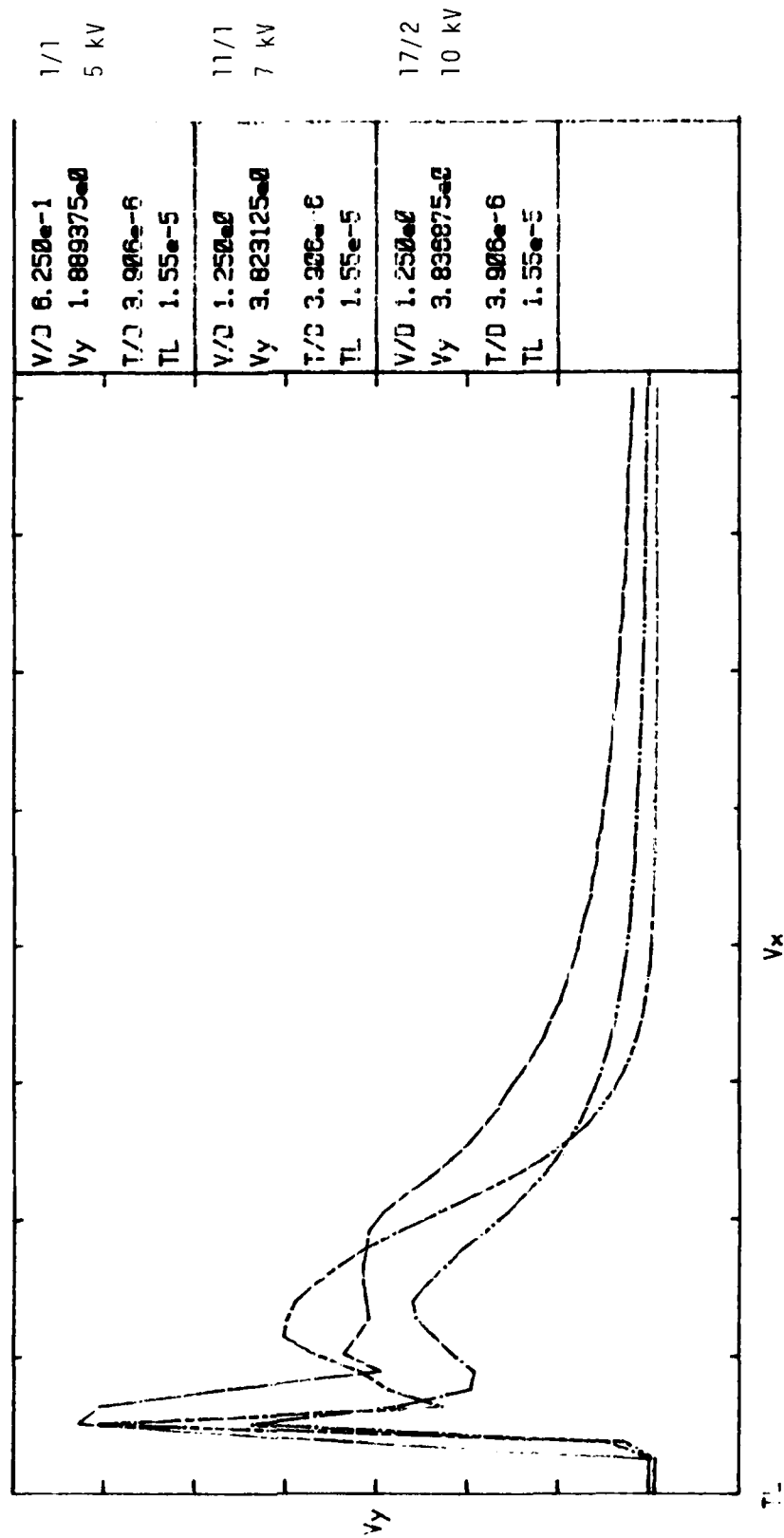


Figure 22. Lamp voltage waveforms for 5, 7 and 10 kV discharges.

Date: 12/12/84  
 Run: As Noted  
 Fill: 16 psia SF<sub>6</sub>  
 Voltage Setting: As Noted

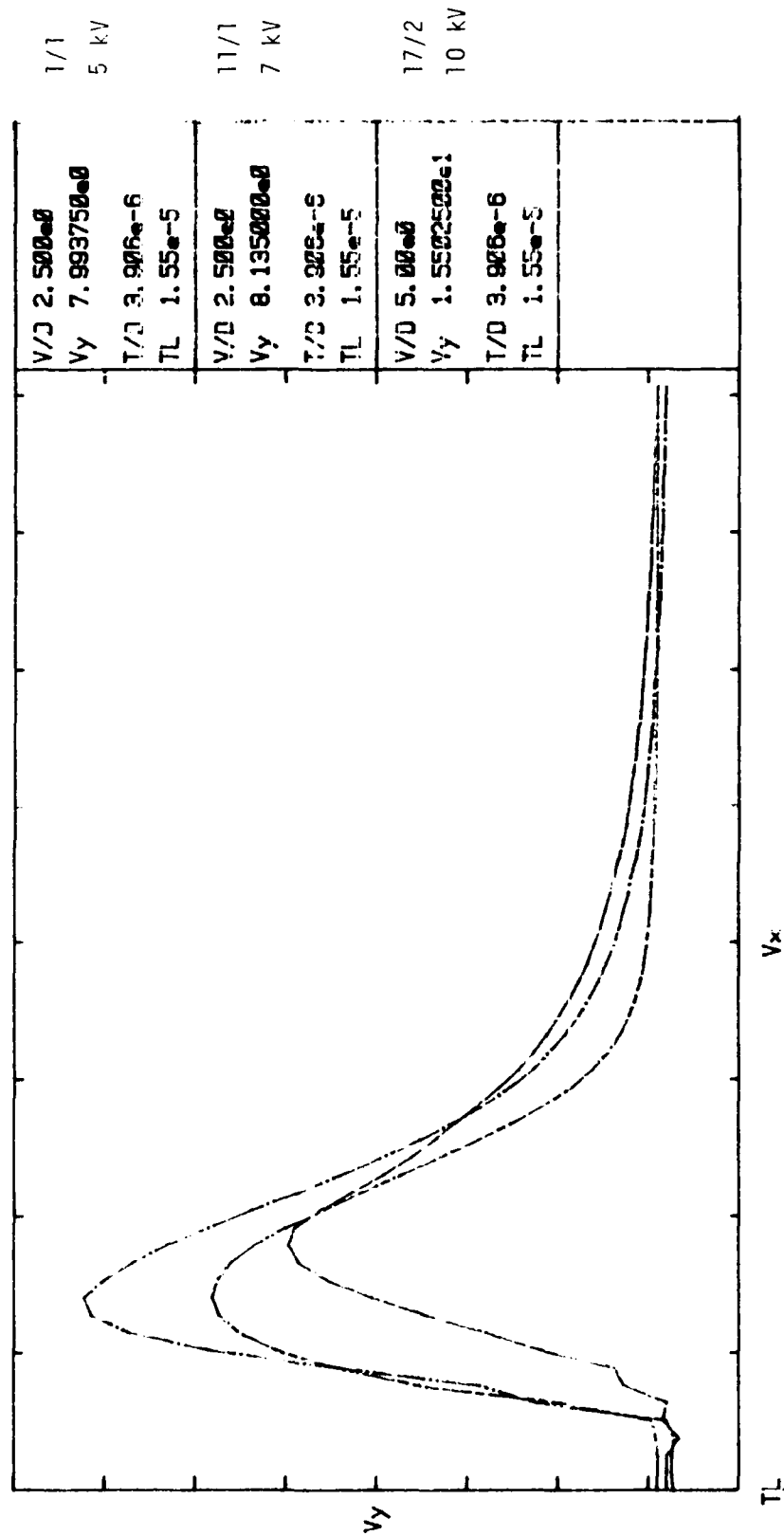


Figure 23. Lamp current waveforms for 5, 7 and 10 kV discharges.

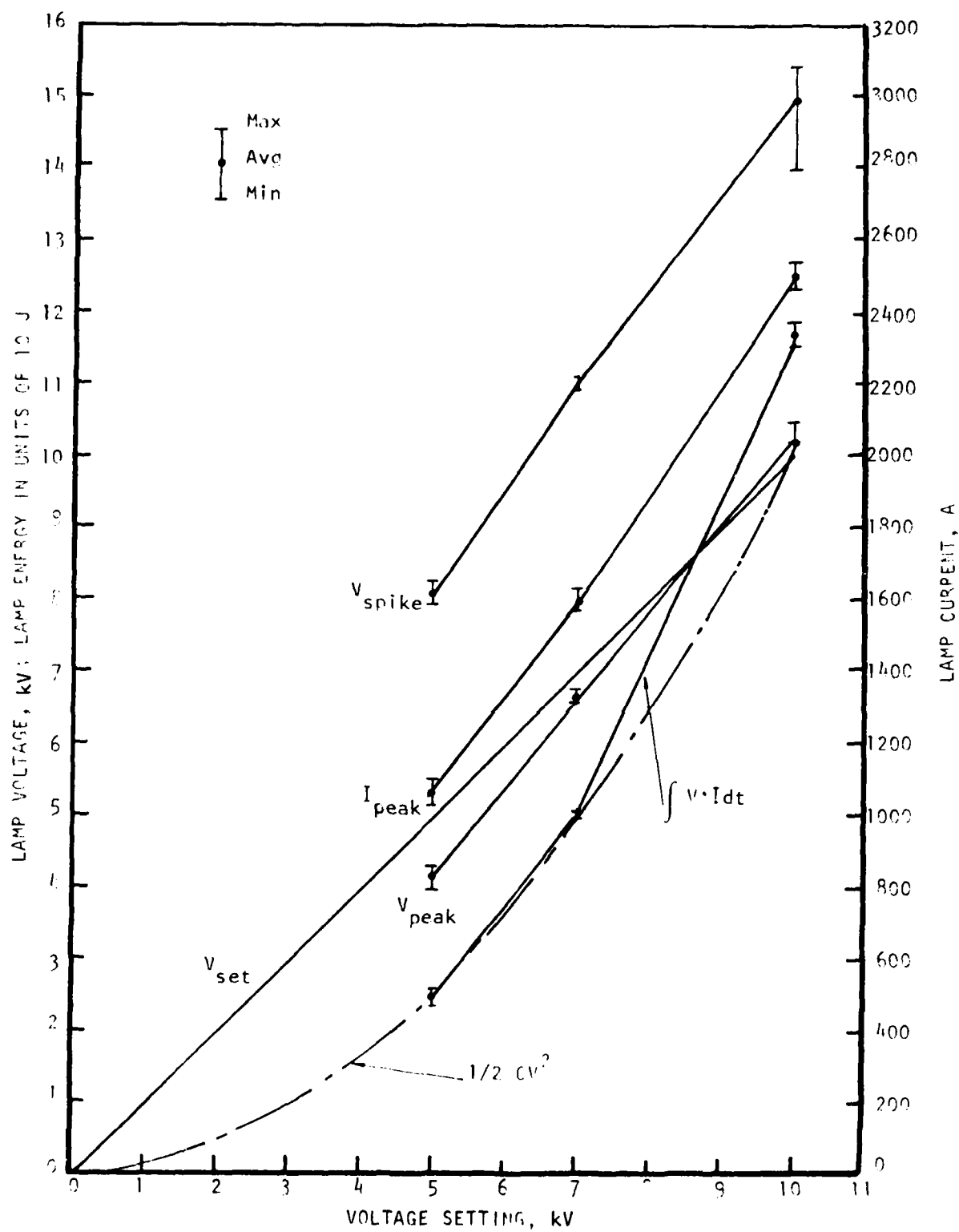


Figure 24. Lamp electrical characteristics (data from 12/12/84).



The groupings for each parameter at each voltage are very satisfying. A larger spread noted for  $V_{SPIKE}$  at 10 kV is caused by the fact that the spike narrows at this voltage and the 0.5  $\mu$ s data sampling rate does not always catch the peak.

$V_{PEAK}$  is about 80% of  $V_{SEI}$  at 5kV and about 102% of it at 10 kV. Although the  $V_{PEAK}$  measured across the lamp is expected to be slightly less than the capacitor charging voltage, the large deviation between the two voltages represents a discrepancy. Both the front panel meter and the LANL high voltage probe are inherently more accurate than the observed deviations. It is believed that the  $V(t)$  data was influenced by residual ground loop problems which were quite serious with this system and which had been reduced but not completely eliminated. The problems would be expected to be more serious at higher discharge energies

It should be noted that the data grouping shown in Figure 24 is for conditions ranging from 16 psia of  $SF_6$  to 4 psia of  $SF_6$  plus 2 psia of 10%  $Cl_2$  in He. For a given voltage, with  $SF_6$  in the fill, the waveforms are nearly identical for all gas fills. Figure 25 shows current and voltage waveforms at 10 kV for the extreme  $SF_6$  containing gas fills just noted. It may be seen that the reproducibility is excellent.

#### Optical Characteristics of the Small Flashlamp System

In this section, the spectral and temporal characteristics of the flashlamp light output are discussed. The observations are based on time dependent data collected using the two optical channels discussed earlier. Only the 334nm bandpass filter (Figure 14) and the 550 nm long wavepass filter (Figure 15) were used with the small flashlamp. Figure 26 shows the output from these two channels together with the voltage and current waveforms. The optical channel signals are designated  $\phi_{330}(t)$  and  $\phi_{LWP}(t)$ . Measurement of these waveforms shows widths (FWHM) of 5.8 $\mu$ s for the current, 6.6  $\mu$ s for the UV radiation, and 8.0 $\mu$ s for the visible and near IR radiation. The time-dependent integrals for electrical energy deposited into the lamp and UV and visible light out are compared in Figure 27. Both the UV and the longer wavelength light continue to be emitted after the electrical energy deposition is complete, with the long wavelength light persisting the longest. The

Date: 12/12/84  
 Run: 17/2  
 Fill: ~ 16 psia SF<sub>6</sub>  
 Charge: 10 kV

12/12/84  
 27/1  
 ~ 4 psia SF<sub>6</sub>, 2 psia 10% Cl<sub>2</sub> in He  
 10 kV

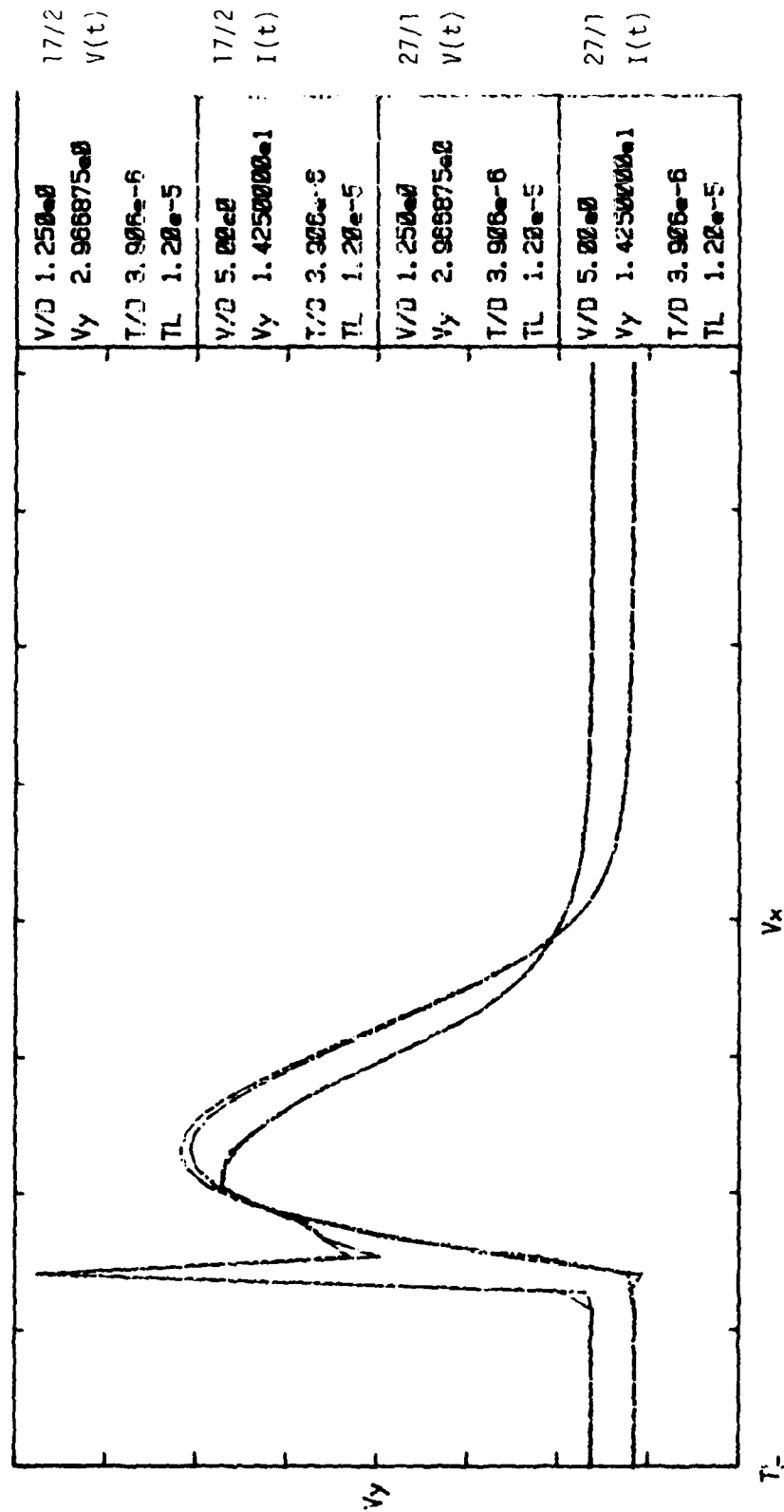


Figure 25. Reproducibility of waveforms for different gas fills with SF<sub>6</sub>.

DATE: 3/11/85

RUN: 1/2

FILL: 16 psia SF<sub>6</sub>

VOLTAGE SETTING: 10 kV

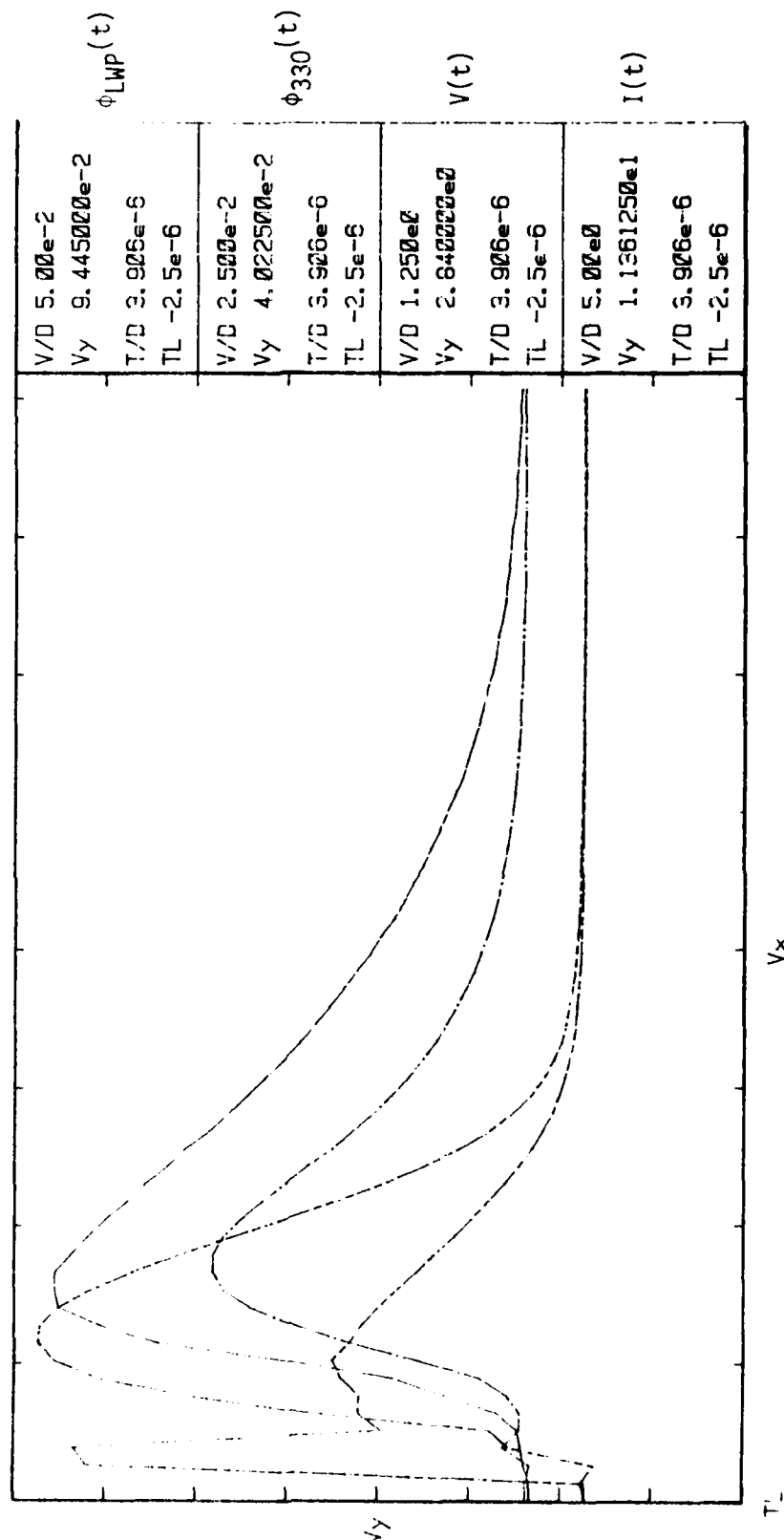


Figure 26. Electrical and optical characteristics of a 10 kV lamp discharge with no absorber.

DATE: 3/11/85  
 RUN: 1/2  
 FILL: 16 psia SF<sub>6</sub>  
 VOLTAGE SETTING: 10 kV

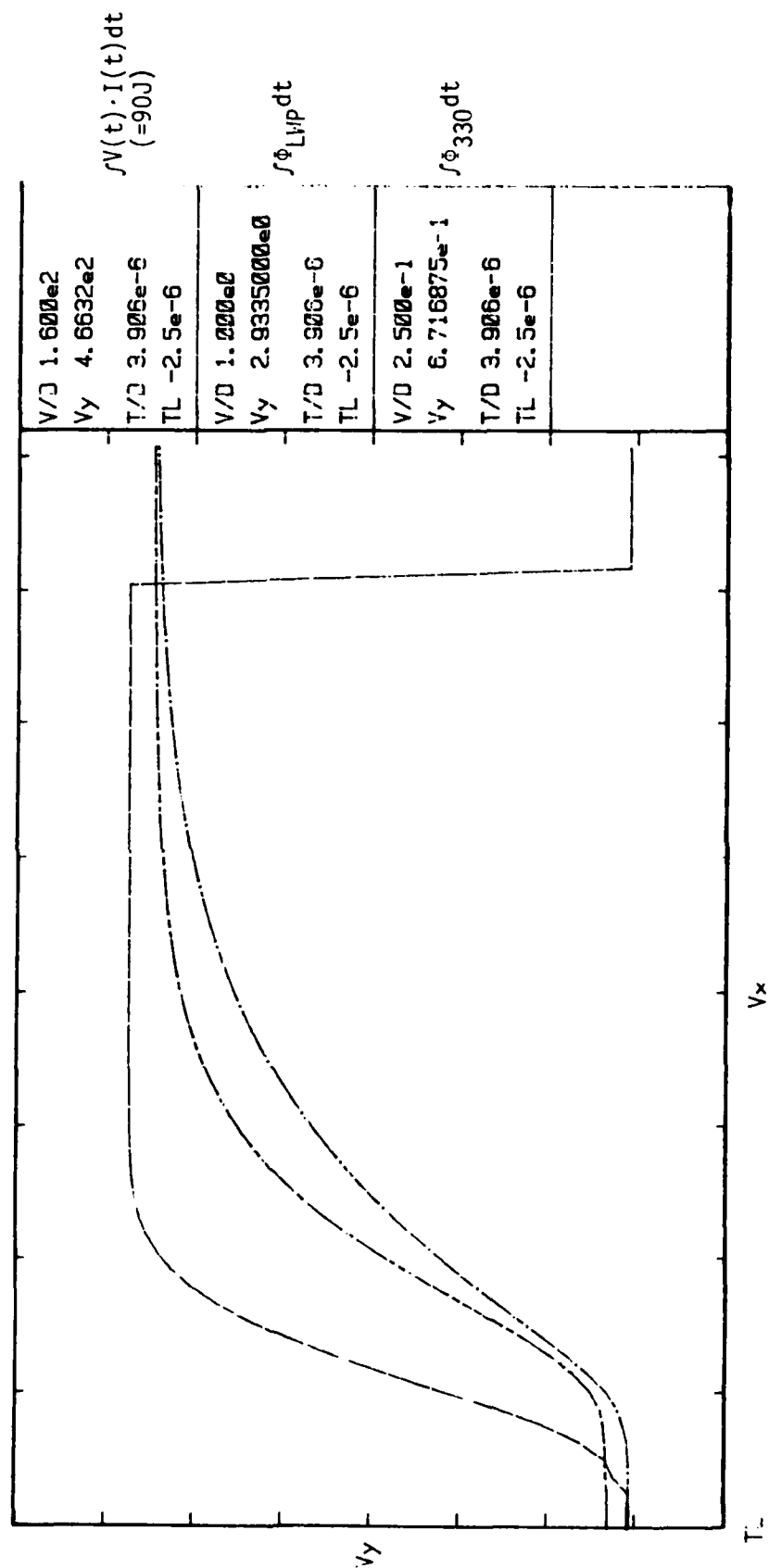


Figure 27. Electrical and optical integrals for 10 kV discharge with no absorber.

behavior observed for the UV light was in contradiction to expectations expressed by lamp vendors and their brochures. There was some concern that the waveforms were being filtered by the photodiode circuits. Tests using pulsed LEDs as sources showed that the rise and fall times of the output signals were well under one microsecond, thereby alleviating the concerns and leading to the conclusion that the waveforms accurately represent the light output. Reproducibility of the light output in the two channels was quite good, as may be seen from the waveforms shown in Figure 28.

As expected, the light output variation with electrical energy input was not the same for the UV as it was for the longer wavelength radiation. This is shown graphically in Figure 29. Time integrated output signals are plotted vs the voltage setting for  $\Phi_{LWP}$  and for  $\Phi_{330}$ . The ratio of these quantities is also plotted. As the discharge electrical energy increases by a factor of 4 (from  $1/2 CV^2 = 25$  to  $100$  J), the long wavelength light output increases by a factor of 2.8 while the light output near 330nm increases by a factor of about 7.5.

#### Electrical Energy Deposition in the Large Flashlamp System

All tests done with this system were conducted with the  $29\mu F$  capacitor charged to near 25kV ( $1/2 CV^2 \approx 9$ kJ). A current monitor was not available so that the actual energy of the discharge could not be measured. The voltage as determined from the signal out of the 895:1 voltage probe provided inside the unit was in excellent agreement with the charging voltage. The waveform of the discharge voltage at a charging voltage of 25 kV had a width (FWHM) of  $9.5 \mu s$ .

#### Optical Characteristics of the Large Flashlamp System

Figure 30 shows the waveforms for the discharge voltage; the long wavelength light,  $\Phi_{LWP}$ ; and the ultraviolet light,  $\Phi_{330}$ . The width of  $\Phi_{330}$  is  $16 \mu s$  while the width of  $\Phi_{LWP}$  is  $22.5 \mu s$ . Both the UV and the long wavelength light appear to rise at about the same rate but the longer wavelength light takes longer to decay. The large flashlamp system provided significantly more short wavelength light, as illustrated by Table 4.

DATE: 3/11/85  
 RUN: AS NOTED  
 FILL: 16 psia SF<sub>6</sub>  
 VOLTAGE SETTING: 10 kV

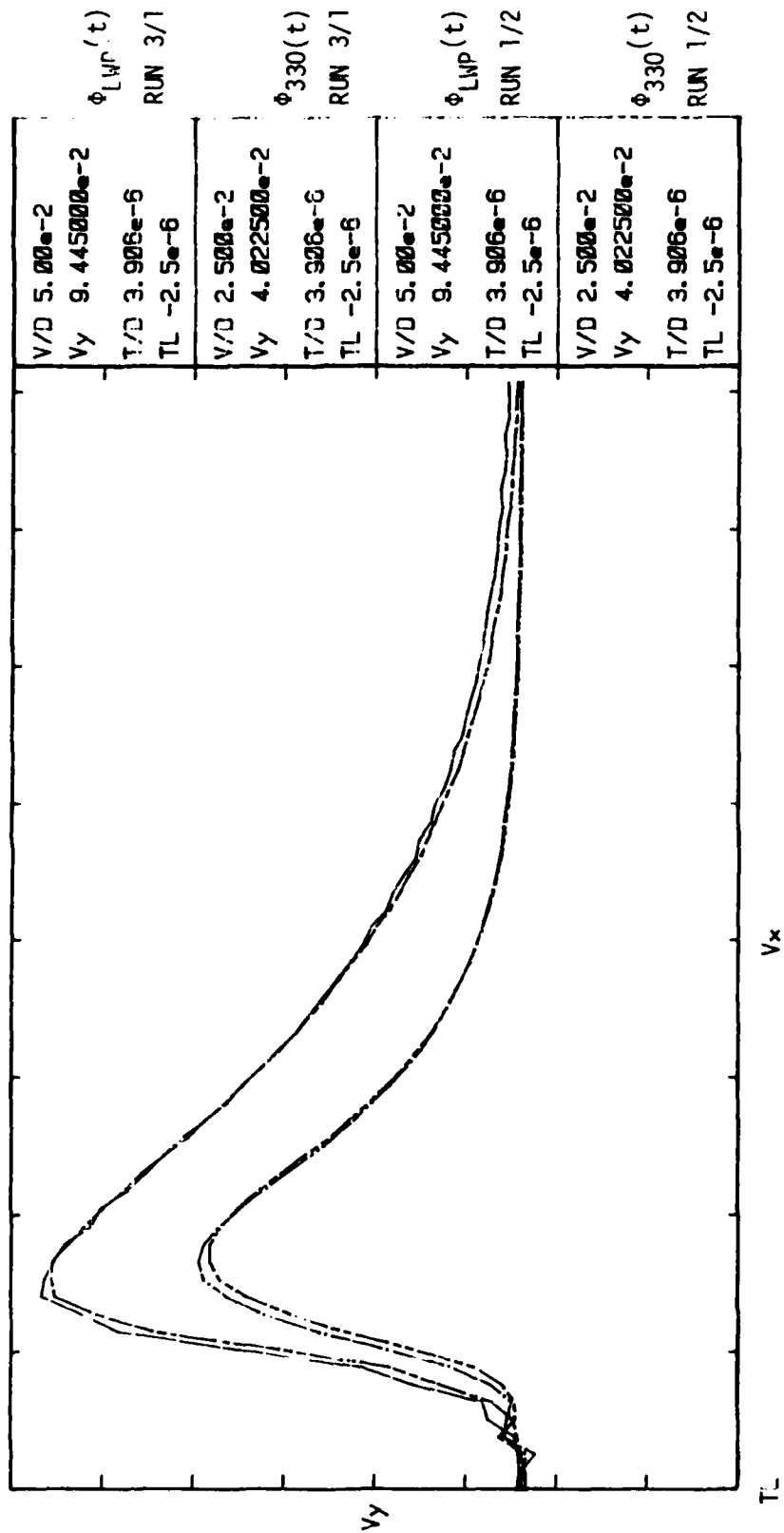


Figure 28. Reproducibility of optical flux signals with no absorber.

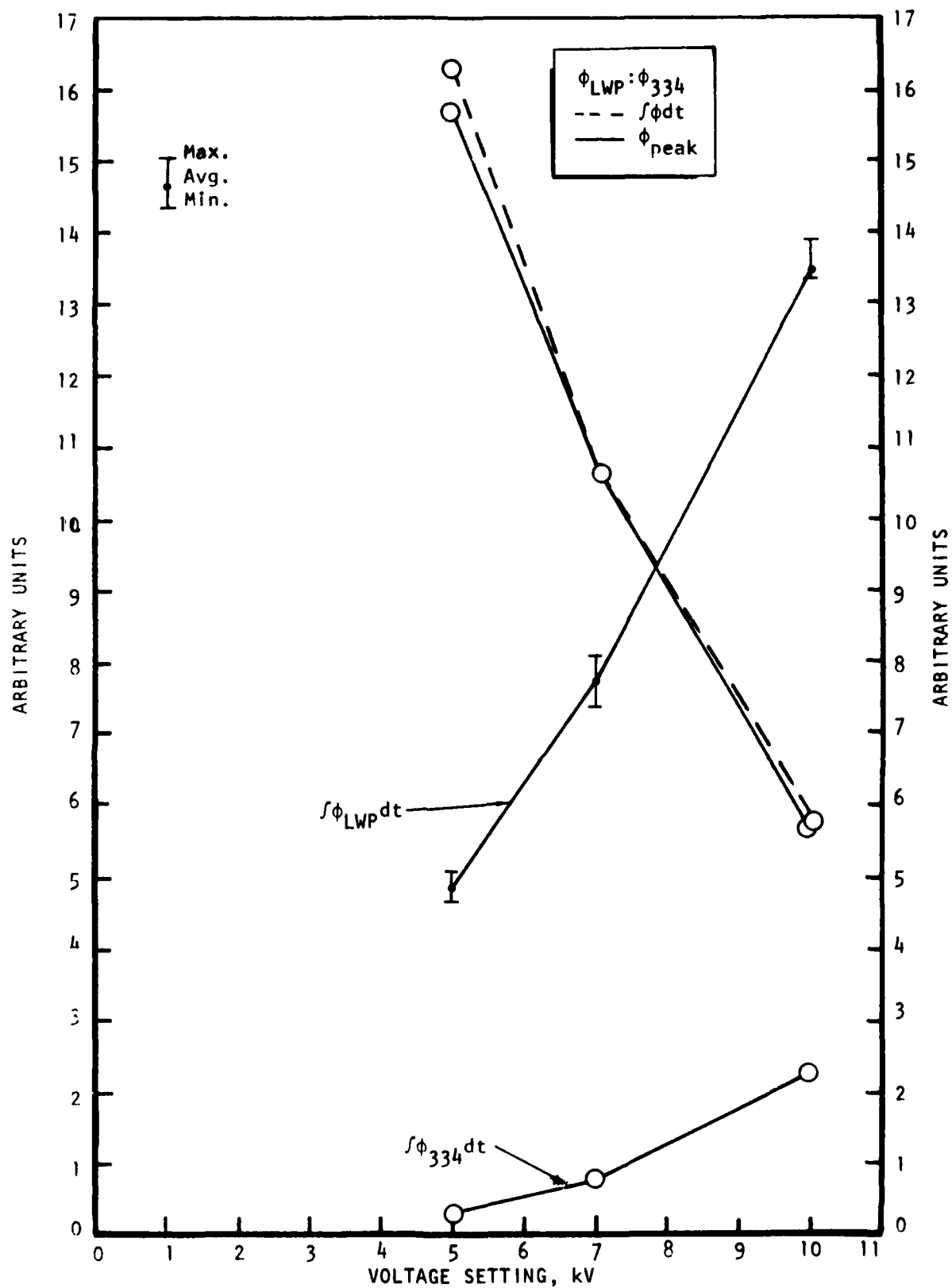


Figure 29. Lamp optical characteristics.

DATE: 8/13/85  
 RUN: 1/1  
 FILL: 12 psia He  
 VOLTAGE SETTING: 26 kV

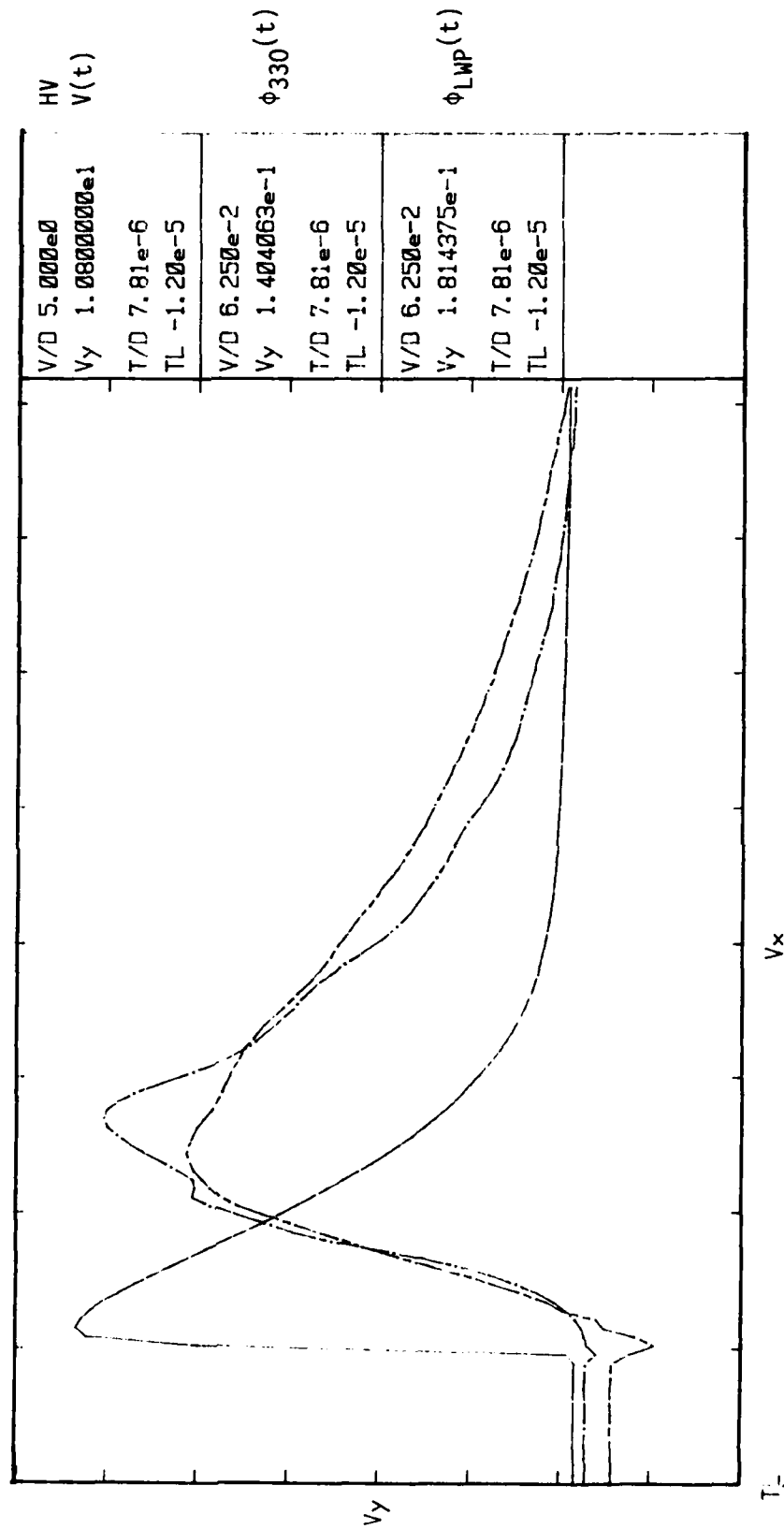


Figure 30. Optical and electrical characteristics of the large flashlamp.



Table 4. FLASHLAMP SPECTRAL COMPARISON

Lamp, Voltage	$\Phi_{330}/\Phi_{LWP}^{(a)}$
Small, 5 kV	0.064
Small, 7 kV	0.044
Small, 10 kV	0.18
Large, 25 kV	1.13

(a) This is a ratio of detector signals under the same conditions of attenuation and filtering, not a ratio of optical fluxes.

Behavior of the lamp over time had a variation as shown in Figure 31, where the observed signal  $\Phi_{LWP}$  is plotted against the number of shots. The raw observed peak signal is plotted as well as the observed peak adjusted by variation in the discharge energy. The adjusted values appear more sensitive to the voltage-dependent adjustment parameter than the raw data are to the actual voltage. This suggests the possibility of some sort of current saturation which results in the peak light output being relatively independent of voltage at settings near 25kV. There appeared to be a slight degradation in light output during each test day and a possible degradation over the duration of the data. This latter degradation could have been associated with variations in the fiber bundle positioning from day-to-day.

Variation in the UV light output, as indicated by  $\Phi_{330}$ , was larger, at least within a given test day. This may be seen in Figure 32, which is a plot of the ratio of the  $\Phi_{330}$  to  $\Phi_{LWP}$  signals obtained with only helium in the reactor. In the case of the 8/14 data, the first shot produced a low  $\Phi_{330}$  signal which was restored after window cleanup and alignment check. Degradation of the UV signal during this day is tentatively assigned to window contamination associated with exposure of the system to  $Cl_2$ . The lines drawn on Figure 31 were used to determine the factor by which the measured  $\Phi_{LWP}$  should be multiplied to determine the appropriate  $\Phi_{330} I_o$  for each shot which was made with  $Cl_2$  in the reactor.

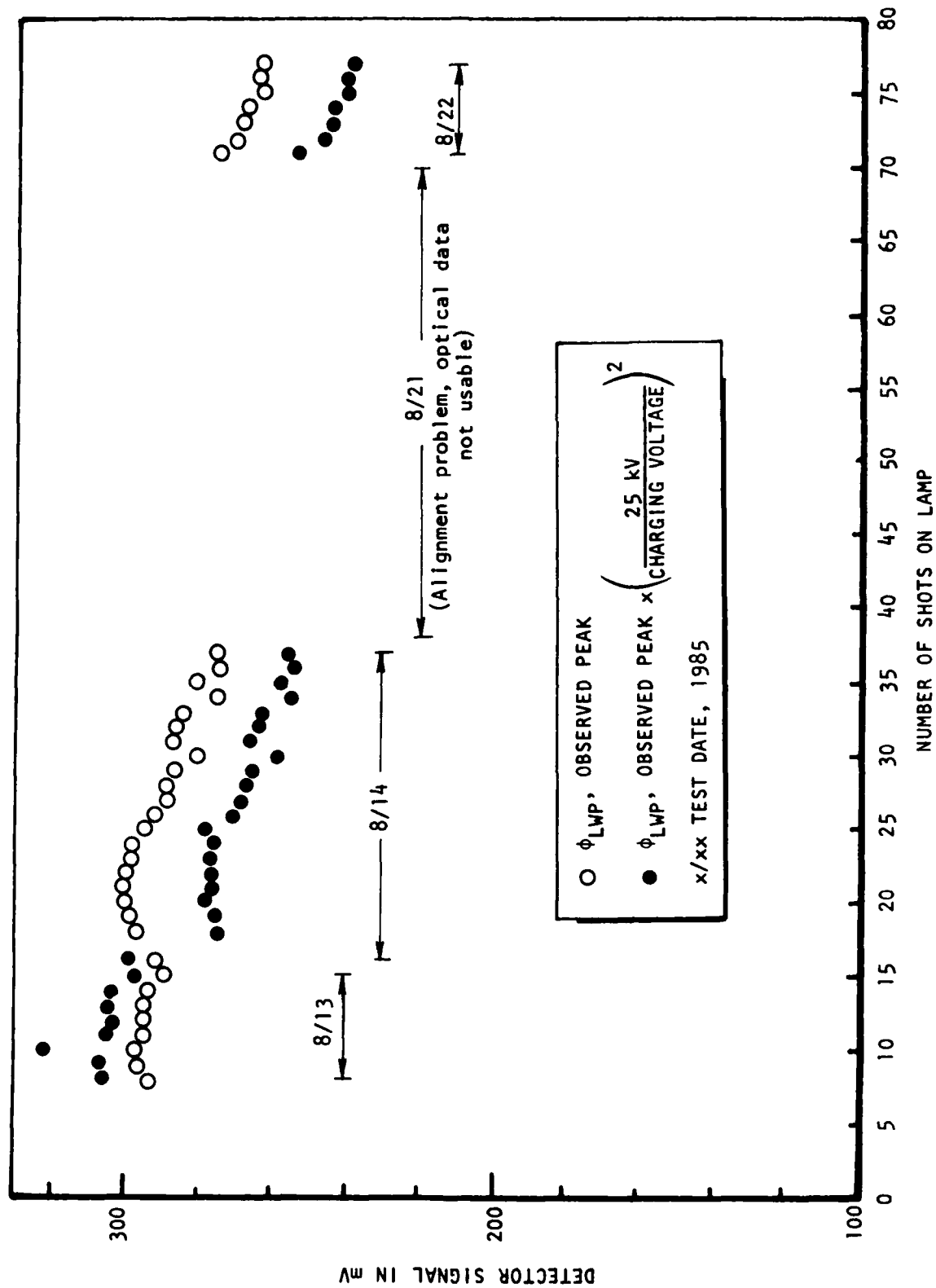


Figure 31. Summary of flashlamp intensity beyond 550 nm.

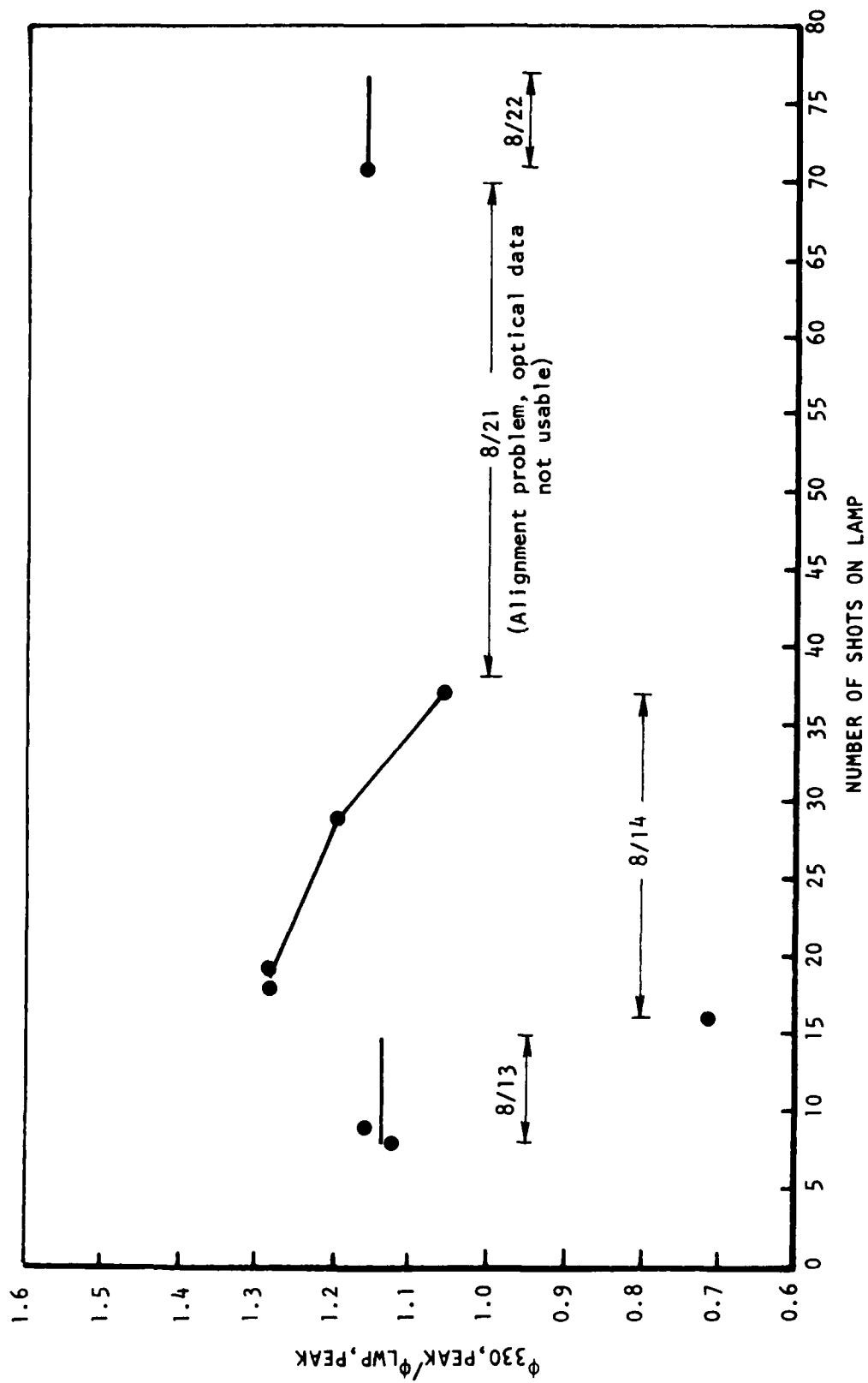


Figure 32. Summary of flashlamp intensity near 334 nm compared with intensity beyond 550 nm.

## FLASHLAMP ENERGY ABSORPTION BY $\text{Cl}_2$

When the gas fill in the reactor contains  $\text{Cl}_2$ , part of the flashlamp energy is absorbed and some of the  $\text{Cl}_2$  is dissociated. As the thermalization described earlier proceeds, the pressure in the constant volume reactor rises. In this section, the observations characterizing the absorption and the pressure rise are presented and discussed. The results are presented separately for the small and large flashlamp experiments because of the differences in geometry and other experimental conditions. In both setups, the absorption was observed via the  $\Phi_{330}$  optical signal and the pressure rise was observed using the quartz transducer.

### Ultraviolet Absorption, Small Flashlamp System

As  $\text{Cl}_2$  is added to the cell, the in-band flashlamp intensity reaching the detector decreases, as shown in Figure 33. When the cylindrical geometry of the internally mounted flashlamp is analyzed according to Beer's law, it is found that the ratio of the observed intensity with and without  $\text{Cl}_2$  present should be given by the familiar exponential:

$$\frac{I(r)}{I_0(r)} = 10^{-\epsilon \rho l}$$

where

- |            |   |
|------------|---|
| $I(r)$     | is the observed intensity at $r$ with an absorber present                                 |
| $I_0(r)$   | is the observed intensity at $r$ with no absorber present,                                |
| $r$        | is the radial position of the measurement,  |
| $\epsilon$ | is the extinction coefficient in $1/\text{mol} \cdot \text{cm}$ ,                         |
| $\rho$     | is the $\text{Cl}_2$ concentration in $\text{mol/l}$ , and                                |
| $l$        | is the radial distance from the lamp surface to the measurement position in $\text{cm}$ . |

When the data shown in Figure 33 are compared with the predictions of Beer's law, the results are as shown in Figure 34. When the actual dimensions are used in Beer's law, the agreement is only good to about 20-30% on  $\text{Cl}_2$  pressure. If the absorption data are used to derive an average "effective" path length, the agreement is quite good when this effective path length is then used in Beer's law. This result, with the effective path length being smaller than the actual path length, is consistent with light reaching the detector indirectly, after having been reflected or scattered from the cell walls. Thus,

DATE: 3/8/85  
 RUN: AS NOTED  
 FILL: 4 psia SF<sub>6</sub> + Cl<sub>2</sub> AS NOTED  
 VOLTAGE SETTING: 10 kV

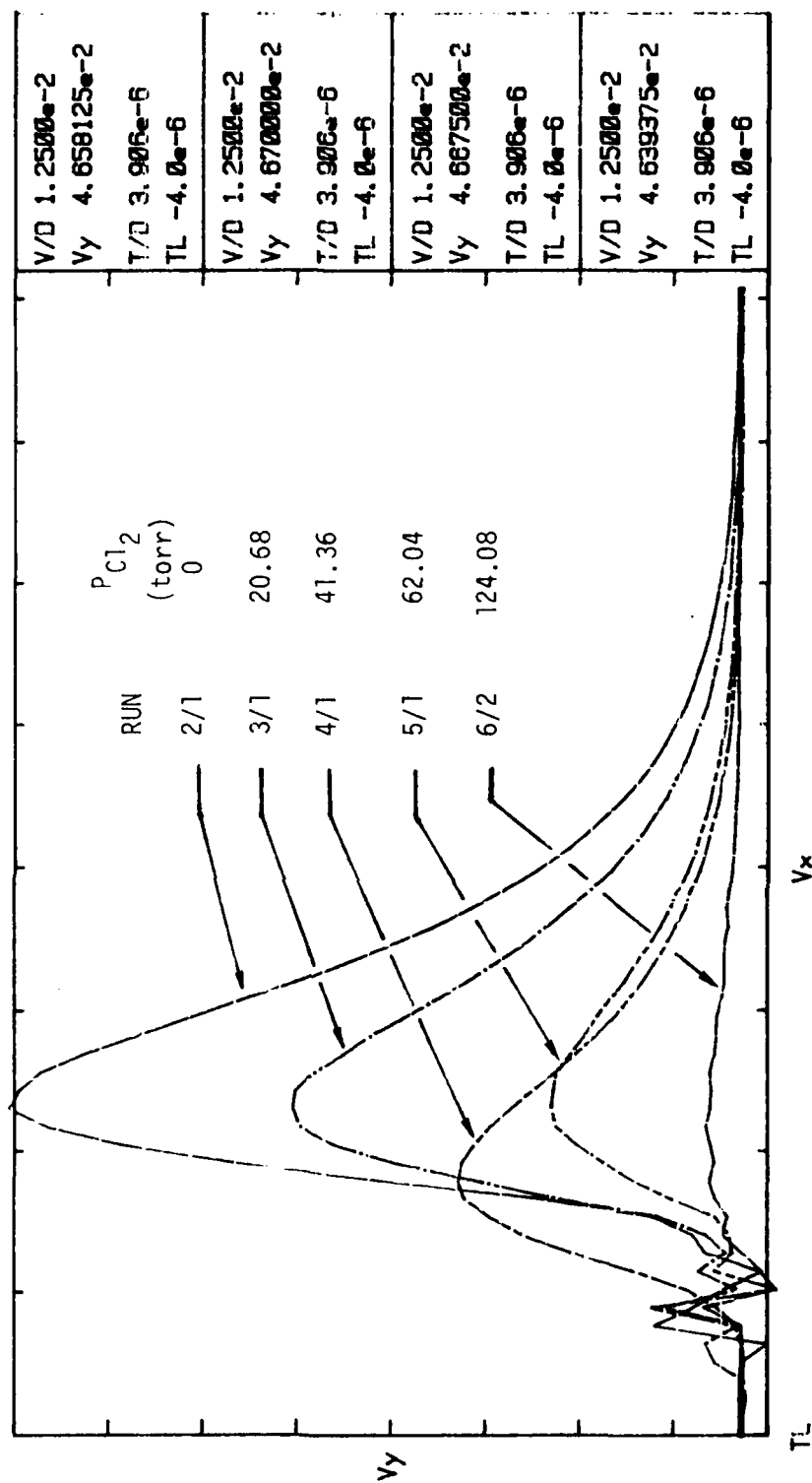


Figure 33.  $\phi_{330}(t)$  for various Cl<sub>2</sub> partial pressures.

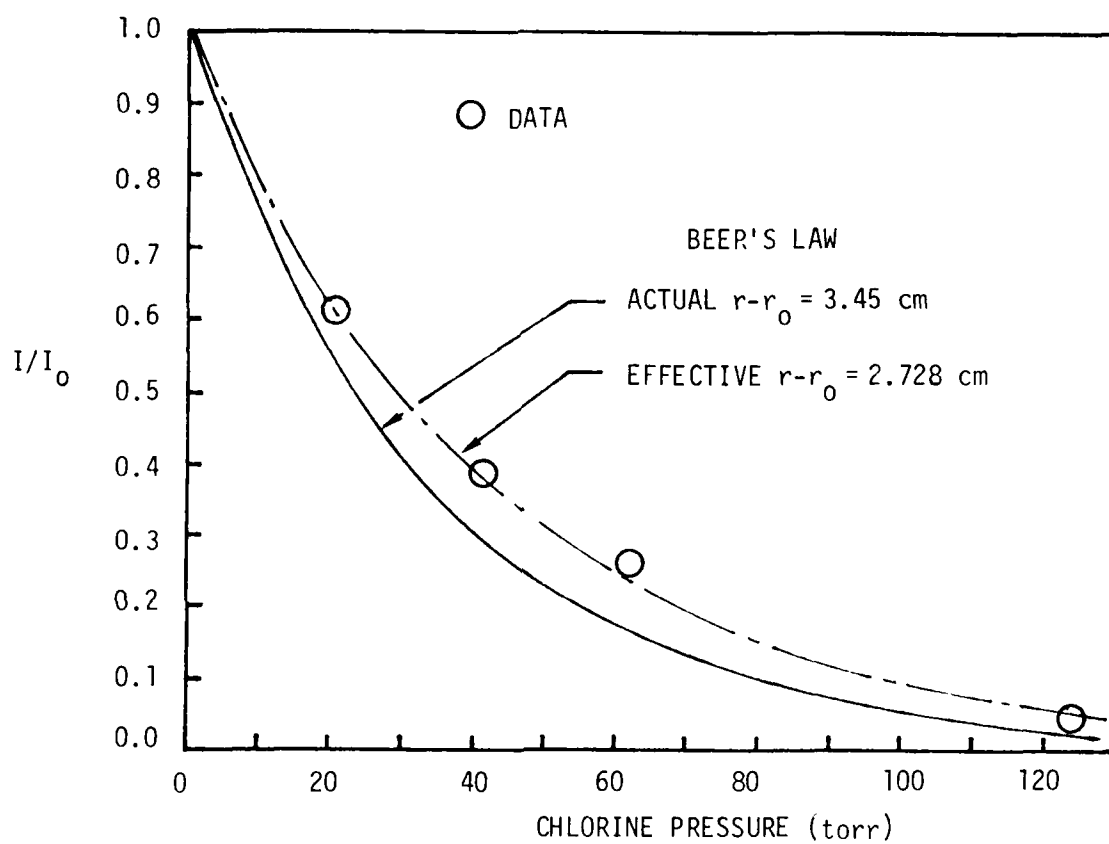


Figure 34. Absorption by  $\text{Cl}_2$  at 334 nm.

Beer's law using the effective path length can be used to determine the chlorine remaining in the cell after a run.

#### Ultraviolet Absorption, Large Flashlamp System

For this setup, absorption at 334nm inside the cylindrical reactor mounted adjacent to the flashlamp would be expected to follow Beer's law if the incoming wavefront were collimated and uniform. Since a collimating lens was not used, strict adherence to Beer's law was not expected.

Data from the tests made with this system are plotted in Figure 35. Discrepancies between observations and Beer's law approach a factor of two for the 5 and 10 torr experiment 3: i.e., if observed  $I/I_0$  and Beer's law is used to infer a  $Cl_2$  pressure, it will be close to double the  $Cl_2$  pressure added to the reactor according to the P3 pressure gauge. The origin of this discrepancy has not been identified and it is probably a combination of factors, including gauge reading uncertainty and optical system geometry effects.

#### Pressure Rise in Small Flashlamp System

All tests conducted with this system included  $SF_6$  in the reactor to prevent arcing. Figure 36 shows a typical signal from the quartz transducer on two time scales. The unexpanded pressure trace before and after the event is seen to carry a small oscillation with a period of about 17 ms. This apparently originated in the transducer/power unit system and was considered acceptable. After the firing, the pressure is seen to rise sharply and then decay back to zero in about 300 ms. The decay is a compound phenomenon associated with actual pressure decay and the transducer characteristic decay time. Sharp oscillations with a period of about 5 ms are observed during the decay. When the time scale is expanded 64X, as in the second trace of Figure 36, oscillations with a period of about 1 ms are observed. When the time scale is expanded by 400X, as in the second trace of Figure 37, oscillations with a period of about 330  $\mu s$  are observed. All of these oscillations are believed to be caused by acoustic phenomena associated with characteristic dimensions of the experimental apparatus.

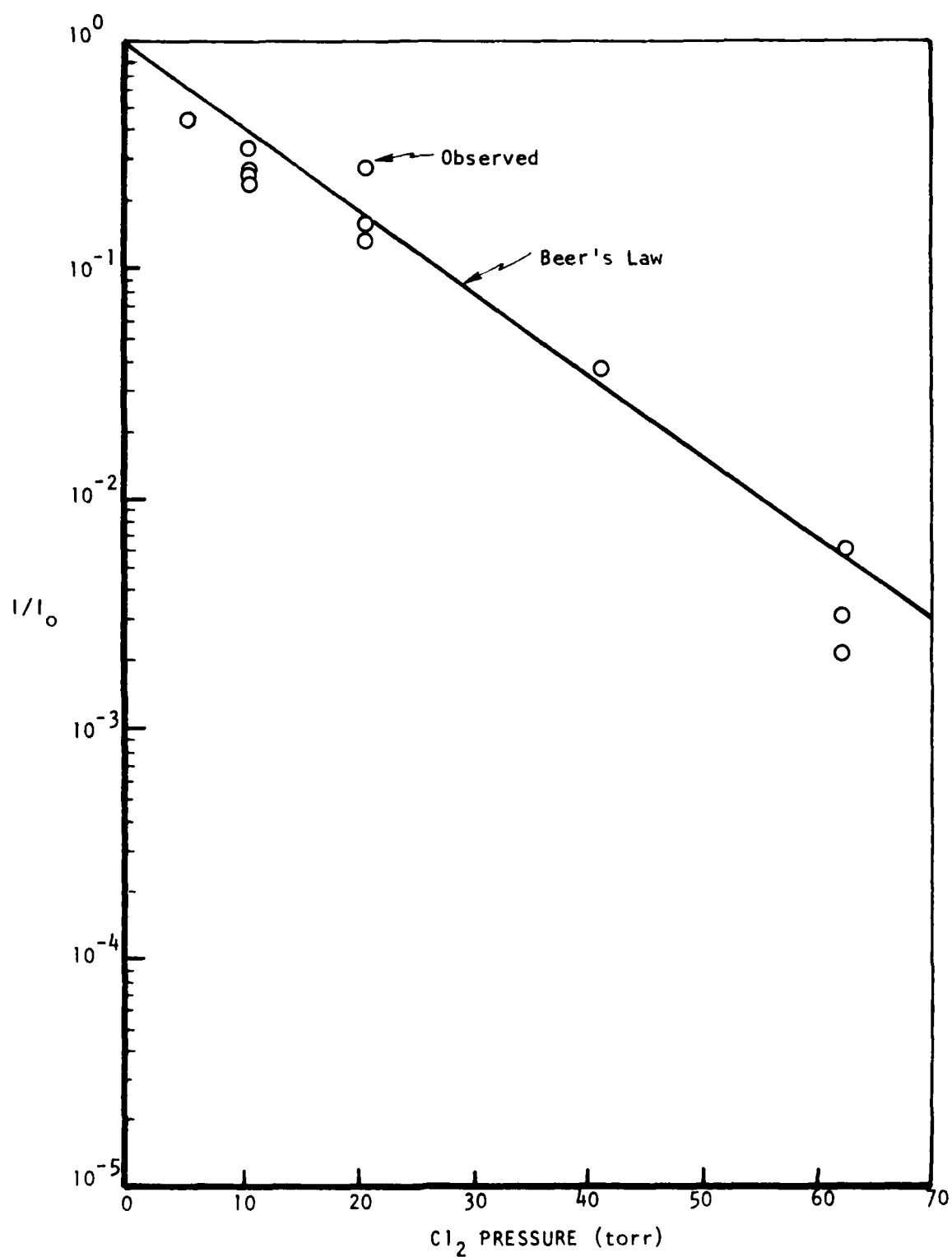


Figure 35. Transmitted intensity vs.  $\text{Cl}_2$  pressure for the large flashlamp and 10 cm reactor.



DATE: 3/8/85

RUN: 13/1

FILL: 4 psia SF<sub>6</sub>, 1.2 psia Cl<sub>2</sub>, 1.2 psia H<sub>2</sub>

VOLTAGE SETTING: 10 kV

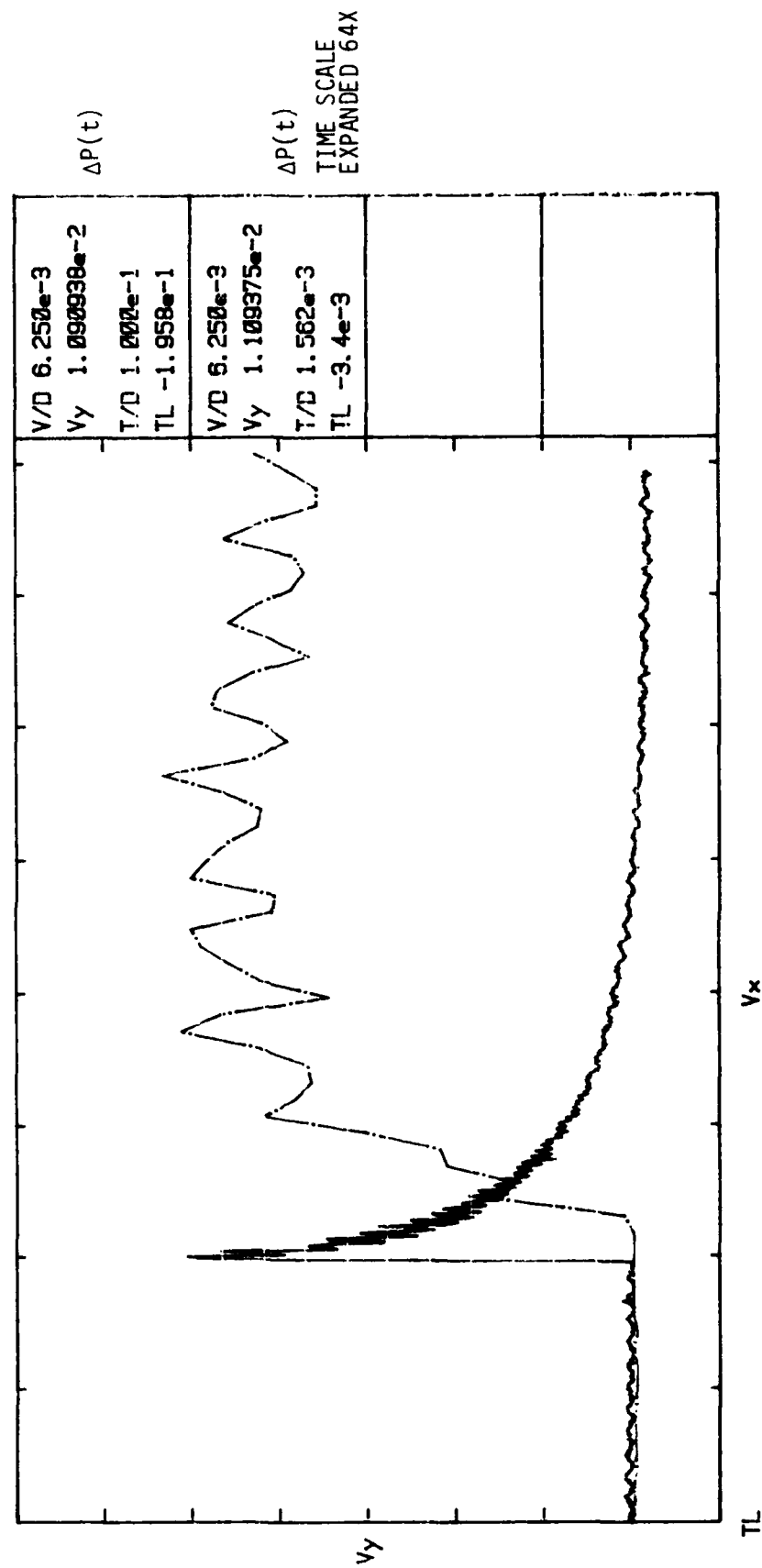


Figure 36. Pressure trace with a 10 kV discharge in H<sub>2</sub> + Cl<sub>2</sub>.

Figure 37 shows the optical signal,  $\Phi_{LWP}$  for reference, although it is largely obscured by electrical noise on the pressure trace. This noise is damped out by about 60  $\mu$ s. Since the noise has been damped out before the first pressure wave begins to arrive at the transducer at about 250  $\mu$ s, it was considered acceptable.

A series of tests was conducted in which a fixed amount of  $SF_6$  and a variable amount of  $Cl_2$  was added to the reactor. After the flashlamp discharge, the pressure in the cell was observed to rise rapidly and then decay. The observed peak pressure values are shown in Table 5. The peak pressures were taken as the peaks of the oscillations shown in Figure 36 and 37.

The results from a series of tests with fixed  $SF_6$  and  $Cl_2$  and variable  $H_2$  are shown in Table 6. Results include the observed peak pressure rise and the degree of  $Cl_2$  reaction, which was determined by firing the lamp a second time after a period of a minute or less. The observed  $\Phi_{330}$  peak signal was then used, together with the empirical fit shown earlier in Figure 33, to estimate the amount of  $Cl_2$  remaining. As seen in Table 5, the  $Cl_2$  reacted was rather low, varying from near 10% to near 50% for the conditions shown. This is discussed further in the analysis section of the report.

#### Pressure Rise in Large Flashlamp System

Pressure rise signals obtained using the large flashlamp system were accompanied by stronger acoustic phenomena than had been observed with the 100J system. This was because of the higher energy deposition density, smaller reactor volume and location of the transducer with its diaphragm nearly flush with the reactor wall. Thermal effects were also observed but were moderated by covering the transducer diaphragm with a piece of adhesive-backed TFE tape. Figure 38 shows the pressure trace obtained after correction for a shifting baseline, with 620 torr of  $Cl_2$  in the reactor. The pressure rises rapidly, then appears to follow a damped oscillation having a period of about 900  $\mu$ s. The Fourier transform of this pressure, shown in Figure 39, contains not only a fundamental peak near 1100 Hz, but also several weak overtones. The phenomena leading to the observed pressure rise waveform is believed to be initially a travelling wave initiated when the ultraviolet light is deposited

DATE: 3/8/85

RUN: 13/1

FILL: 4 psia SF<sub>6</sub>, 1.2 psia Cl<sub>2</sub>, 1.2 psia H<sub>2</sub>

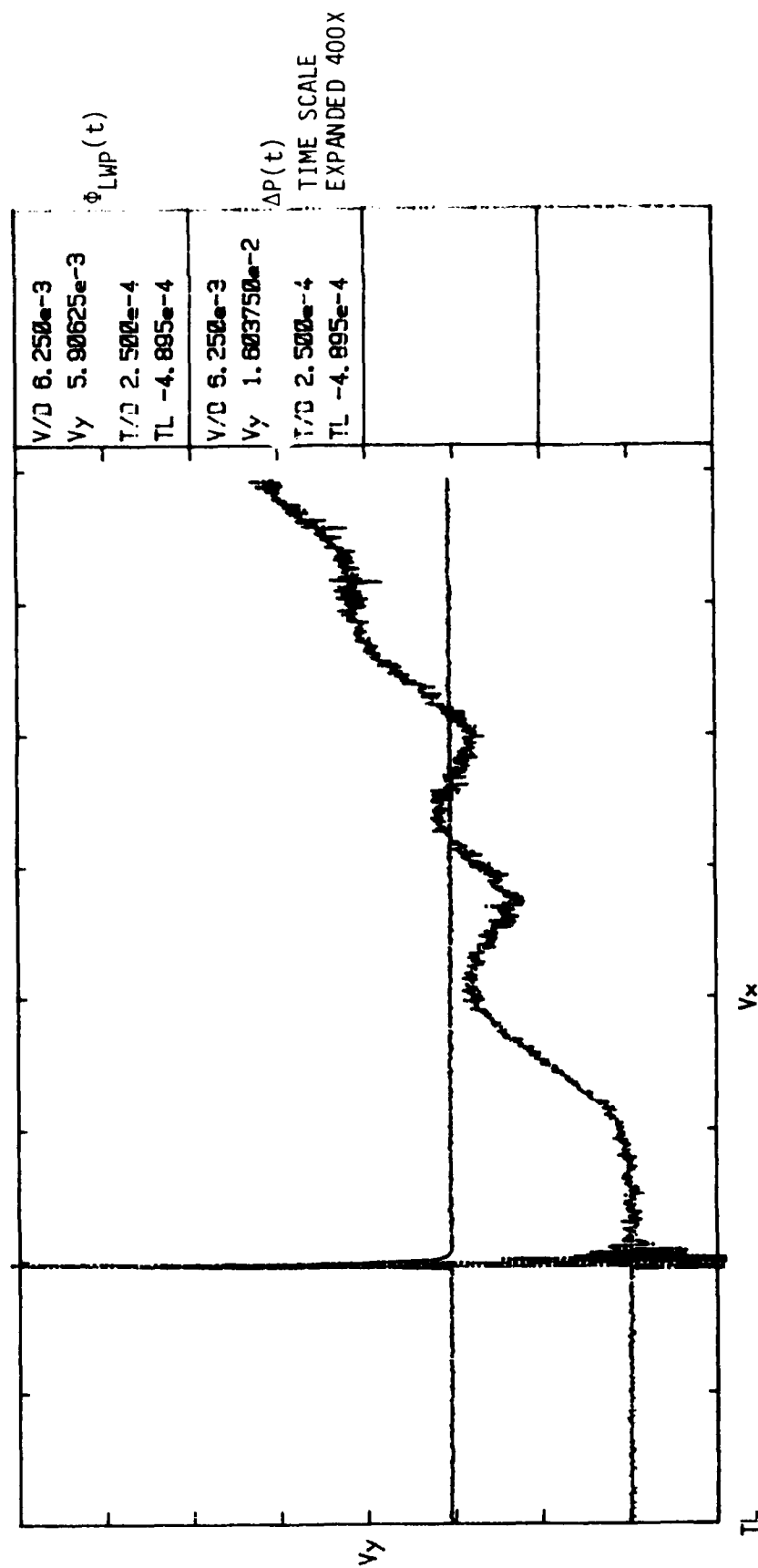


Figure 37. Pressure behavior with a 10 kV discharge in H<sub>2</sub> + Cl<sub>2</sub>.

TABLE 5. PRESSURE RISE WITH  $SF_6 + C^{12}_2$   
(100J DISCHARGE)

RUN IDENTIFICATION	PRESSURES (torr)		
	$SF_6$ FILL	$C^{12}_2$ FILL	OBSERVED $\Delta P$
3/8/85: 3/2	207	21	1.79
3/8/85: 4/1	207	41	3.72
3/8/85: 5/1	207	62	5.62
3/8/85: 6/2	212	124	10.74
3/8/85: 7/3	207	248	16.45
3/8/85: 8/1	207	414	23.94

TABLE 6. PRESSURE RISE AND  $\text{Cl}_2$  REACTED WITH  $\text{SF}_6 + \text{Cl}_2 + \text{H}_2$   
(100J DISCHARGE)

RUN IDENTIFICATION	PRESSURES (torr)				$\Delta\text{Cl}_2/\text{Cl}_2$
	$\text{SF}_6$ FILL	$\text{Cl}_2$ FILL	$\text{H}_2$ FILL	$\Delta P$ OBS	
3/11/85: 5/1	207	62	62	57	0.093
3/11/85: 5/2	207	62	62	75	NO DATA
3/11/85: 6/1	207	62	124	175	0.375
3/11/85: 7/1	207	62	248	318	0.549
3/11/85: 8/1	207	62	496	519	0.524

DATE: 8/21/85  
 RUN: 2/1  
 FILL: 12 psia  $Cl_2$   
 VOLTAGE SETTING: 26 kV

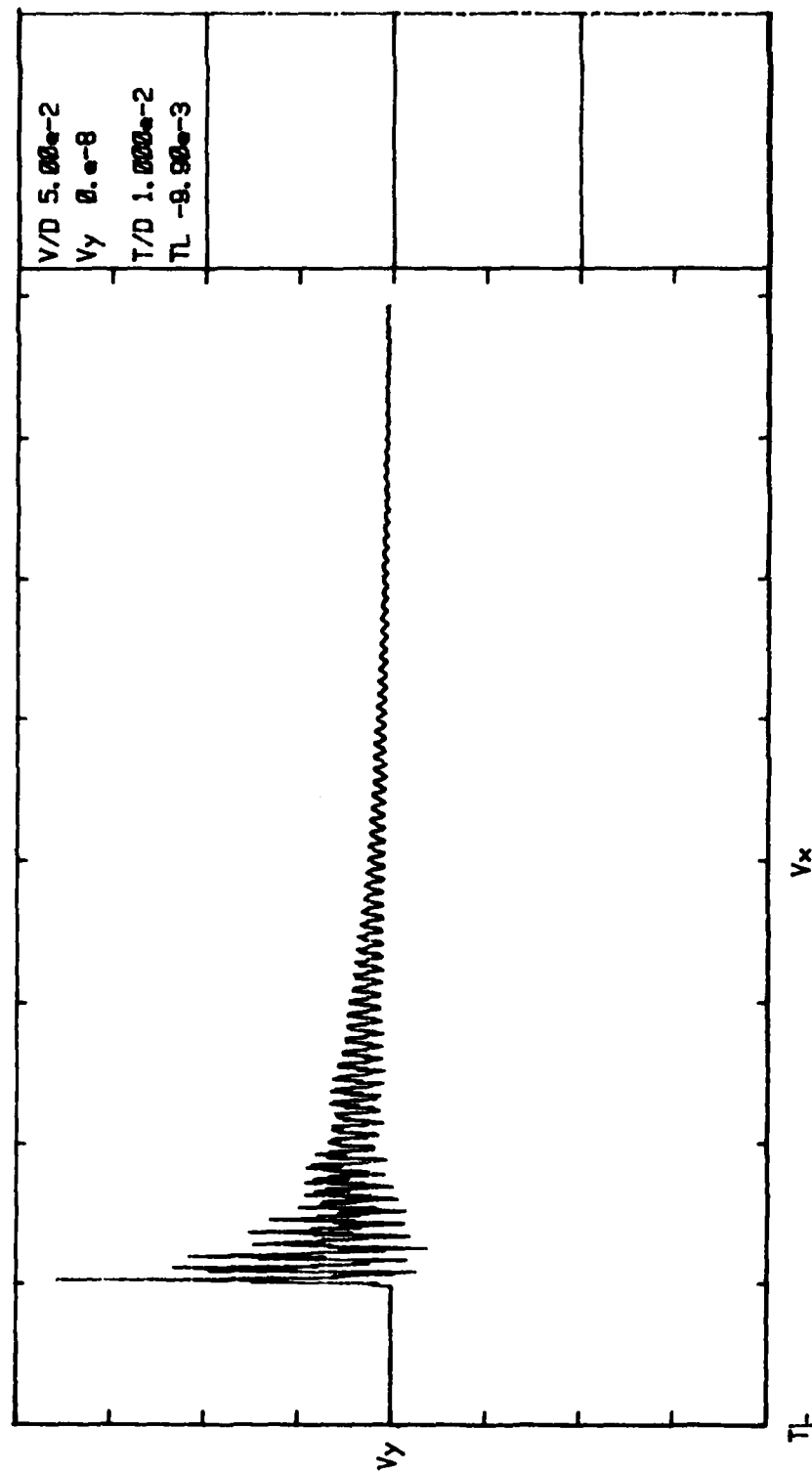


Figure 38. Pressure trace observed in  $Cl_2$ .

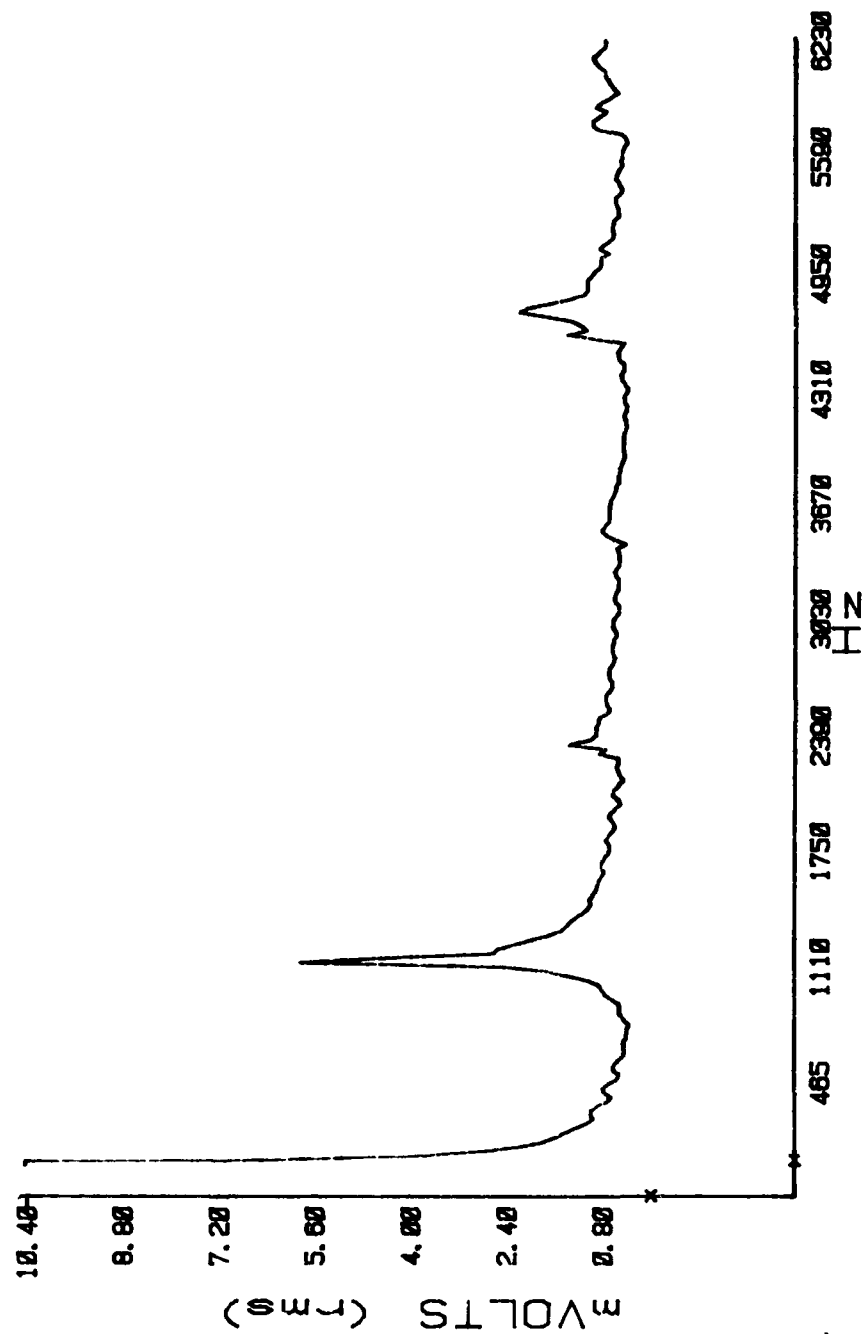


Figure 39. Fourier transform of the pressure trace shown in Figure 38.

into a thin slab of  $\text{Cl}_2$  near the window. This probably degrades into more of a standing wave later.

Table 7 displays the results of some acoustic calculations and shows that the observed 1100 Hz is in good agreement with expected acoustic transit times for a travelling wave at 300 K. Closer examination of the waveform on an expanded time scale (Figure 40) shows some fine structure in the acoustic pulses. The first few oscillations are clearly separated into two peaks. The time interval between peaks 1 and 3 of  $7.8 \times 10^{-4}$  s should correspond to one round trip of a distance  $2L$  or 0.2 m. This leads to a velocity of sound of 256 m/s. Ignoring  $\gamma$  variations, a temperature of 430 K can be derived from this. The time between peaks 1 and 2 is 140  $\mu\text{s}$ . The ratio of this time to  $7.8 \times 10^{-4}$  s is 0.179, in good agreement with the ratio of the distance between the transducer and the near window to the total reactor length, 0.190 (ref. Fig. 11). This supports the idea of a traveling wave bouncing between the two windows. The time of arrival of the first peak after the light pulse supports a speed of sound near 280 m/s.

A number of approaches was tried to estimate an effective pressure and temperature for comparison with steady state analytical results. Figure 41 shows the observed  $\Delta P$  vs.  $\text{Cl}_2$  pressure for the  $\Delta P$  of the highest peak and for the average  $\Delta P$  taken between the peaks of the first and second cycles (e.g. average  $\Delta P$  between peaks 1 and 3 of Figure 40). This latter  $\Delta P$  is believed to represent an effective or volumetrically average  $\Delta P$  shortly after the light pulse. Figure 41 also shows the temperature as derived from the speed of sound based on the time between the first and second peaks (e.g. peaks 1 and 3 in Figure 40)  $\Delta t = 1/f = 2L/R$ . Variations in  $\gamma$  were ignored in deriving the temperature from  $c$ .

When  $\text{H}_2$  and  $\text{Cl}_2$  were introduced together into the reactor and the flash-lamp fired, the pressure rise was generally much higher than that observed with  $\text{Cl}_2$  alone. Figure 42 shows a typical result on two time scales. The fine structure observed with only  $\text{Cl}_2$  in the reactor is not as clear, probably because of detonation or deflagration phenomena occurring in the reactor. The procedures just described were used to derive  $\Delta P$  and  $\Delta T$  from the pressure traces. The results are shown graphically in Figures 43, 44, and 45.



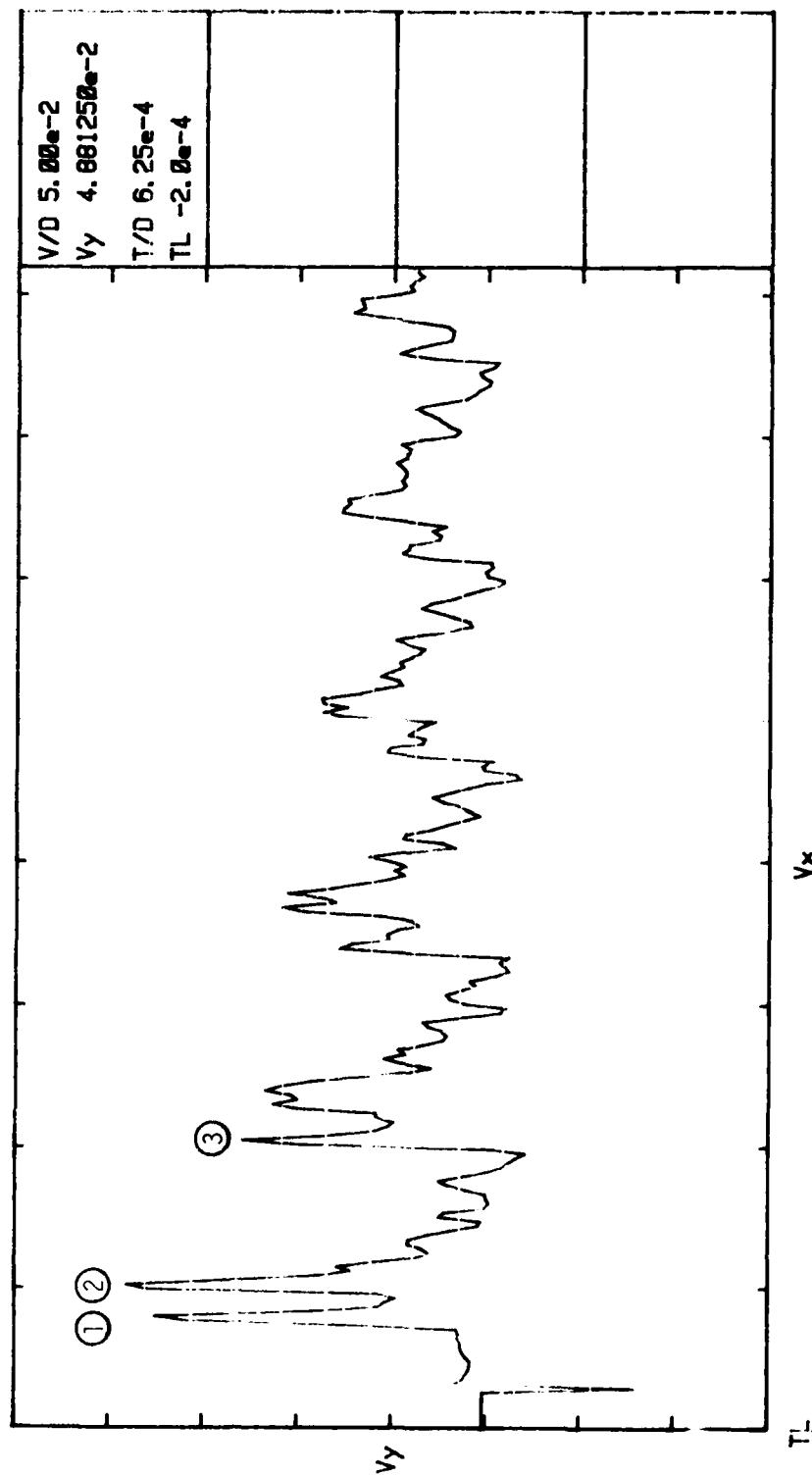


Figure 40. Expanded display of the pressure trace shown in Figure 38.

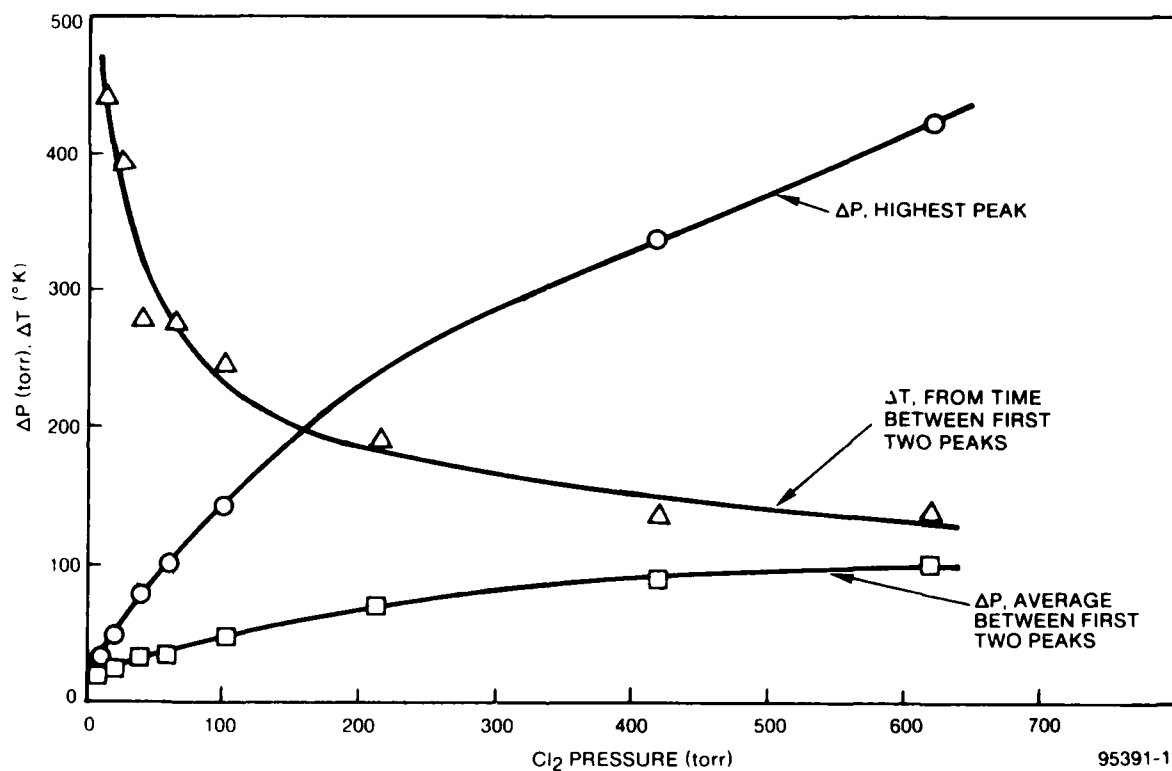


Figure 41. Observed pressure and temperature rise in  $\text{Cl}_2$ .

DATE: 8/21/85  
 RUN: 14/1  
 FILL: 0.2 psia Cl<sub>2</sub> 0.3 psia H<sub>2</sub>  
 VOLTAGE SETTING: 26 kV

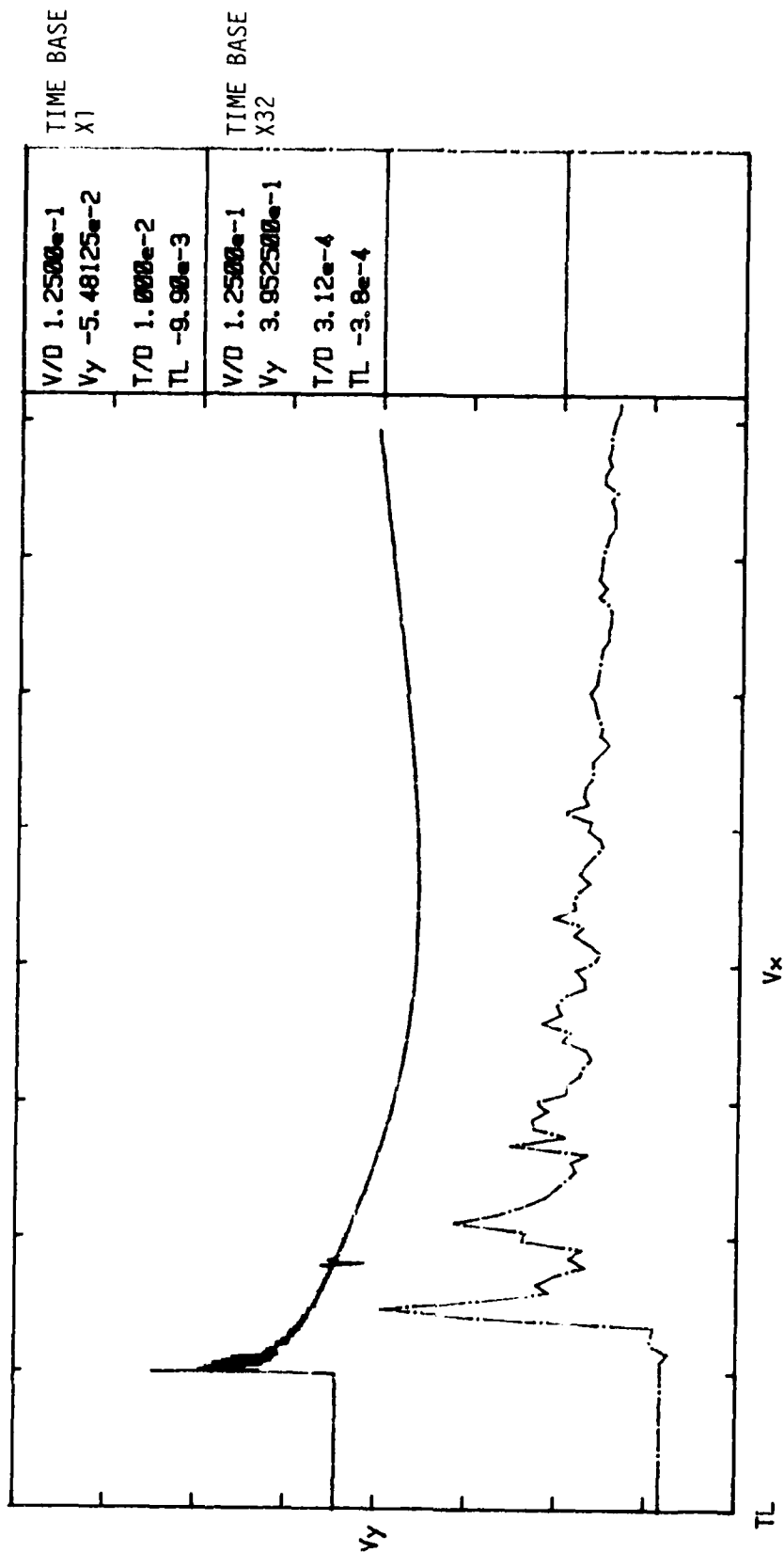


Figure 42. Pressure trace with H<sub>2</sub> and Cl<sub>2</sub> in the reactor.

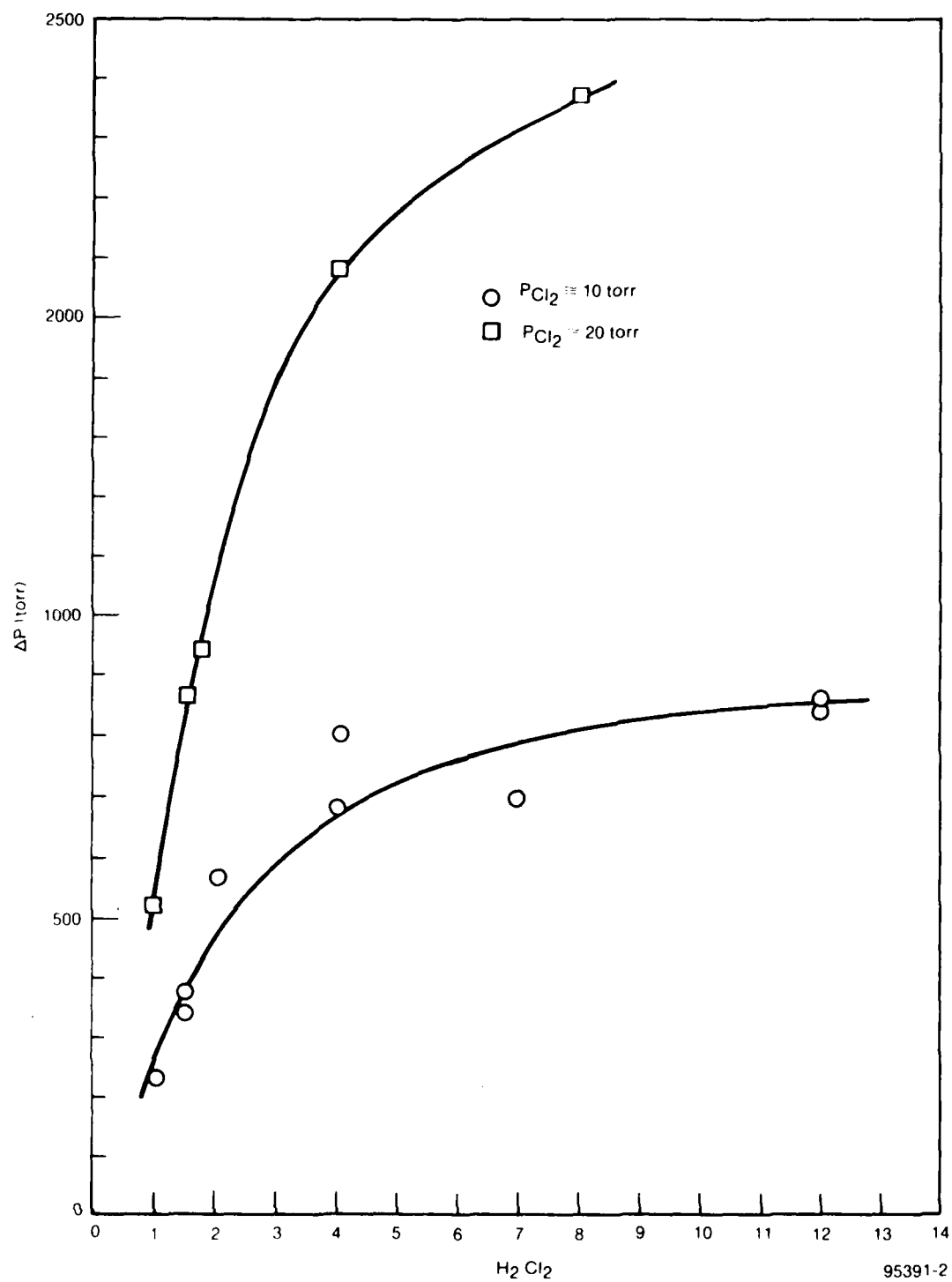


Figure 43. Observed pressure rise in  $Cl_2 + H_2$  based on highest peak.

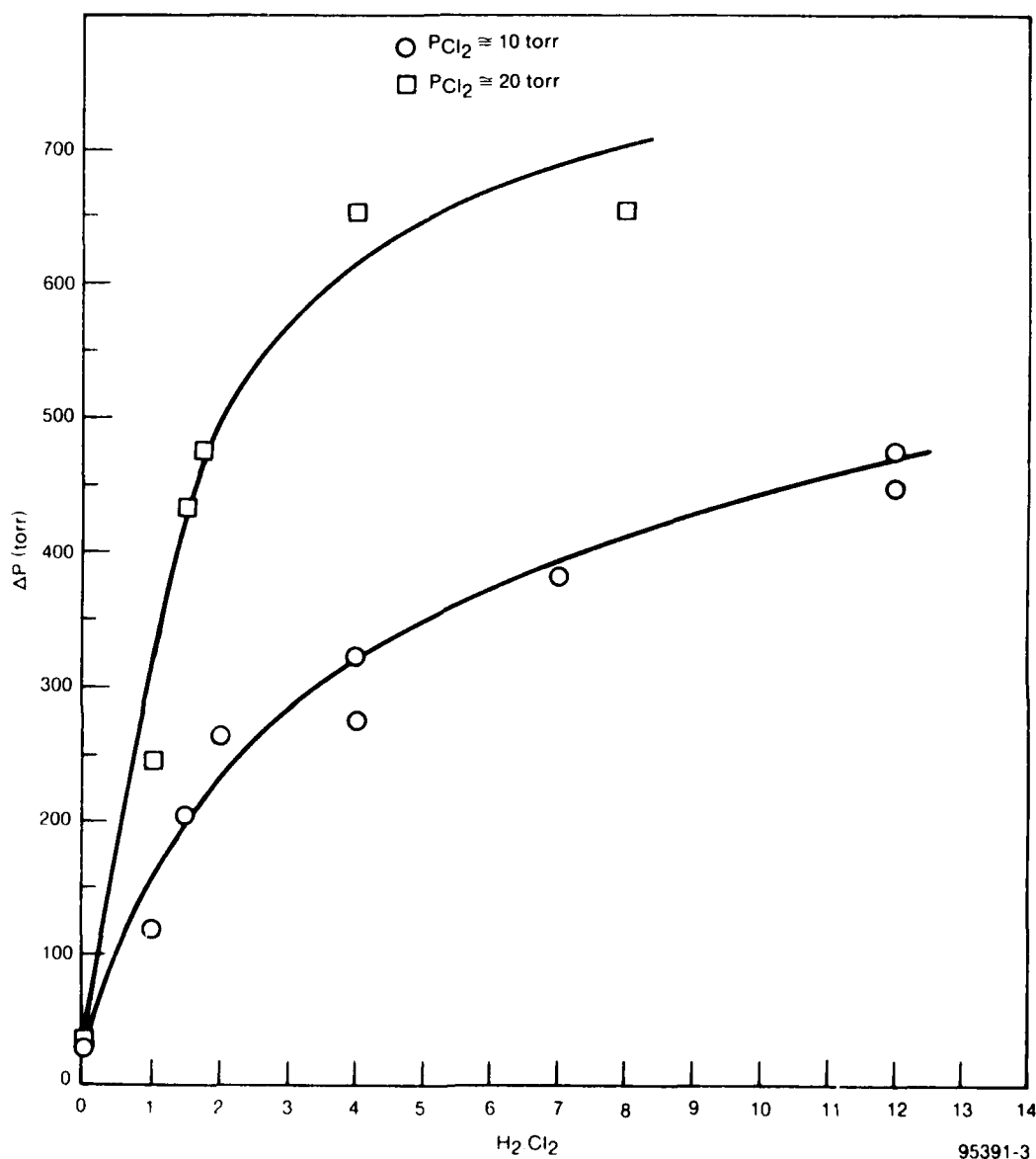


Figure 44. Observed pressure rise in  $Cl_2 + H_2$  based on average of first two peaks.

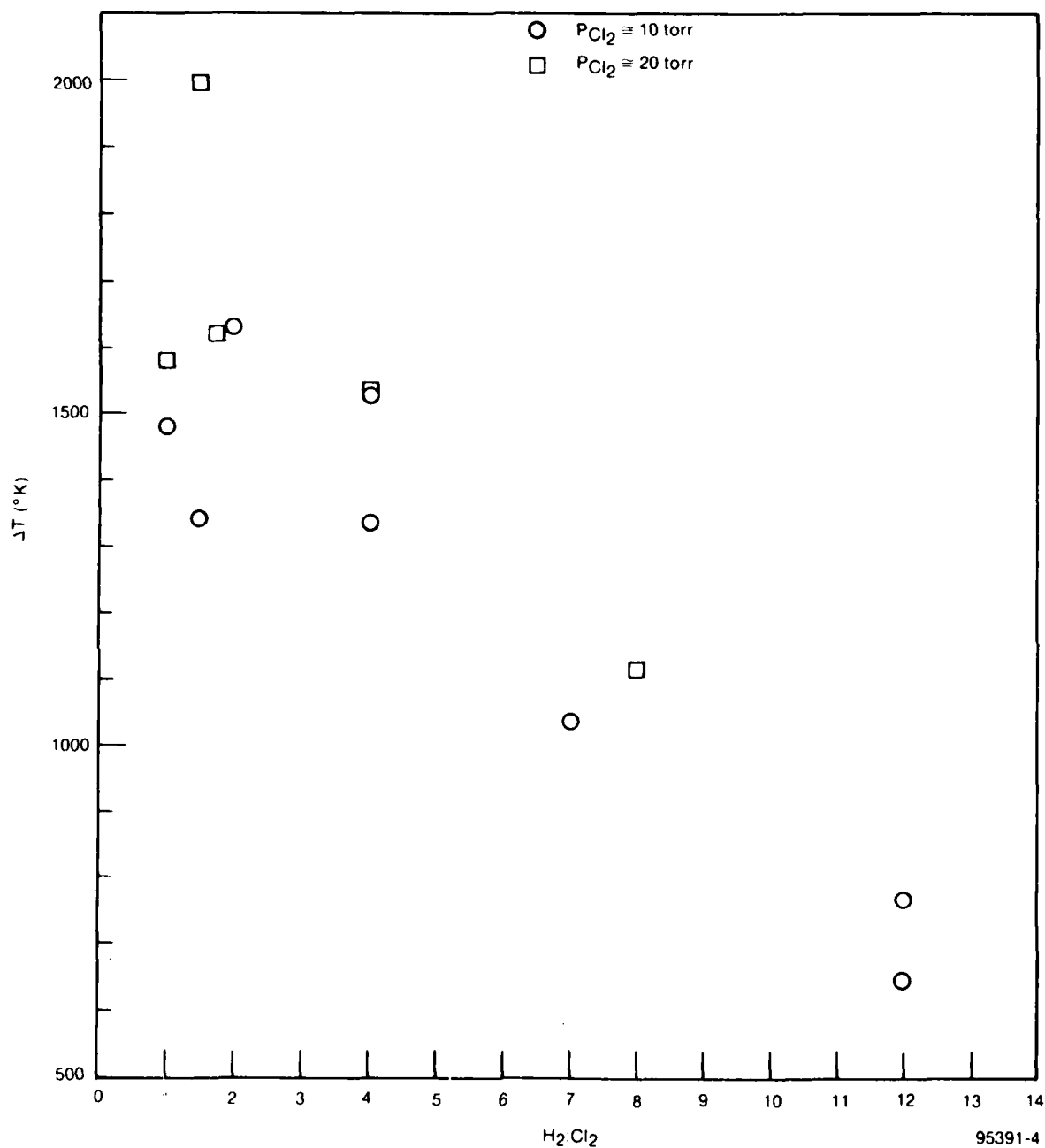


Figure 45. Observed temperature rise in  $Cl_2 + H_2$  based on time between first two peaks.

TABLE 7. Acoustic Frequencies (Calculated)

T (°K)	$\gamma_{\text{Cl}_2}$	$c = (\gamma RT/M)^{1/2}$ (m/s)	(a)	(b)
			$f = \frac{c}{2l}$ Hz	$f = \frac{c}{2(l + 8a/3\pi)}$ Hz
300	1.324	214	1070	954
1000	1.285	385	1925	1716

(a) Expected frequency for a traveling wave

(b) Resonant frequency for a cylindrical column, where,

$c$  = speed of sound

$l$  = length

$a$  = radius

#### FLASHLAMP ENERGY ABSORPTION BY ICl

When ICl was added to the photolysis reactor, results using the large flashlamp system were obtained which were quite similar to those obtained with  $\text{Cl}_2$ . ICl pressures from 4.5 torr to 29 torr were added to the reactor. Optical absorption data are shown in Figure 46. The  $I/I_0$  values were determined as the ratio of the optical signals with helium and with ICl in the reactor. The 500 nm filter (ref. Figure 16) was used. Figure 46 includes the results of Beer's law calculations for wavelengths corresponding to the peak filter transmission ( $\lambda = 505$  nm) and the half power points ( $\lambda = 488$  nm and  $\lambda = 524$  nm).

Pressure rise data were determined as described earlier and are plotted in Figure 47. Corresponding  $\text{Cl}_2$  results are included for comparison.

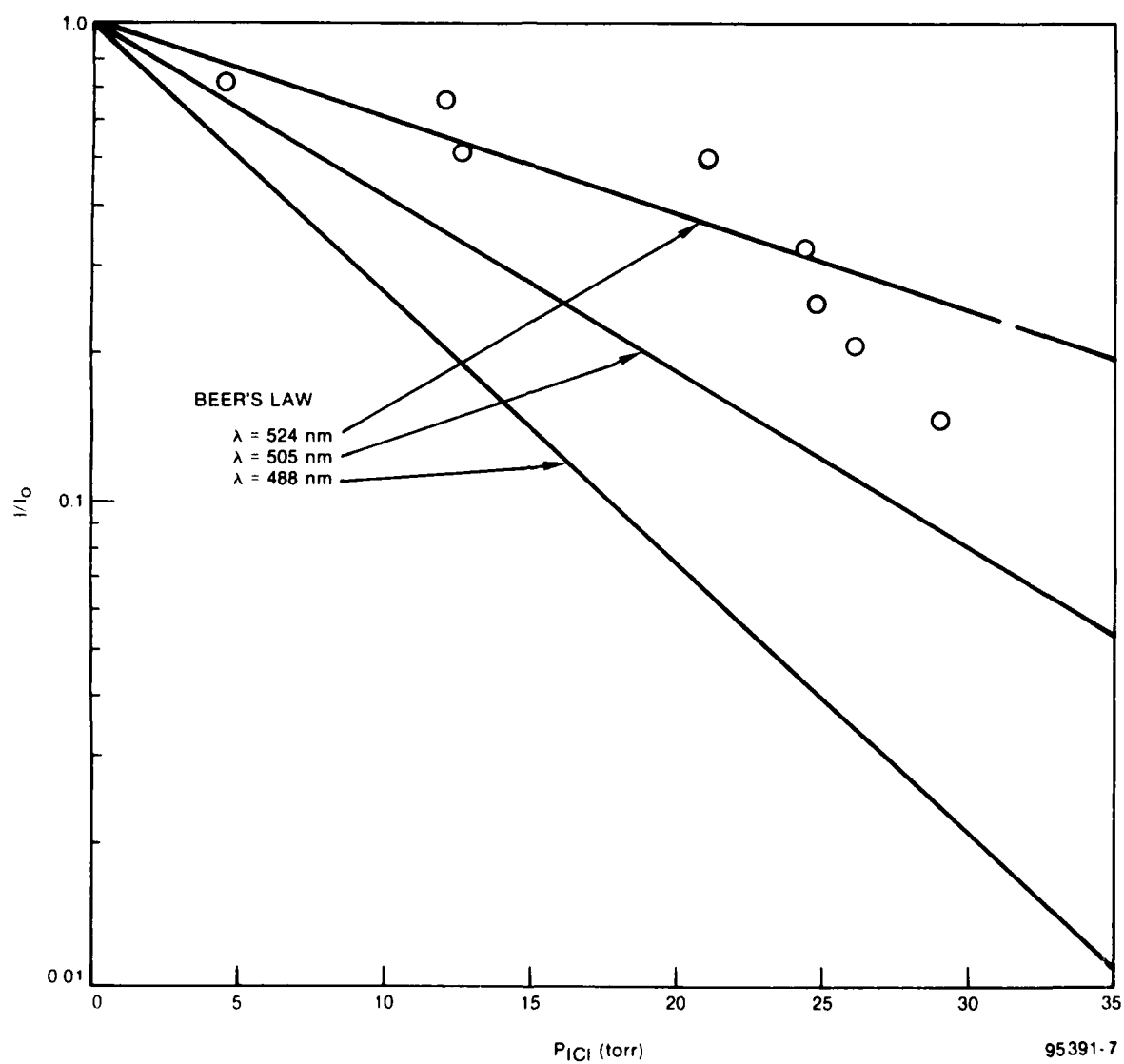


Figure 46. Observed ICl absorption near 500 nm.



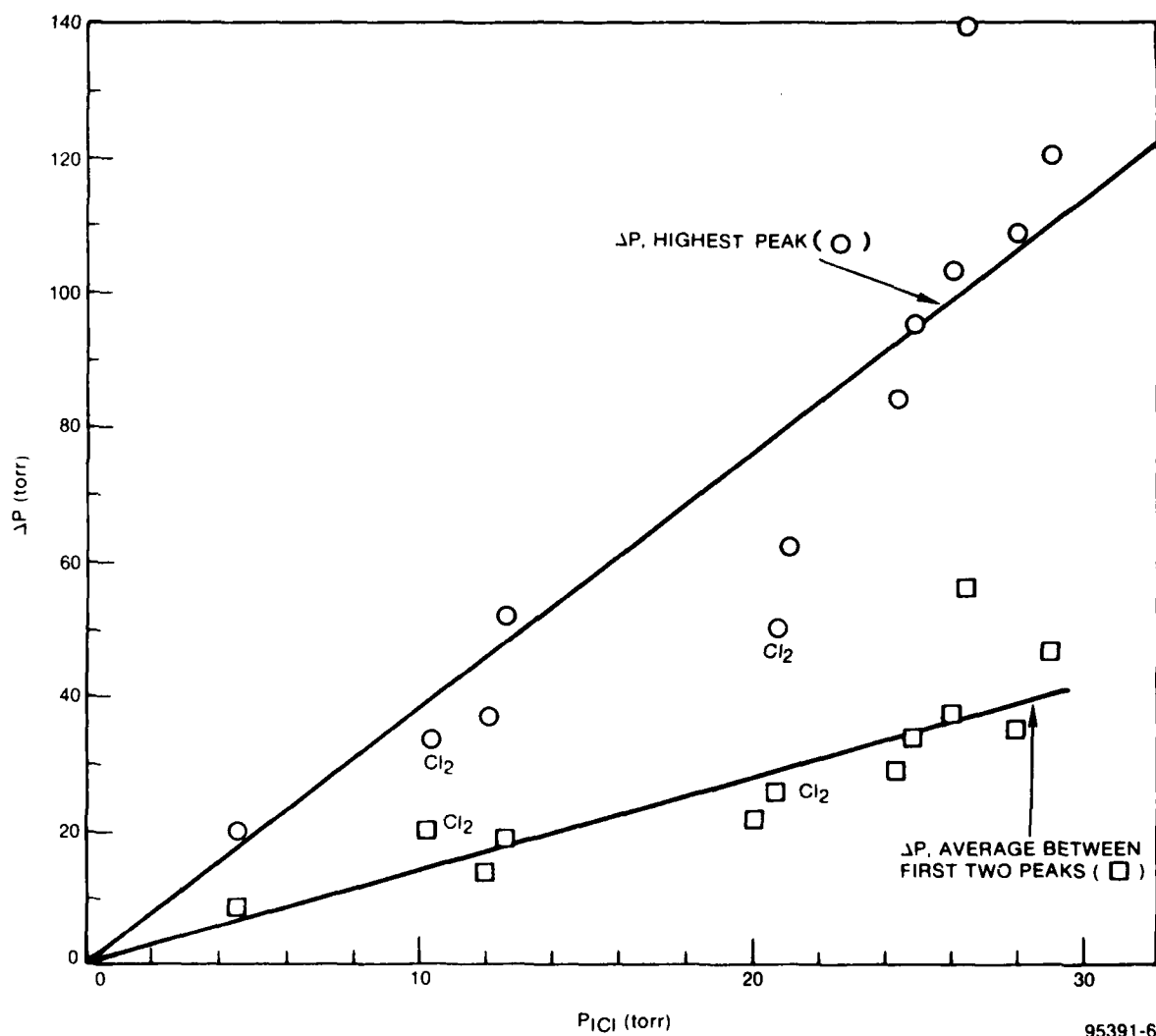


Figure 47. Observed pressure rise in ICl.

## ANALYSIS AND INTERPRETATION

This section of the report includes results of analyses conducted to correlate the experimental results with an understanding of the relevant physics and chemistry. Analytical methods have included a variety of simple calculations to estimate or interpret behavior for macroscopic observables. A detailed kinetic model was also developed and the relevant coupled equations were solved numerically using a Rocketdyne computer program.

### NUMERICAL ANALYSIS

#### Computer Program Description

The computer program used for this study was derived from the Advanced Cavity Code (ACC), which had been developed by Rocketdyne for chemical laser cavity performance evaluations (Ref. 14, 15). The discussion and computations presented here apply to the small flashlamp, cylindrical geometry arrangement. Modification to set up the geometry applicable to the large flashlamp experiments would be straightforward.

Input to and output from the model are indicated in Table 8. The phenomena which are modeled include absorption and photodissociation, two body, three body, and wall reactions, thermal radiation, heat and mass transport within the gas and heat transfer with the walls. Options include conducting or insulating walls, and the addition of turbulence to enhance transport phenomena, and specification of wall reflectivity.

For photodissociation, the energy transfer is considered to be unidirectional, i.e., normal to the flashlamp surface and to be accompanied by photolytic reactions. Photodissociation is treated as a two-step process. The first step is the dissociation of molecules into atoms in which the photoenergy is stored. The rate of dissociation is given by the rate of photoenergy absorbed divided by the molecule energy for dissociation (i.e., photon energy). The second step is the deactivation of the dissociated atoms to ground state.

This is a thermalization process by which the stored photoenergy is released and heats the fluid. The local photoenergy flux is calculated by a rate

TABLE 8. MODEL OPERATION

INPUT TO MODEL	OUTPUT FROM MODEL
LAMP SPECTRUM, $\int \phi(\lambda, t) dt / \Delta t$	$-[X_i](t, r)$
LAMP TEMPORAL BEHAVIOR, $\int \phi(\lambda, t) d\lambda$	$-P(t)$ $-T(t, r)$
THERMAL DATA	$-q_{wall}$
KINETIC RATE PACKAGE	
SPECTROSCOPIC DATA PACKAGE	
REACTANT ABSORPTION COEFFICIENT	
PRODUCT ABSORPTION COEFFICIENT	
INITIAL CONDITIONS: $P, T, [X_i]$	
GEOMETRY AND BOUNDARY CONDITIONS	

Where:  $\phi$  = Photo flux  
 $\lambda$  = Wavelength  
 $t$  = Time  
 $[X_i]$  = Concentration of species  $i$   
 $P$  = Pressure  
 $T$  = Temperature  
 $q$  = Heat flux

equation, which states that the rate of decrease in energy is equal to the amount absorbed.

For thermal radiation, the energy transfer is random in direction and is not directly related to chemical reactions. Thermal radiation in the gas, due to the random nature, is governed by integro-differential equations. The method of differential approximation is employed by which the equations are reduced to ordinary differential form. This method is equivalent to the Milne-Eddington approximation commonly used in astrophysics. The radiative heat flux is due to emission minus absorption. The emission term is a strong function of temperature, while the absorption term is itself coupled to the radiative heat flux.

#### Kinetic Data Set

The numerical analysis program requires as input a chemical kinetic data package including species, reactions, and rates. The reaction rate set which was developed under this program is shown in Tables 9-11.

#### Spectroscopic and Radiometric Data Set

Spectroscopic and radiometric data input to the RKM model comprises parameters describing flashlamp intensity as a function of wavelength and time, reactant extinction coefficients as a function of wavelength and temperature, and product extinction coefficients as a function of wavelength and temperature.

The lamp spectral and temporal radiant output may be represented by  $\phi(\lambda, t)$ . Based on discussions with lamp vendors, the total radiant output was taken as 35% of the electrical energy input, which was measured:

$$\phi(\lambda, t) d\lambda dt = 0.35 \times \int I(t) \cdot V(t) dt. \cong 0.35 \times 1/2 CV^2$$

where

$\lambda$  = wavelength

$t$  = time

$I(t)$  = lamp current

$V(t)$  = lamp voltage

$V_c$  = charging voltage

$C$  = capacitance

TABLE 9. RECOMBINATION RATES

REACTION	M	H kcal/mol	k, cm <sup>6</sup> /s 300°K	RECOMMENDED VALUES			REFS
				A (cm <sup>6</sup> /s)	N	E (kcal)	
Cl + Cl + M = Cl <sub>2</sub> + M	n Cl <sub>2</sub>	- 57.844	5.5 x 10 <sup>-32</sup>	3.7 x 10 <sup>-33</sup>		-1.6	17
	He		6.3 x 10 <sup>-33</sup>	4.1 x 10 <sup>-33</sup>		-0.26	17,18
	n H <sub>2</sub>		1.9 x 10 <sup>-32</sup>	2.5 x 10 <sup>-31</sup>	-0.88	-1.44	22
	ICl		2.5 x 10 <sup>-30</sup>				23
	I <sub>2</sub>		3.8 x 10 <sup>-30</sup>				23
	n HCl		6.2 x 10 <sup>-33</sup>	8.4 x 10 <sup>-32</sup>	-0.88	-1.44	22
	n Cl		1.2 x 10 <sup>-31</sup>	1.7 x 10 <sup>-30</sup>	-0.88	-1.44	22
	n H		3.7 x 10 <sup>-32</sup>	5.0 x 10 <sup>-31</sup>	-0.88	-1.44	22
	n SF <sub>6</sub>		3.3 x 10 <sup>-32</sup>	4.5 x 10 <sup>-31</sup>	-0.88	-1.44	17
							23
I + I + M = I <sub>2</sub> + M	Cl <sub>2</sub>	- 51.074	5.6 x 10 <sup>-32</sup>				23
	He		6.4 x 10 <sup>-33</sup>	1.4 x 10 <sup>-36</sup>	0.8	-2.3	19,20,21
	H <sub>2</sub>		9.6 x 10 <sup>-33</sup>				19
	ICl		2.5 x 10 <sup>-30</sup>				19,20
	I <sub>2</sub>		3.8 x 10 <sup>-30</sup>	5.5 x 10 <sup>-26</sup>	-2.36	-2.31	23
	HCl		3.2 x 10 <sup>-33</sup>				23
	Cl		6.3 x 10 <sup>-32</sup>				23
	H		1.9 x 10 <sup>-32</sup>				23
	Cl <sub>2</sub>		5.6 x 10 <sup>-32</sup>				23
	He		6.4 x 10 <sup>-33</sup>				23
I + Cl + M = ICl + M	H <sub>2</sub>	-103.086	9.5 x 10 <sup>-33</sup>				23
	ICl		1.2 x 10 <sup>-30</sup>				23
	I <sub>2</sub>		1.8 x 10 <sup>-30</sup>				23
	HCl		3.2 x 10 <sup>-33</sup>				23
	Cl		6.4 x 10 <sup>-32</sup>				23
	H		1.9 x 10 <sup>-32</sup>				23
	Cl <sub>2</sub>		4.8 x 10 <sup>-32</sup>	5.4 x 10 <sup>-26</sup>	-2.0	1.5	22
	He		1.6 x 10 <sup>-32</sup>	1.8 x 10 <sup>-26</sup>	-2.0	1.5	22
	n H <sub>2</sub>		1.6 x 10 <sup>-32</sup>	1.8 x 10 <sup>-26</sup>	-2.0	1.5	22
	ICl		1.6 x 10 <sup>-32</sup>				22
H + Cl + M = HCl + M	I <sub>2</sub>		1.6 x 10 <sup>-32</sup>				22
	n HCl		8.0 x 10 <sup>-32</sup>	9.0 x 10 <sup>-26</sup>	-2.0	1.5	22
	n Cl		8.0 x 10 <sup>-32</sup>	9.0 x 10 <sup>-26</sup>	-2.0	1.5	22
	n H		8.0 x 10 <sup>-32</sup>	9.0 x 10 <sup>-26</sup>	-2.0	1.5	22
	n SF <sub>6</sub>		1.6 x 10 <sup>-32</sup>	1.8 x 10 <sup>-26</sup>	-2.0	1.5	22
							24,25
	H + I + M = HI + M		2.0 x 10 <sup>-32</sup>				22
	H + H + M = H <sub>2</sub> + M		7.6 x 10 <sup>-33</sup>	1.7 x 10 <sup>-30</sup>	-0.95	0.0	22
			7.6 x 10 <sup>-33</sup>	1.7 x 10 <sup>-30</sup>	-0.95	0.0	22
			8.0 x 10 <sup>-33</sup>	2.6 x 10 <sup>-31</sup>	-0.61	0.0	22
O <sub>2</sub> + Cl + M = ClO <sub>2</sub> + M	HCl	-104.208	7.6 x 10 <sup>-33</sup>	1.7 x 10 <sup>-30</sup>	-0.95	0.0	22
	H		1.5 x 10 <sup>-31</sup>	3.4 x 10 <sup>-29</sup>	-0.95	0.0	22
	Cl		7.6 x 10 <sup>-33</sup>	1.7 x 10 <sup>-30</sup>	-0.95	0.0	22
	SF <sub>6</sub>		7.6 x 10 <sup>-33</sup>	1.7 x 10 <sup>-30</sup>	-0.95	0.0	22
	n Cl <sub>2</sub>		1.7 x 10 <sup>-33</sup>				37
	n He		1.7 x 10 <sup>-33</sup>				37
	n H <sub>2</sub>		1.7 x 10 <sup>-33</sup>				37
	n HCl		1.7 x 10 <sup>-33</sup>				37
	n H		1.7 x 10 <sup>-33</sup>				37
	n Cl		1.7 x 10 <sup>-33</sup>				37
O <sub>2</sub> + H + M = HO <sub>2</sub> + M	n SF <sub>6</sub>		1.7 x 10 <sup>-33</sup>				37
	n Cl <sub>2</sub>		5.6 x 10 <sup>-32</sup>	2.1 x 10 <sup>-32</sup>	0.0	-0.58	37
	n He		1.8 x 10 <sup>-32</sup>	6.7 x 10 <sup>-33</sup>	0.0	-0.58	37
	n H <sub>2</sub>		1.8 x 10 <sup>-32</sup>	6.7 x 10 <sup>-33</sup>	0.0	-0.58	37
	n HCl		5.6 x 10 <sup>-32</sup>	2.1 x 10 <sup>-32</sup>	0.0	-0.58	37
	n H		1.8 x 10 <sup>-32</sup>	6.7 x 10 <sup>-33</sup>	0.0	-0.58	37
	n Cl		1.8 x 10 <sup>-32</sup>	6.7 x 10 <sup>-33</sup>	0.0	-0.58	37
	n SF <sub>6</sub>		5.6 x 10 <sup>-32</sup>	2.1 x 10 <sup>-32</sup>	0.0	-0.58	37

n = New Reaction or Modified Rate

TABLE 10. EINSTEIN COEFFICIENTS FOR SPONTANEOUS EMISSION

REACTION	V	$\Delta H$ kcal/mol	$A(\text{sec}^{-1})$	REFS
$\text{HCl}(v) = \text{HCl}(v-1) + h\nu$	1	8.250	34.6	36
	2		59.4	36
	3		74.7	36
	4		81.1	36
	5		79.7	36
	6		71.9	36
			71.9	36

TABLE 11. MOLECULAR REACTIONS

REACTION	v	$\Delta H$ kcal/mole	k, cm <sup>3</sup> /s 300°K	RECOMMENDED VALUES			REFS
				A(cm <sup>3</sup> /s)	N	E(kcal)	
Cl + H <sub>2</sub> = HCl(v) + H	0	1.114	1.2 x 10 <sup>-14</sup>	8.0 x 10 <sup>-11</sup>		5.26	22,26
H + Cl <sub>2</sub> = HCl(v) + Cl	1	-36.996	4.1 x 10 <sup>-13</sup>	1.1 x 10 <sup>-11</sup>	0.163	2.52	22,26
	2		1.5 x 10 <sup>-12</sup>	4.0 x 10 <sup>-11</sup>			22
	3		1.4 x 10 <sup>-12</sup>	3.7 x 10 <sup>-11</sup>			
	4		1.4 x 10 <sup>-13</sup>	3.8 x 10 <sup>-12</sup>			
	5		7.0 x 10 <sup>-14</sup>	1.9 x 10 <sup>-12</sup>			
	6		7.0 x 10 <sup>-15</sup>	1.9 x 10 <sup>-13</sup>			
HCl(v) + HCl = HCl(v-1) + HCl	1-6	- 8.250	2.3 x 10 <sup>-14</sup> <sub>v</sub>	1.3 x 10 <sup>-21</sup> <sub>v</sub>	2.6	-1.11	22
HCl(v) + H <sub>2</sub> = HCl(v-1) + H <sub>2</sub>	1-6	- 8.250	5.3 x 10 <sup>-15</sup> <sub>v</sub>	1.6 x 10 <sup>-20</sup> <sub>v</sub>	2.23		22
HCl(v) + H = HCl(v') + H	v' < v	- 8.250	2.8 x 10 <sup>-11</sup>	8.3 x 10 <sup>-11</sup>		0.65	22
HCl(v) + Cl <sub>2</sub> = HCl(v-1) + Cl <sub>2</sub>	1-6	- 8.250	7.5 x 10 <sup>-15</sup> <sub>v</sub>	8.3 x 10 <sup>-20</sup> <sub>v</sub>	2.0		22
HCl(v) + Cl = HCl(v') + Cl	v' < v	- 8.250	1.0 x 10 <sup>-11</sup>	3.3 x 10 <sup>-11</sup>		0.70	22
HCl(v) + He = HCl(v-1) + He	1-6	- 8.250	4.9 x 10 <sup>-17</sup> <sub>v</sub>	2.0 x 10 <sup>-29</sup> <sub>v</sub>	5.0		22
HCl(v) + HCl(v') = HCl(v+1) + HCl(v'-1)	1 ≤ v' ≤ v	> - .290	2.2 x 10 <sup>-12</sup> <sub>v'(v+1)</sub>	6.6 x 10 <sup>-10</sup> <sub>v'(v+1)</sub>	-1.0		22
Cl + ICl = Cl <sub>2</sub> + I		- 7.569	3.0 x 10 <sup>-10</sup>			2.15	27
Cl + I <sub>2</sub> = ICl + I		-14.126	1.7 x 10 <sup>-10</sup>	3.0 x 10 <sup>-10</sup>		.34	27,28
H + ICl = HCl(v) + I	1	-44.561	4.4 x 10 <sup>-12</sup>	2.2 x 10 <sup>-11</sup>		.94	29,30
	2		5.4 x 10 <sup>-12</sup>	2.6 x 10 <sup>-11</sup>			
	3		7. x 10 <sup>-12</sup>	3.6 x 10 <sup>-11</sup>			
	4		9.9 x 10 <sup>-12</sup>	4.8 x 10 <sup>-11</sup>			
	5		9.9 x 10 <sup>-12</sup>	4.8 x 10 <sup>-11</sup>			
	6		8.4 x 10 <sup>-12</sup>	4.1 x 10 <sup>-11</sup>			
	7		4.0 x 10 <sup>-12</sup>	1.9 x 10 <sup>-11</sup>			
H + I <sub>2</sub> = HI + I	0		1.7 x 10 <sup>-10</sup>	1.7 x 10 <sup>-10</sup>			30
Cl + HI = HCl(v) + I	1		1.2 x 10 <sup>-11</sup>	2.1 x 10 <sup>-2</sup>	-4.47	2.99	31-33
	2			4.0 x 10 <sup>-2</sup>			
	3			1.1 x 10 <sup>-3</sup>			
	4			8.4 x 10 <sup>-2</sup>			
H + HI = H <sub>2</sub> (v) + I	0	-32.863	1.1 x 10 <sup>-10</sup>	2.7 x 10 <sup>-12</sup>	0.5	- .52	34,35
Cl + ClO <sub>2</sub> = Cl <sub>2</sub> + O <sub>2</sub>	- n		1.56 x 10 <sup>-10</sup>	1.56 x 10 <sup>-10</sup>	-	-	37
H + ClO <sub>2</sub> = HCl(O) + O <sub>2</sub>	- n		2.0 x 10 <sup>-10</sup>	2.0 x 10 <sup>-10</sup>	-	-	37
Cl + HO <sub>2</sub> = HCl(O) + O <sub>2</sub>	- n		6.0 x 10 <sup>-11</sup>	6.0 x 10 <sup>-11</sup>	-	-	37
H + HO <sub>2</sub> = H <sub>2</sub> + O <sub>2</sub>	- n		1.3 x 10 <sup>-11</sup>	4.2 x 10 <sup>-11</sup>		.7	37

n = New Reaction or Modified Rate

It was further assumed that the spectral and temporal dependences were uncoupled and were given by normalizations of the lamp spectrum  $F(\lambda)$  given by Gonz and Newell (Ref. 16) and shown earlier in Figure 6 and of the temporal behavior observed here as  $\Phi_{330}(t)$  and shown earlier in e.g. Figure 26. Thus,  $\Phi(\lambda, t)$  was represented as

$$\Phi(\lambda, t) = \frac{F(\lambda)}{\int F(\lambda) d\lambda} \times \frac{\Phi_{330}(t)}{\int \Phi_{330}(t) dt} \times 0.35 \times \int I(t) \times V(t) dt$$

or

$$= \frac{F(\lambda)}{\int F(\lambda) d\lambda} \times \frac{\Phi_{330}(t)}{\int \Phi_{330}(t) dt} \times 0.35 \times \frac{1}{2} CV^2$$

### Sample Calculations

The computer program provides graphical output in the form of parameter values plotted against time. Figure 48, for example shows the pressure in units of dynes/cm<sup>2</sup> vs. time. Each major mark on the time base is 1 ms and the plot runs to 10 ms. Figure 49 shows the Cl<sub>2</sub> concentration in mol fraction plotted against the same time base. The data plotted refer to node 15 in the computation, which is at the wall of the cylindrical reactor with the small flashlamp on the cylinder axis. The computation was for a 100 J discharge in 207 torr SF<sub>6</sub>, 62 torr of Cl<sub>2</sub> and 248 torr of H<sub>2</sub>.

### Correlation of Results

Cl<sub>2</sub> + SF<sub>6</sub>. Results from a series of tests with Cl<sub>2</sub> and SF<sub>6</sub> in the small flashlamp system were shown in Table 5. That test series represented a constant SF<sub>6</sub> concentration with Cl<sub>2</sub> concentration being varied by up to a factor of 20. When the experiments were modeled using the rates from Tables 9-11, the results shown in Figure 50 were obtained. The computed peak pressure rise increases with Cl<sub>2</sub> concentration in excellent agreement with the observed trend. A relatively constant offset of about 2 torr was observed, with the computed result being higher.

Cl<sub>2</sub> + H<sub>2</sub> + SF<sub>6</sub>. Results from a series of tests with Cl<sub>2</sub>, H<sub>2</sub>, and SF<sub>6</sub> in the small flashlamp system were shown earlier in Table 6. Obtaining computational results in agreement with the Table 6 experimental results proved to be difficult. When the difficulties were recognized, it was decided



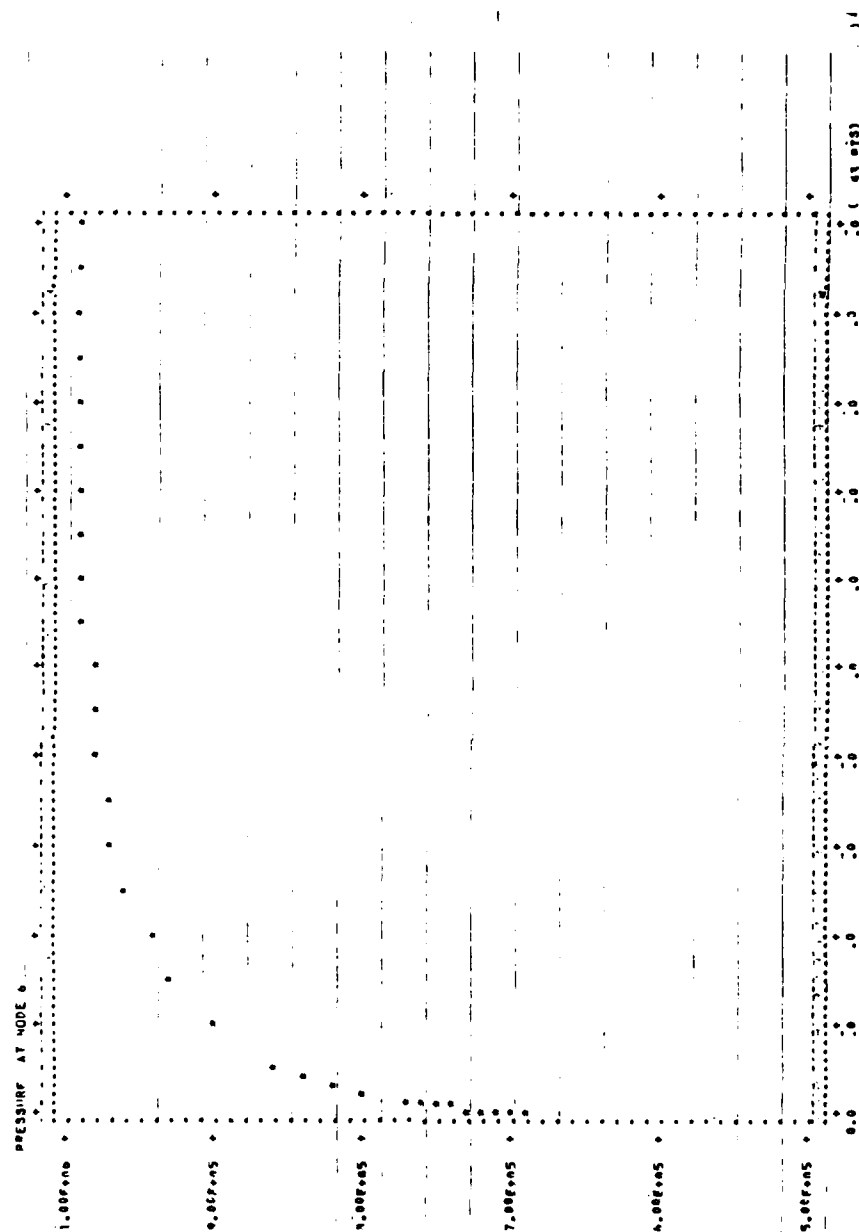


Figure 48. Sample computed results, pressure vs time.

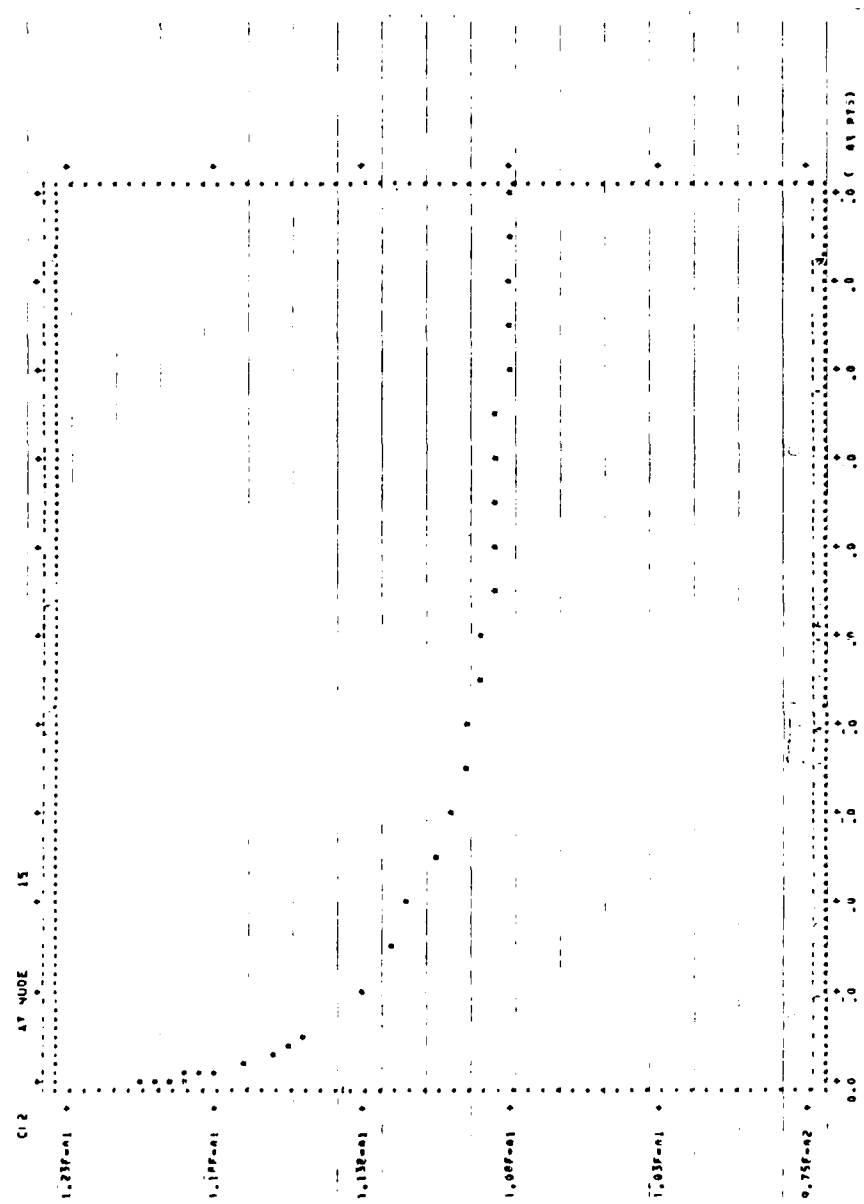


Figure 49. Sample computed results,  $Cl_2$  concentration vs time.

AD-A163 983

RADIATION AUGMENTED PROPULSION FEASIBILITY(U) ROCKWELL  
INTERNATIONAL CANOGA PARK CA ROCKETDYNE DIV  
S C HURLOCK ET AL DEC 85 RI/RD85-257 AFRPL-TR-85-068  
F04611-84-C-0047

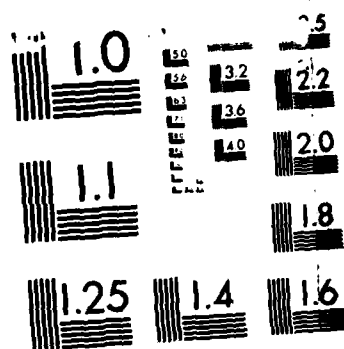
2/2

UNCLASSIFIED

F/G 10/1

NL





MICROCOPY RESOLUTION TEST CHART  
NATIONAL BUREAU OF STANDARDS-1963-A

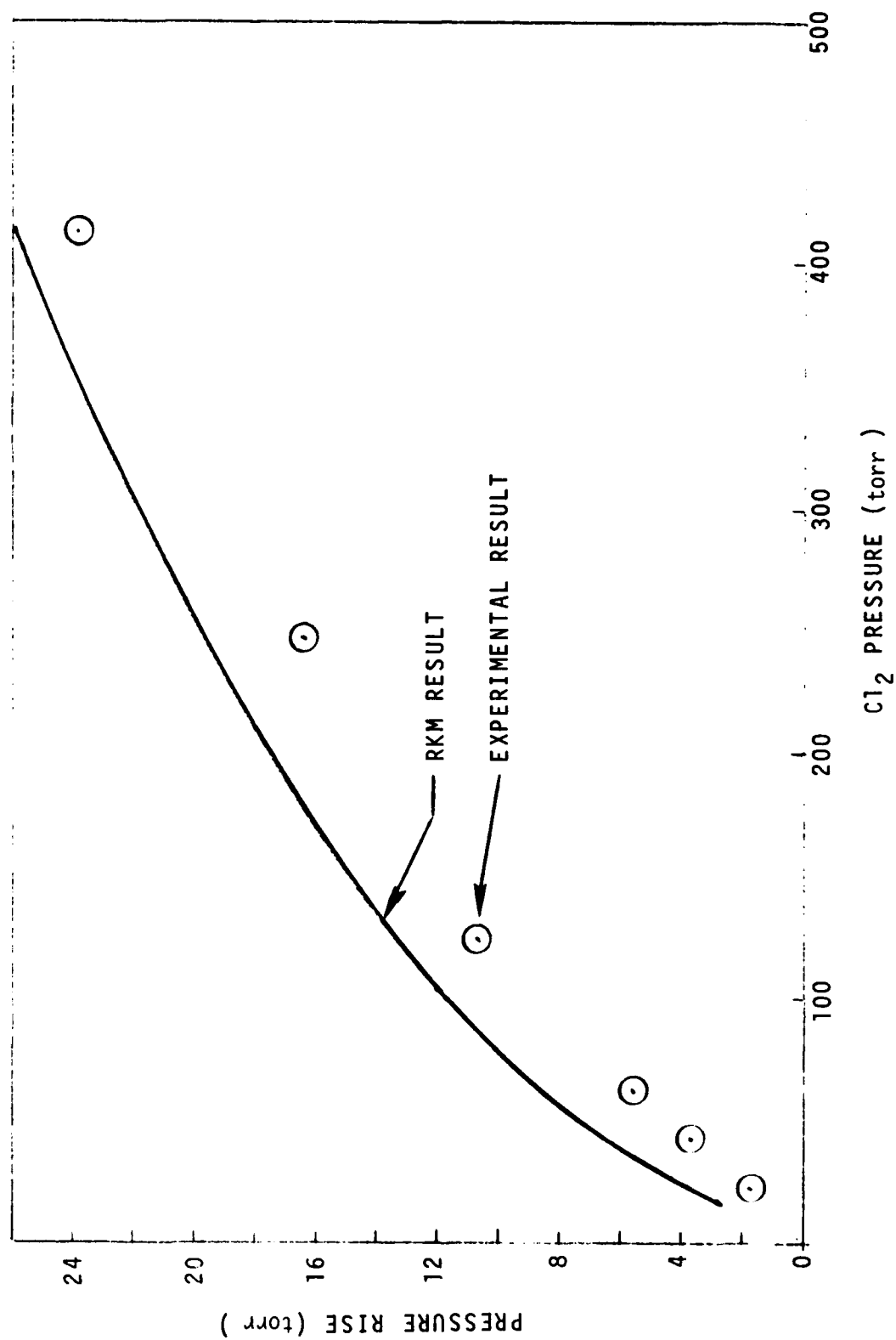


Figure 50. Pressure rise in  $\text{Cl}_2 + \text{SF}_6$  ( $P_{\text{SF}_6} = 200$  torr).

to try to anchor the model to the run with the largest observed pressure rise, 3/11/85: 8/1. The difficulties lay in getting the  $\text{H}_2 + \text{Cl}_2$  chain reaction to terminate and in getting simultaneous agreement with the observed pressure rise and  $\text{Cl}_2$  consumption. In order to try to improve the agreement, atom-atom recombination rates with  $\text{SF}_6$  as the third body were varied. Other relevant rates were considered too well known to justify changing them. In the following paragraphs, attempts to improve agreement between experiment and theory are summarized.

1. Establishing bounds on  $\text{SF}_6$  three body rate excursions was accomplished by computing 3/11/85: 8/1 results with  $\text{SF}_6$  rates from 1 to 100 times those in Table 9. All  $\text{SF}_6$  rates were multiplied by the same factor. At 100x the baseline rates, much less reaction occurred than had been observed experimentally. At 10x, both the  $\Delta P$  and the  $\Delta \text{Cl}_2$  were in reasonable agreement with experiment in the  $3 \times 10^{-3}$ s to  $6 \times 10^{-3}$ s time regime. However, the reaction was continuing and clearly would go to near completion if the computation were continued. This revealed an important aspect of the model which was confirmed in subsequent computations:  $\text{SF}_6$  alone as a third body chain terminator could not account for the experimentally observed  $\Delta P$  and  $\Delta \text{Cl}_2$  endpoints.
2. Estimating the best choice for the  $\text{SF}_6$  three body recombination rates was accomplished by computing 3/11/85: 8/1 results with  $\text{SF}_6$  rates of 10x, 30x, 40x, and 50x those in Table 7. The best results ( $\Delta P = 470$  Torr,  $\Delta \text{Cl}_2 = 0.53$ , at  $t = 6 \times 10^{-3}$ s) were obtained at 40x. However, the reaction had not terminated and  $\Delta P$  and  $\Delta \text{Cl}_2$  were still rising.
3. Wall reactions, particularly wall-catalyzed recombination, could help to terminate the chain. They were included at this point (along with the 40x  $\text{SF}_6$  rates) at an efficiency of 100%. A few percent reduction in  $\Delta P$  and  $\Delta \text{Cl}_2$  was obtained at corresponding times but the chain was not terminated.
4. Some turbulent mixing was evidently occurring experimentally as evidenced by acoustic phenomena in the cell. The laminar diffusion mixing was enhanced in the model to simulate this phenomena. The diffusion coefficient was increased by about 100x and 1000x to bring the reactants

to the catalytic wall more rapidly. Using this approach, with simultaneous variation in the  $\text{SF}_6$  rates, good agreement with  $\Delta P$  and  $\Delta \text{Cl}_2$  could not be obtained. Furthermore, the chain was not terminated under those conditions which gave the best  $\Delta P$ ,  $\Delta \text{Cl}_2$  match to the experimental data.

5. Two other phenomena which were examined were the  $\text{H} + \text{SF}_6$  reaction and equilibrium thermal dissociation of  $\text{Cl}_2$ . Neither of these effects could account for the observed results.
6. Inclusion of  $\text{O}_2$ , resulting from air inleakage, was found to provide the needed chain termination. Figure 51 shows the sensitivity of  $\Delta \text{Cl}_2$  and  $\Delta P$  to  $\text{O}_2$  concentration for two different  $\text{SF}_6$  rate sets.  $\text{O}_2$  concentrations in a reasonable range are shown to provide agreement with the observed  $\Delta P$ ,  $\Delta \text{Cl}_2$  results for the test case, when coupled with  $\text{SF}_6$  rates 10x-15x these in Table 9. More importantly, the computations showed termination of the chain at the values plotted. Wall reactions and turbulent mixing were not included in these runs.

Figure 52 shows the results of the model, with 0.04 torr of  $\text{O}_2$  and the 10x  $\text{SF}_6$  rate set applied to the test cases of Table 6. The pressure rise is computed to be somewhat lower than the experimental values except for the test case 8/1. Deviation of the  $\text{Cl}_2$  consumption calculation from the experiments is quite severe, except for the test case. At this point, it is believed that the model contains all the features needed to correlate the data and that optimization of the agreement with the data points shown in Figure 52 could be accomplished through adjustment of the  $\text{SF}_6$  rates and the  $\text{O}_2$  partial pressures (which were not necessarily the same for all the experiments). Because of the lack of  $\text{O}_2$  partial pressure data and the expense of the computations, this optimization was not attempted.

#### ANALYSIS OF RESULTS FROM LARGE FLASHLAMP SYSTEM

The observational results presented earlier are discussed and interpreted in this section. Analytical methods involved application of basic spectroscopic,

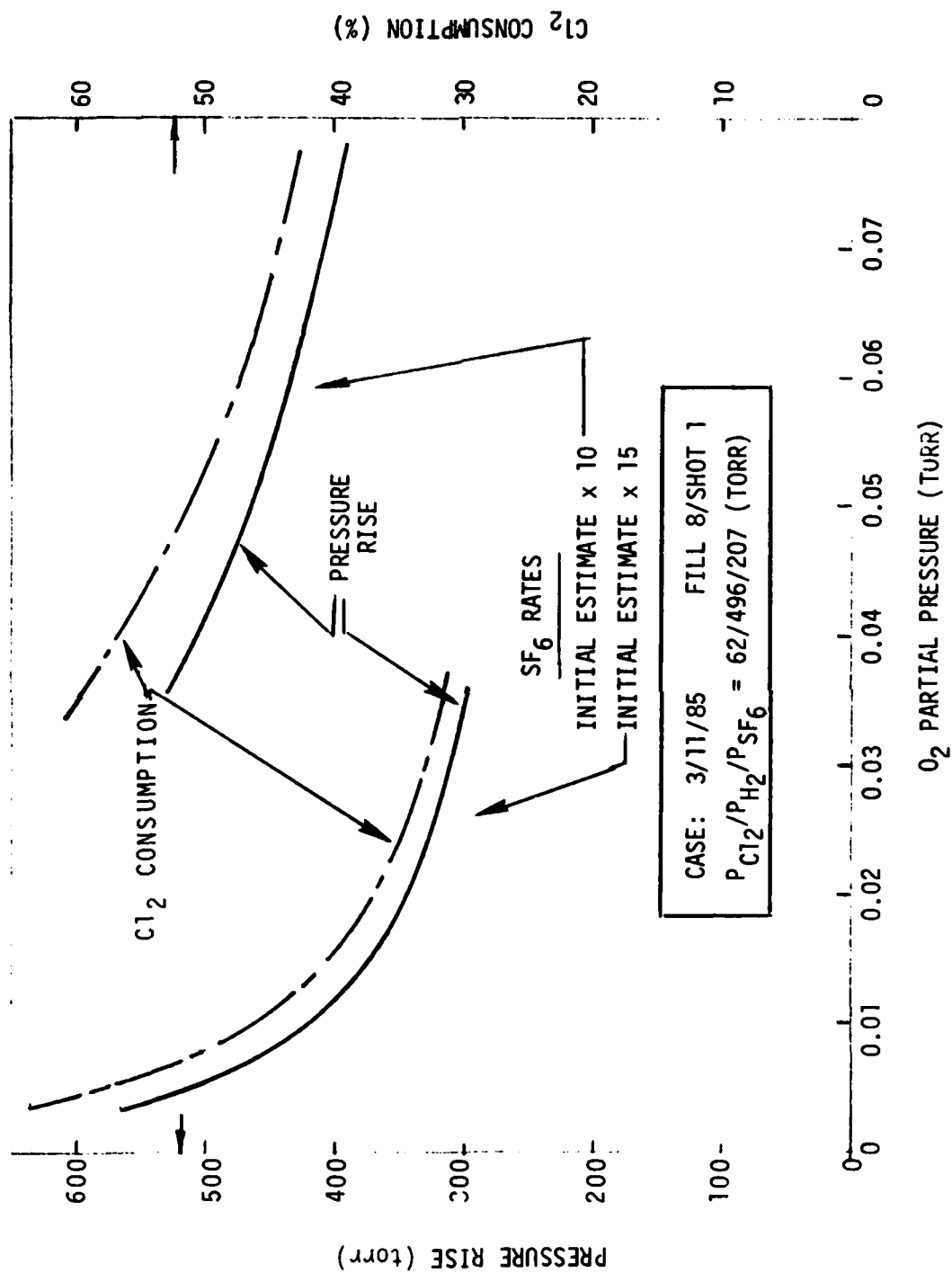


Figure 51. Sensitivity of computational results to model parameters (arrows indicate data).



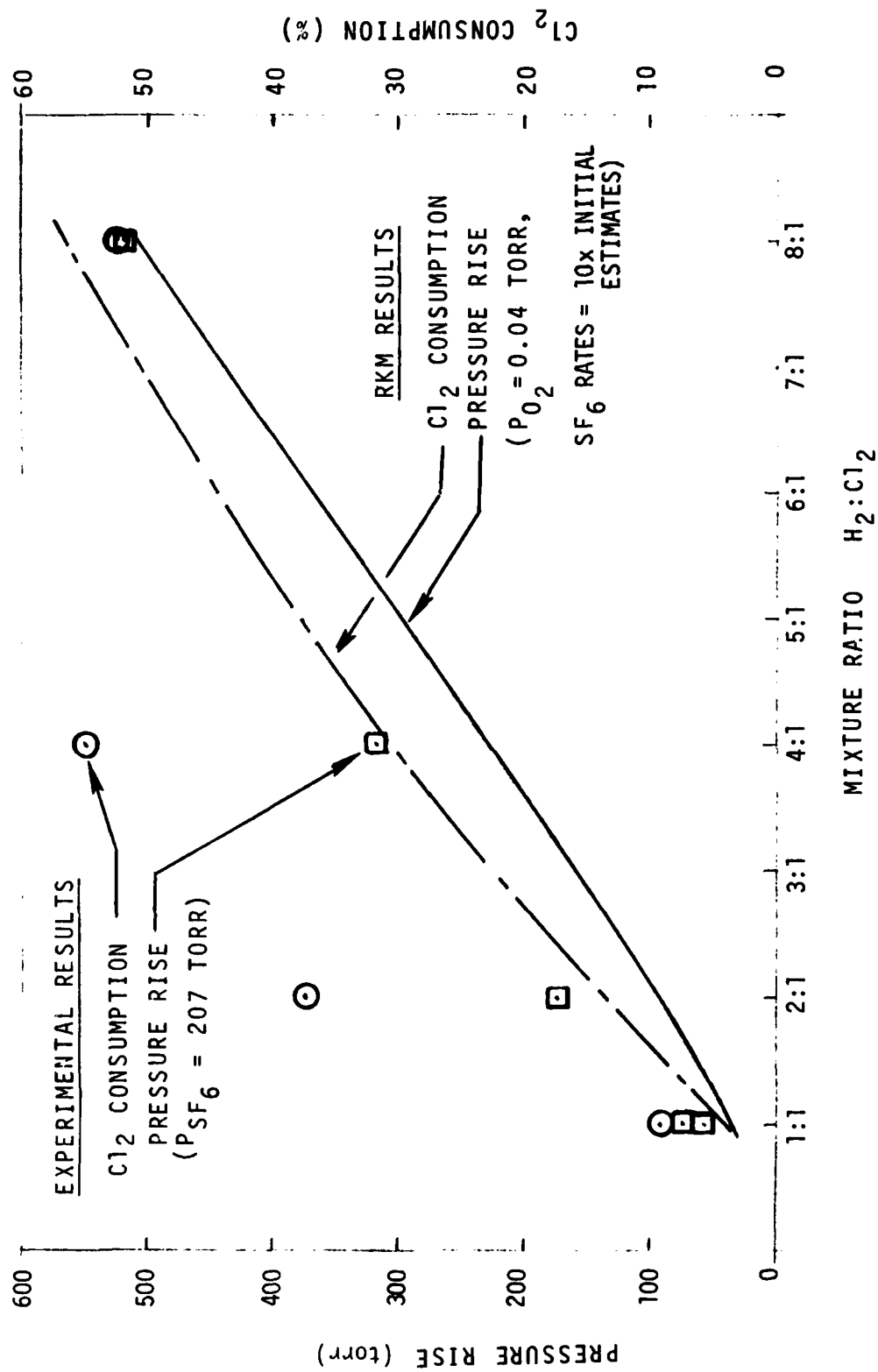


Figure 52.  $SF_6 + H_2 + Cl_2$  results.

chemical and thermodynamic principles. The numerical model was not applied to correlate results obtained with this system.

#### Energy Deposition and Release in Cl<sub>2</sub>

Flux available from the lamp was modelled as dependent on  $1/r$  where  $r$  is the distance from the lamp centerline. It was assumed that 35% of the electrical energy deposited was available as light and was uniformly distributed over the area of the lamp outer wall having a radius of 1.2 cm and a length of 100 cm. The flux available at the reactor inlet window, 4.5 cm from the lamp centerline, was thus taken as  $1.1 \text{ J/cm}^2$  for a 29  $\mu\text{F}$ , 25 kV discharge energy.

The energy receiving capacity of Cl<sub>2</sub> in the reactor depends on the pressure-path length product. If a 334 nm photon (peak of Cl<sub>2</sub> absorption) is absorbed per molecule, the energy capacity in the 10 cm long cell depends on the Cl<sub>2</sub> pressure according to

$$E(\text{J/cm}^2) = 57.4 \times \frac{P(\text{torr})}{T(^{\circ}\text{K})}$$

This energy capacity of the Cl<sub>2</sub> is plotted in Figure 53. When the fraction of the lamp energy at each wavelength (from the assumed lamp spectrum) is multiplied by the Cl<sub>2</sub> absorption as a function of pressure and the product is integrated over the wavelength range of the Cl<sub>2</sub> absorption, the amount of lamp flux which is absorbed is also shown in Figure 53. The ratio of the energy absorbed and the energy capacity gives the fraction of the Cl<sub>2</sub> absorbed, which is also plotted in Figure 53.

The energy absorbed by the Cl<sub>2</sub> leads, after thermalization, to a temperature rise. This can be estimated using the amount of energy absorbed and the heat capacity, according to

$$\Delta T = \frac{E}{nC_v}$$

where  $n$  = number of mols/cm<sup>2</sup> and  $C_v$  is the heat capacity at constant volume, which is  $6.132 \text{ cal mol}^{-1} \text{ deg}^{-1}$  at 300K.

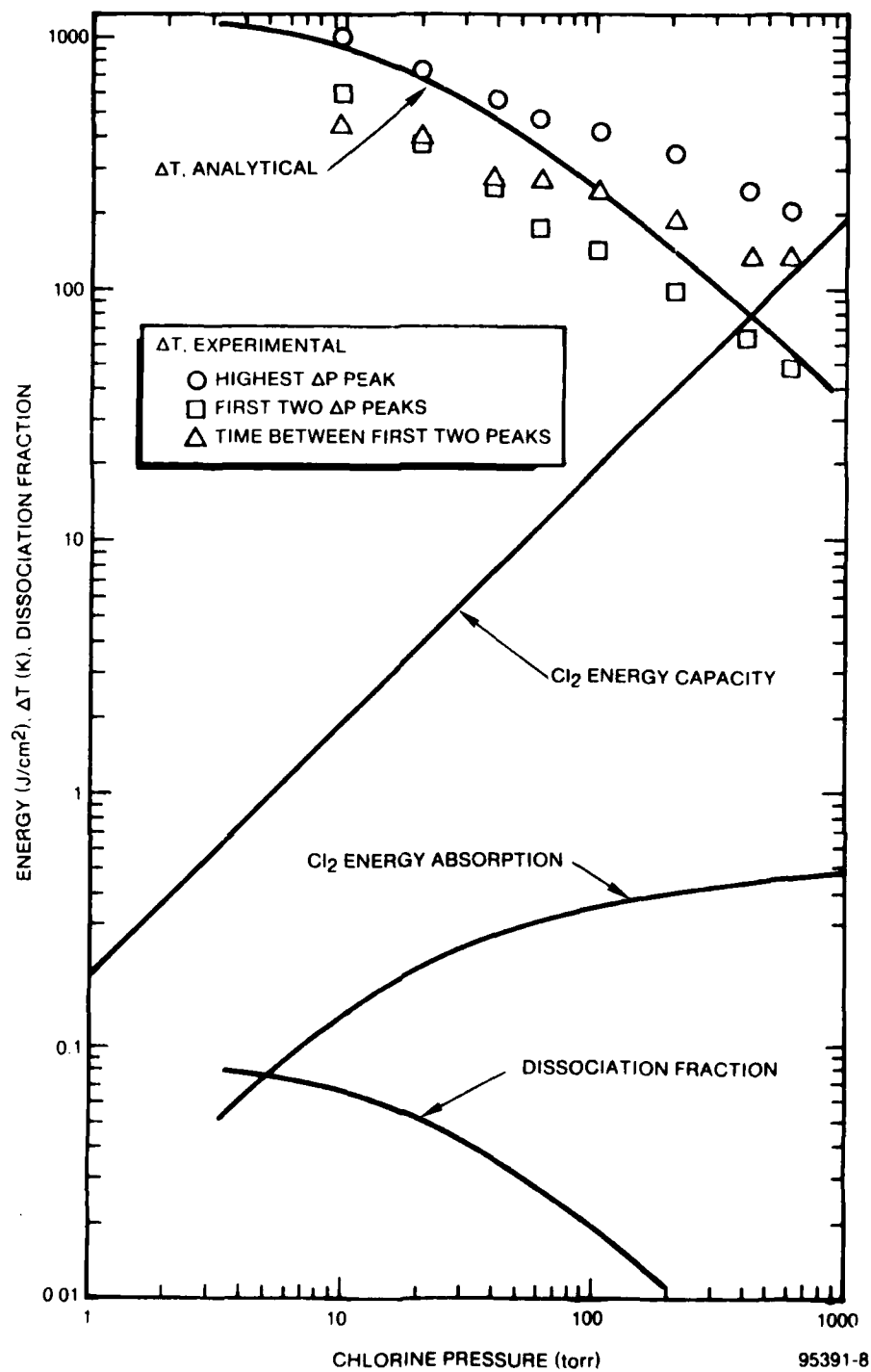


Figure 53. Analysis for temperature rise in Cl<sub>2</sub>.

The  $\Delta T$  estimate is also plotted in Figure 53. For comparison, observational results presented earlier are also plotted on the figure. The  $\Delta T$  results shown earlier in Figure 41 are plotted directly. The  $\Delta P$  results shown in Figure 41 were used to derive a  $\Delta T$  using

$$\Delta P/P = \Delta T/T$$

with  $T$  taken as 300K.

Considering the assumptions made in deriving the  $\Delta T$  predictions in this section, and the difficulties described earlier in obtain  $\Delta P$  and  $\Delta T$  values from the data records, the agreement is quite satisfactory. The fact that the different  $\Delta T$  determination methods provide agreement with the prediction in different pressure regions may provide further insight into the predictive and data reduction methods but this has not been pursued.

#### Energy Deposition and Release in $Cl_2 + H_2$

The final temperature in this system is achieved through the thermalization of the absorbed flashlamp radiation plus the chemical energy released by the exothermic formation of HCl from the elements.

$$\Delta T = \frac{E(\text{absorbed}) + E(\text{chemical})}{n_{HCl} C_{v,HCl} + n'_{H_2} C_{v,H_2} + n'_{Cl_2} C_{v,Cl_2}}$$

where  $n'_{H_2}$  and  $n'_{Cl_2}$  represent any reactants which remain after the chain

reaction has been terminated. For the analysis presented here, complete reaction is assumed. With the 10.3 torr and 20.7 torr partial pressures of  $Cl_2$  for which  $Cl_2 + H_2$  tests were conducted, the absorbed energy, discussed in the previous section, is about 10% of the chemical energy. This percentage goes down as the  $Cl_2$  pressure goes up, resulting in a slightly lower predicted  $\Delta T$  for the 20.7 torr than for the 10.3 torr cases. Figure 54 shows the calculated temperature rise plotted as a function of  $H_2:Cl_2$  ratio. Experimentally determined results are included on the plot for comparison. The experimental values are those determined using the average pressure rise over the first two  $\Delta P$  peaks and then employing  $\Delta P/P = \Delta T/T$

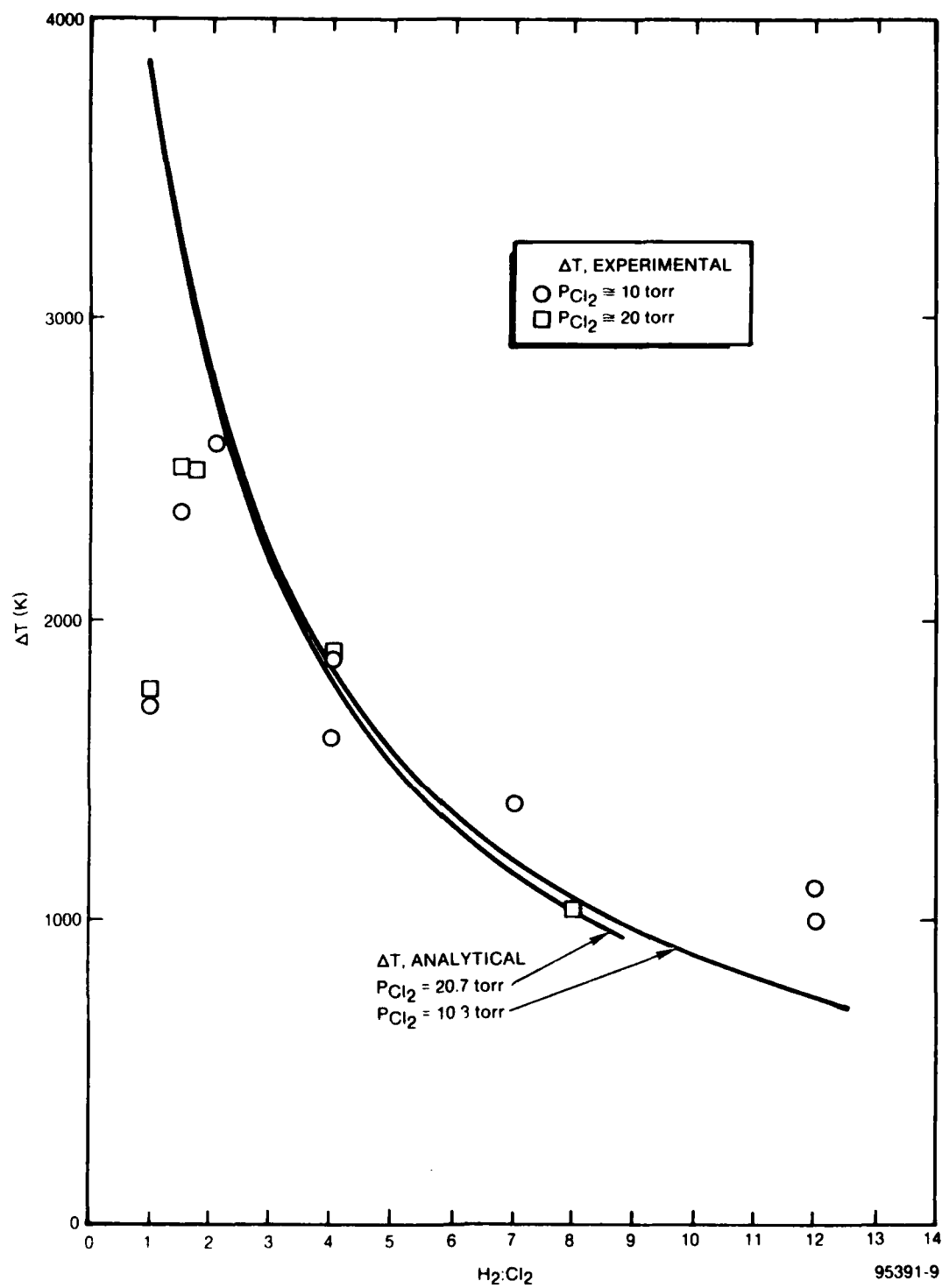


Figure 54. Analytical and experimental temperature rise in  $Cl_2 + H_2$ .

to determine  $\Delta T$  values. Agreement between the calculated and experimental results are quite satisfactory at high  $H_2:Cl_2$  ratios. As this ratio is reduced, the reaction to form HCl does not go to completion and the chemical energy input is reduced, leading to a lower observed  $\Delta T$ . The temperature rise calculations shown in Figure 54 were obtained using 2 or 3 iterations on the specific heat. Initial  $\Delta T$  values were calculated using  $C_v$  at 300K. The calculations were repeated using a  $C_v$  value for an average  $(T_{FINAL} + 300)/2$  temperature. The procedure was repeated again if necessary.

## CONCLUSIONS

The work reported here was conducted to obtain and demonstrate a basic understanding of the phenomena of energy deposition and release in halogens, mixed halogens, and halogens plus fuel. The results are useful for evaluation of space propulsion systems which derive all or part of their energy from solar absorption. However, the scope of work did not include engineering or system evaluations of such space propulsion systems. Therefore, the conclusions presented here relate to basic phenomena rather than potential feasibility of applications.

The flash photolysis approach to evaluation of energy deposition and release provides an easy and convenient way to screen reactants and reactor operating conditions. Conditions which provide high energy absorption and release can be quickly identified. Quantitative determination of the energy absorption and of energy release contain uncertainties due to acoustic phenomena and incomplete information regarding flashlamp output.

Experimental determination of energy deposition and release provided self consistent data which was in satisfactory agreement with analytical predictions and correlations.

Simple analysis based on spectroscopic and thermochemical principles can provide a satisfactory correlation of pressure and temperature increase induced by absorption of radiation. However, the analysis does not predict the degree to which the chain reaction goes to completion.

The Rocketdyne numerical analysis program, Radiation Kinetics Mixing (RKM) provides good predictions of energy deposition and release for halogen-only systems. For systems involving a chain reaction, the role of impurities and diluents as chain terminators can be explored. By modification of the chain termination rates, the model appears to be capable of correctly predicting

the time evolution of properties in the photolysis reaction. The spatial evolution feature, applicable to a flowing reactor, was not applied here. It is believed that the computations performed are the most detailed to date.

The kinetic rate package, which was developed using direct literature values and/or analogies, appears to be generally satisfactory for the chemical reactions studied. Some uncertainties remain regarding recombination rates involving  $\text{SF}_6$  as a third body. The kinetic data set is believed to be the most comprehensive and accurate available for the chemical reactions studied.

Energy deposition in  $\text{Cl}_2$  and in  $\text{ICl}$  initially at room temperature can lead to a temperature rise of up to nearly 1000K. This corresponds to nearly 10% of the halogen being dissociated. Enhanced absorption coefficients at higher temperature would increase the energy depositions but this phenomenon has not been explored in this program.

Photoinitiated reaction of  $\text{Cl}_2 + \text{H}_2$  mixtures can lead to temperature rises of a few thousand degrees K. As much as 10-15% of the energy released can originate in absorption of radiation.

The photoinitiated reaction between  $\text{Cl}_2$  and  $\text{H}_2$  fails to go to completion at low pressure without excess  $\text{H}_2$ . When diluents or impurities are present, these terminate the chain.  $\text{SF}_6$  is moderately effective as a chain terminator and  $\text{O}_2$  is extremely effective. In the reactions observed here with  $\text{SF}_6$  diluent and  $\text{O}_2$  impurity, the highest  $\text{Cl}_2$  utilization was only about 50%.



## RECOMMENDATIONS

Based on the results and understanding developed in this program, it would appear logical and beneficial to pursue this general area of research and development. The recommendations presented here are of three general types. The first type represents engineering analysis in order to assess the feasibility of space based solar propulsion systems employing the principles discussed here. The second type represents additional experimental and analytical research leading to improving the data base and understanding relative to solar conversions via gas phase absorption of solar radiation. The third type of recommendation deals with development of proof of principle solar reactors applicable to space propulsion.

### 1. Engineering analysis

It is recommended that a small design analysis study be conducted to configure and optimize space propulsion systems based on halogen gas phase absorption of solar radiation. The study could begin immediately using the results and understanding developed in the present program plus other open literature data.

### 2. Additional experiments and analysis.

It is recommended that the experimental and analytical approaches developed in the present program be applied to evaluation of some important aspects of solar radiation by halogens. Enhancement of the absorption through heating of the reactants and through use of mixed halogens should be explored. Improvements in the experimental approach through improved characterization of the flashlamp output and measurement of total energy absorption should be included.

### 3. Small scale reactor development.

It is recommended that a small scale solar absorber be developed and tested using terrestrial solar flux. The device should be of a flowing gas closed loop design to allow some of the absorbed energy to provide system heating, thereby enhancing absorption coefficients. This heating could also be simulated through electrical heating of a flowing open loop device. Instrumentation would provide for controlled extraction and measurement of the deposited energy.

# LIST OF REFERENCES

1. Chaudoir, D. W., Niggemann, R. E. and T. J. Bland  
"A Solar Dynamic ORC Power System for Space Station Application,"  
Paper 859085, Proceedings of the 20th Intersociety Energy Conversion  
Engineering Conference, Miami Beach, Florida, August 18-23, 1985.
2. Shoji, J. M., Solar Rocket Component Study,  
AFRPL-TR-84-057, Air Force Rocket Propulsion Laboratory, Edwards Air  
Force Base, Calif., July, 1984.
3. Wolfe, W. L., and Zissis, G. J. eds., The Infrared Handbook,  
IRIA-ERIM, 1978.
4. Thekaekara, M. P., "Evaluating Light from the Sun", Optical Spectra,  
pp 32-35 March, 1972.
5. McDaniel, E. W., Flannery M. R., Thomas, E. W. Ellis, H. W. and  
McCann, K. J. Compilation of Data Relative to Nuclear Pumped Lasers,  
U.S. Army Missile Research Development Command, Rept; H-78-1, Vol. V,  
Feb. 1979,
6. Okabe, H., Photochemistry of Small Molecules, John Wiley & Sons, 1978.
7. Seery, D. J., and Britton, D. "The Continuous Absorption Spectra of  
Chlorine, Bromine, Bromine Chloride, Iodine Chloride, and Iodine  
Bromide," Journal of Physical Chemistry, Volume 68, page 2263, 1964.
8. Hohla, K., and Kompa, K. L. "The Photochemical Iodine Laser," in  
Handbook of Chemical Lasers, R. W. F. Gross and J. F. Bott,  
eds. John Wiley & Sons., 1976.
9. Scragg, R. L. and Parker, A. B. Solar Reactor Steam Generator  
Method and Apparatus, U.S. Patent 3,998,205, Dec. 21, 1976.
10. Scragg, R. L. and Parker, A. B. Solar Reactor Engine, U.S. Patent  
4,024,715, May 24, 1977.
11. Scragg, R. L. and Parker, A. B. Solar Reactor Engine, U.S. Patent  
4,026,112, May 31, 1977.
12. Scragg, R. L. and Parker, A. B. Solar Reactor Combustion Chamber,  
U.S. Patent 4,070,861, Jan. 31, 1978.
13. Scragg, R. L. and Parker, A. B. Electromagnetic Reactor Engine  
System-Apparatus and Method, U.S. Patent 4,175,381, Nov. 27, 1979.
14. Quan, V., Persselin, S. F. and Yang, T. T. "Computation of  
Reacting Flowfield with Radiation Interaction in Chemical  
Lasers," AIAA Journal, Vol. 21, page 1283, 1983.

15. Quan, V., Vieceli, J. J. and Yang, T. T. "Source Flow Chemical Laser Cavity Performance," Applied Optics, Vol. 23, page 1381, 1984.
16. Gonz, J. H. and Newell, B. "Spectra of Pulsed and Continuous Xenon Discharges", Journal of Optical Society of America, Vol. 56, page 87, 1966.
17. Widman, R. P. and Degraff, B. A. "On the Gas Phase Recombination of Chlorine Atoms," Journal of Physical Chemistry, Vol. 77, No. 1, pp. 1325-28, 1973.
18. Hippler, H. and Troe, J. "Flash Photolysis Study of the Recombination of Chlorine Atoms in The Presence of Various Inert Gases and NO", International Journal of Chemical Kinetics, Vol. VIII, pp. 501-510, 1976.
19. Maier, H. N. and Lampe, F. "Heteronuclear Recombination of Chlorine and Iodine Atoms in the Flash Photolysis of Iodine Monochloride", Journal of Physical Chemistry, Vol. 77, pp. 430-34, 1973.
20. Blake, J. A. and Burns, G., "Kinetics of Iodine Atom Recombination Between 300° and 164°K", Journal of Chemical Physics, Vol. 54, No. 4, pp. 1480-86, 1971.
21. Smith, F. T., "Three Body Collision Rates in Atomic Recombination Reactions", Discussions of the Faraday Society, Vol. 33, page 183, 1962.
22. Gross, R. W. F., and Bott, J. F., "Handbook of Chemical Lasers", pp. 33-94, John Wiley and Sons, N.Y., 1976.
23. By Analogy to the Data for  $\text{Cl} + \text{Cl} + \text{M} = \text{Cl}_2 + \text{M}$ ,  $\text{I} + \text{I} + \text{M} = \text{I}_2 + \text{M}$ , and  $\text{I} + \text{Cl} + \text{M} = \text{ICl} + \text{M}$ .
24. Benson, S. W., "Thermochemical Kinetics", pp. 113-115, John Wiley and Sons, Inc., New York, 1968.
25. By Analogy to  $\text{H} + \text{F} + \text{M} = \text{HF} + \text{M}$  and  $\text{H} + \text{Cl} + \text{M} = \text{HCl} + \text{M}$  Systems.
26. Miller, J. C., "Gas Phase Kinetics of the Cl-H<sub>2</sub> System", Ph.D. Thesis, University of Illinois at Chicago, 1982.
27. Clyne, M.A.A. and Crus, H., "Atomic Resonance Fluorescence Spectroscopy for the Rate Constants of Rapid Bimolecular Reactions, Part 2 - Reactions of  $\text{Cl} + \text{BrCl}$ ,  $\text{Cl} + \text{Br}_2$ ,  $\text{Cl} + \text{ICl}$ ,  $\text{Br} + \text{IBr}$ ,  $\text{Br} + \text{ICl}$ ", Journal of the Chemical Society, Faraday Transactions 2: Chemical Physics, Vol. 68, pp 1377-87, 1972.
28. Appelman, E. H. and Clyne, M. A. A., "Reaction Kinetics of Ground State Fluorine, FP Atoms", Journal of the Chemical Society, Faraday Transactions 1: Physical Chemistry, Vol. 71, No. 10 page 2072, 1975.

29. Bung, J. P., Malins, R. J., and Setser, D. W., "Comparison of Rate Constants for Reactions of Hydrogen Atoms with Chlorine, Fluorine, Iodine Chloride, and Chlorine Fluoride", Journal of Physical Chemistry, Vol. 83, No. 8, page 1907, 1979.
30. Wagner, H. G. and Wolfrum, J., "Reactions of Atoms", Angewandte Chemie International Edition, Vol. 10, No. 9, pp. 604-19, 1971.
31. Bergmann, K. and Moore, C. B., "Energy Dependence of the Total Reaction Rate of  $\text{Cl} + \text{HI}$  and  $\text{Cl} + \text{HBr}$ ", Journal of Chemical Physics, pp. 643-49, 1975.
32. Mai, C. C. and Moore, C. B., "Temperature Dependence of Total Reaction Rates for  $\text{Cl} + \text{HI}$  and  $\text{Cl} + \text{HBr}$ ", Journal of Chemical Physics, Vol. 67, No. 5, pp. 3936-39, 1977.
33. Anlauf, K. G., Polanyi, J. C., Wang, W. H. and Woodall, K. B., "Distribution of Reaction Products. III:  $\text{Cl} + \text{HI}$ ,  $\text{Cl} + \text{DI}$ ", Journal of Chemical Physics, Vol. 49, No. 11, page 5189, 1968.
34. Sullivan, J. H., Journal of Chemical Physics, Vol. 30, page 1292, 1962.
35. Dickens, A. F. T., and Milne, G. S., "Tables of Bimolecular Gas Reaction Rates", NSROS-NBS9, October 1967.
36. Herbelin, J. M. and Emanuel, G. "Einstein Coefficients for Diatomic Molecules", Journal of Chemical Physics, Vol. 60, No. 2, pp. 689-95, 1974.
37. Hampson, Jr., R. F. and Garin, D., "Chemical Kinetic and Photochemical Data for Modeling Atmospheric Chemistry", NBS Tech. Note 866, June 1975.

END

FILMED

3 - 86

DTIC